Enabling Ultra Deep Hydrodesulfurization by Nanoscale Engineering of New Catalysts

Christoffersen, Ann-Louise Nygård

Publication date:
2017

Document Version
Publisher's PDF, also known as Version of record

Enabling Ultra Deep Hydrodesulfurization by Nanoscale Engineering of New Catalysts

Ann-Louise Nygård Christoffersen

August 9, 2017

Preface

This thesis is submitted in the candidacy of the PhD degree in physics from the Technical University of Denmark (DTU). The work presented was carried out at the Department of Physics as part of the HYDECAT project, which was funded by Innovation Fund Denmark. The funding support is gratefully acknowledged, as are the co-workers in the HYDECAT project.

The work was carried out in the period January 2014 - July 2017 under the supervision of Professor Ib Chorkendorff. I would like to thank him for granting me the opportunity to work in a scientific research environment with such talented, skilled and dedicated people.

As I am looking back, more than three years after my engagement to this project, I have now come to realize some very important things. The time and effort put into a certain research project is not necessarily reflected by tangible or ground-breaking scientific results. Troubleshooting becomes a daily routine, and the complexities seem inexhaustible in ways I personally never imagined before. Since technical know-how does not come overnight, I am still trying to get grounded on a very steep learning curve, but many people helped me on my way, and I want to mention some of them here.

Michael Brorson, Haldor Topsøe A/S, for supervision during my external stay and for always being positive and open-minded. Thank you for nice, rewarding discussions and for proofreading this thesis.

Robert Jensen, scientific floor manager, for teaching me literally everything I know about UHV. Your patience in answering countless numbers of questions has been priceless. I will miss your company and our conversations about random and important things in life, your resolute opinions and definitely your multicolored socks!

Sine Olesen, my office room mate during three years, you have been the best

company. Your optimistic being have made things easier for sure.

Dan and Heise from the workshop for great assistance in the process of building and designing the new parts for my setup.

Assistant Professor, Jakob Kibsgaard and Christian Elkjær, postdoc. in HY-DECAT, for showing such interest in my experimental results and helping me out with data interpretation, guidance and proofreading. I really appreciate it.

Anders Bodin for preparing all the samples presented in this thesis. It has been a pleasure working with you and I have enjoyed our interesting discussions about work and life together with Daniel Trimarco. It has been a pleasure to be "the girl next-door" and meet for cookies every second hour during the last months of writing our theses.

Jakob Ejler Sørensen, for great help, support and proofreading most of this thesis. I have really enjoyed your company and our regular trips to the coffee machine.

Kenneth Nielsen, Béla Sebök, Claudie Roy, Søren Scott, Brian Knudsen and the rest of the people at SurfCat, for making this a nice place to work.

Furthermore, I would like to thank my parents for being supportive and optimistic on my behalf - with this thesis it seems like I finally passed the "course".

To all my friends outside DTU - long time no see! I look forward to seeing you soon and let you know how much I have valued your support, especially during the last six months.

Last, but certainly not least. Thank you, Lars, for your love, support, patience and everything else. You simply rock my world!

Abstract

The HYDECAT project was initiated to make a targeted effort in the field of hydrodesulfurization (HDS), which is the process where sulfur is removed from crude oil by addition of hydrogen to form hydrocarbons and hydrogen sulfide. This PhD thesis represents my share in the project.

Due to the adverse environmental and societal effects of sulfur emissions from on-road transportation, legislation has been continuously tightened, pushing oil refiners to produce ultra-low sulfur diesel (ULSD), with a maximum sulfur content of 15 ppm. Since these specifications are expected to be further tightened, the existing HDS catalysts fall short.

Experiments were performed on a setup dedicated to testing minute amounts of well-defined catalytic systems in the ambient pressure gas phase HDS of the model compounds dibenzothiophene (DBT) and 4,6-dimethyldibenzothiophene (4,6-DMDBT). An existing µ-reactor platform connected to a high resolution time-of-flight mass spectrometer (TOF-MS) was modified and optimized for this specific reaction. The µ-reactor has a reaction volume of only 240 nL and can be operated between 0.1-5 bar and temperatures up to 400 °C. Only 0.01 % of the mixed gas flows from the two inlets, O1 and O2, is bypassed through the reaction chamber and exposed to the catalyst. A channel terminated by a narrow capillary ensures that the entire reaction gas volume can be directed into the TOF-MS by probing only $5{\cdot}10^{14}$ molecules/s.

The low vapor pressure of both DBT and 4,6-DMDBT complicated the process of introducing them in their gaseous form into the µ-reactor at ambient pressure, and a specially designed flange with an incorporated ion source and internal heat tracing was implemented.

HDS of DBT and 4,6-DMDBT at 800 mbar on six mass-selected Pt samples were conducted. Two Pt samples of ∼3 nm (185 kamu) and two samples of ∼6 nm (1500 kamu) all showed that only the direct desulfurization (DDS) pathway was

followed, hence resulting in biphenyl (BiPhe) and 3,3'-dimethylbiphenyl (3,3'-DMBiPhe), respectively. The same was observed for two samples of Pt single atoms. One 1500 ,kamu sample reached full conversion and was used to derive a sensitivity factor, x , relating the DBT and BiPhe signals, since most ionization cross sections were unknown. This was applied in all the following data interpretation. Large deviations between the, in theory, identical samples made it difficult to see any clear trends, and it was estimated that a reaction temperature difference of 30 °C could have induced the different activities observed.

Four NiMo-based samples were tested in the HDS of DBT. Two metallic NiMo samples of ∼3.5 nm (134 kamu), and two in-flight sulfided $NiMoS_x$ samples - one of ∼5 nm (200 kamu) and one of∼6.5 nm (440 kamu). X-ray photoelectron spectroscopy (XPS) and activity measurements emphasized the need for a sulfidation step prior to the reaction, since exposure to air revealed the formation of an oxide layer. Scanning transmission electron microscopy (STEM) images of the in-flight sulfided $NiMoS_x$ samples showed flat lying platelet-like particles in the 200 kamu sample and upright standing particles in the 440 kamu sample. When normalized to the amount of metal in each sample, the activity of the flat lying particles were exceeded by the activity of the upright standing particles by an order of magnitude, indicating that more active edge sites are exposed in the latter and thereby enabling better HDS activity.

Resumé

HYDECAT-projektet blev indledt for at gøre en målrettet indsats inden for afsvovling (HDS), hvilket er processen, hvori svovl fjernes fra råolie ved tilsætning af hydrogen under dannelsen af kulhydrater og hydrogensulfid. Denne ph.d.-afhandling repræsenterer min andel i projektet.

På grund af de uhensigtsmæssige miljø- og samfundsmæssige indvirkninger af svovlemissioner fra vejtransport, er lovgivningen fortsat blevet strammet, og olieraffinaderierne blevet presset til at producere diesel med ultra-lavt svovlindhold (ULSD), som har et maksimalt svovlindhold på 15 ppm. Da disse specifikationer forventes at blive yderligere strammet, kommer de eksisterende HDS katalysatorer til kort.

Eksperimenterne blev udført på en test opstilling dedikeret til test af små mængder af veldefinerede katalytiske systemer under atmosfærisk tryk i gasfase HDS af modelmolekylerne dibenzothiophen (DBT) og 4,6-dimethyldibenzothiophen (4,6-DMDBT). En eksisterende μ-reaktorplatform koblet til et højopløsnings-massespektrometer (TOF-MS) blev modificeret og optimeret til denne specifikke reaktion. μ-reaktoren har et reaktionsvolumen på kun 240 μL og kan anvendes mellem 0,1-5 bar og temperaturer op til 400 ° C. Kun 0,01 % af gasblandingen fra de to inlets, O1 og O2, ledes gennem reaktionskammeret og udsættes for katalysatoren. En outlet kanal termineret af en smal kapillar sikrer, at hele reaktionsgasvolumenet kan ledes direkte ind i TOF-MS'en ved at probe $5{\cdot}10^{14}$ molecules/s.

Lavt damptryk af både DBT og 4,6-DMDBT komplicerede processen med at introducere dem i deres gasform gennem μ-reaktoren ved atmosfærisk tryk, og en specielt designet flange med en inkorporeret ionkilde og intern varmesporing blev implementeret.

HDS af DBT og 4,6-DMDBT blev udført ved 800 mbar på seks masse-selekterede Pt-prøver. To Pt-prøver af∼3 nm (185 kamu) og to prøver af ∼6 nm (1500 kamu)

viste alle, at kun den direkte desulfuriseringsvej (DDS) blev fulgt, hvilket resulterede i henholdsvis biphenyl (BiPhe) og 3,3'-dimethylbiphenyl (3,3'-DMBiPhe). Det samme blev observeret for to prøver med Pt-enkeltatomer. En 1500 kamu prøve opnåede fuld konvertering og blev brugt til at udlede en følsomhedsfaktor, x, der relaterede DBT- og BiPhe-signalerne, da de fleste ioniseringstværsnit var ukendte. Dette blev anvendt i al efterfølgende datatolkning. Store afvigelser mellem de i teorien identiske prøver gjorde det vanskeligt at se nogen klare tendenser, og det blev anslået, at en reaktionstemperaturforskel på 30 ° C kunne have induceret de forskellige observerede aktiviteter.

Fire NiMo-baserede prøver blev testet i HDS af DBT. To metalliske NiMo-prøver af $\sim$3.5 nm (134 kamu), og to in-flight sulfiderede $NiMoS_x$ prøver - én af $\sim$5 nm (200 kamu) og én af$\sim$6.5 nm (440 kamu), blev syntetiseret. Røntgen fotoelektron spectroskopi (XPS) og aktivitetsmålinger understregede behovet for et sulfidationstrin forud for reaktionen, da eksponering for luft afslørede dannelsen af et oxidlag. Skanning transmissions elektron mikroskopi (STEM) billeder af de in-flight sulfiderede $NiMoS_x$ prøver afslørede planliggende pladelignende partikler i 200 kamu prøven og opretstående partikler i 440 kamu prøven. Når disse blev normaliseret til mængden af metal i hver prøve, blev aktiviteten af de planliggende partikler overgået af aktiviteten af de opretstående stående partikler med en størrelsesorden, hvilket indikerer, at flere aktive kantsites eksponeres i sidstnævnte og derved muliggør bedre HDS aktivitet.

Nomenclature

β-DBT Alkyl-substituted dibenzothiophene

3,3'-DMBCH 3,3'-dimethylbicyclohexyl

4,6-DMDBT 4,6-dimethyldibenzothiophene

A1 Acceleration plate

A2 Grid

BCH Bicyclohexyl

BiPhe Biphenyl

CF conflat

CHB Cyclohexylbenzene

DDS Direct desulfurization

DEF Deflection plate

DFT Density functional theory

FOC Focus lens

HDS Hydrodesulfurization

HYD Hydrogenation

L Liner

m/z mass-to-charge

MCP Micro channel plate

QMS Quadropole mass-spectrometer

RTD Resistance temperature detector

SEM Scanning electron microscopy

STEM Scanning transmission electron spectroscopy

STM Scanning tunneling microscopy

TEM Transmission electron spectroscopy

TOF-MS Time-of-flight mass-spectrometer

ULSD Ultra-low sulfur diesel

XPS X-ray photoelectron spectroscopy

List of publications

Paper 1

Ambient Pressure HDS of Refractory Sulfur Compounds in Highly Sensitive μ-reactor Platform Coupled to a Time-of-Flight Mass Spectrometer.

In preparation. To be submitted to Journal of Physical Chemistry C.

Paper 2

Engineering Ni-Mo-S Nanoparticles for Ultra-Deep Hydrodesulfurization: Reactive Gas Aggregation Synthesis, Characterization and Catalytic Testing.

In preparation.

Contents

Chapter 1

Introduction

Modern day society relies on the practical applications of heterogeneous catalysis to a degree that most people might not be aware of. But even though it might not be general knowledge, several Nobel prizes have been awarded within this field, and the importance of heterogeneous catalysis is tremendous, to say the least [1, 2]. Of the products produced in the chemical industry approximately 90 % are made in catalytic processes and catalysts are the workhorses of chemical transformations [3]. Ammonia production through the population sustaining Haber-Bosch process [4], production of syngas and catalytic cracking that enables processing of petroleum into fuels and chemicals are some of the heterogeneous catalytic processes that have all had an impact on the world as we know it today [3]. In order to conceive how these fundamental breakthroughs have been possible, the basic principles of heterogeneous catalysis must be understood.

1.1 Heterogeneous catalysis

The term heterogeneous catalysis dates back more than a century, and is a process where the reactants and products are in a different phase than the catalyst itself. Typically, the catalyst is a solid which catalyzes either gas phase reactions or molecules in a solution [3, 5]. In 1836 the Swedish chemist J.J. Berzelius published his findings of what he called "a new force". This force was later rephrased to catalysis [6, 7].

According to the International Union of Pure and Applied Chemistry, IUPAC [8], the fundamental definition of a catalyst is

> *a substance that increases the rate of a reaction without modifying the overall standard Gibbs energy change in the reaction.*

Catalysis is a cyclic event that serves to accelerate the reaction rate while leaving the catalyst itself unaltered at the end of reaction [3].

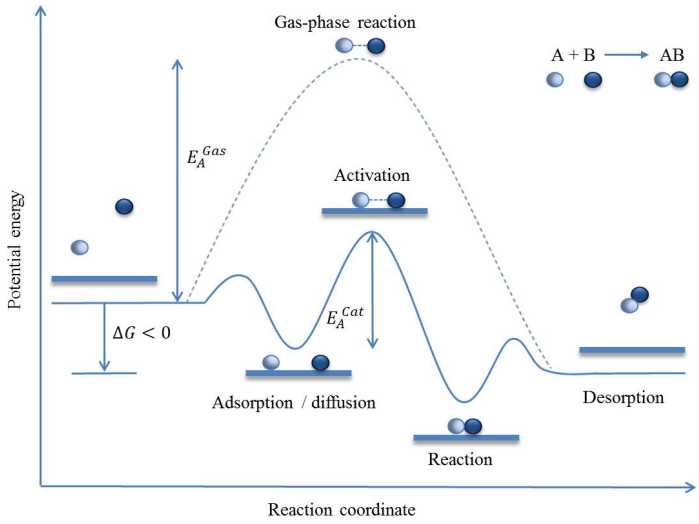

Figure 1.1: *Potential energy diagram, illustrating the elementary steps in a heterogeneous catalytic reaction. Dashed line: the uncatalyzed reaction pathway. Solid line: the catalyzed pathway offering more, but less costly, elementary reaction steps.*

The catalytic pathway can be seen as a sequence of elementary steps. This includes adsorption of the reactants on the surface of the catalyst, diffusion on the surface, breaking or weakening of adsorbate bonds and the creation of new bonds to form the product molecules. When the products desorb, the active site will be regenerated and the catalytic cycle is complete [9].

As can be seen from figure 1.1, the catalytic reaction pathway (solid line) is much more complex than the uncatalyzed pathway (dashed line), but the lowering in activation barriers for these elementary steps makes the former energetically

more favorable. In brief, the catalyst changes the kinetics but not the thermodynamics of a chemical reaction [5].

One of the key parameters in understanding and tuning catalysis towards higher efficiency is the surface of the catalyst. This is where any chemical transformation takes place, and the reactivity can be directly correlated with the number of exposed active surface sites, which is why high-surface-area supports are often applied in technical catalysts as a means of dispersing the catalytically active material. Another way of expressing the concept of figure 1.1 is by the Sabatier principle. A catalyst is reaction specific and will not work for any reaction, and the Sabatier principle can offer qualitative guidance within the search for alternative catalytic materials. It states that the maximum activity can be obtained when the reaction intermediates have an intermediate heat of formation [10–12]. In other words, the rate of reaction will be too slow or simply not proceed if the reactants, intermediates or products bind too strongly to the catalyst surface, not leaving any available active sites for new reactants to be converted. If the binding is too weak, no reaction will occur at all. The optimum catalyst is therefore a catalyst that binds just strongly enough for the reactants to be able to react, but weakly enough to be able to release the products from the surface after reaction.

1.1.1 Nanoparticles in catalysis

The scale lengths in catalysis range from the macroscopic domain of industrial reactors to the atomic and molecular scale, where most fundamental research is found. The nanoscale domain in between deals with size, shape, structure and composition of the active material, and is of significant interest when designing new catalysts [3].

A material in its bulk phase possesses very different properties than in its nanoparticulate form. Gold is a brilliant example of this, since only small particles have demonstrated high activity in a range of reactions, whereas bulk gold is catalytically inactive [13]. Since catalysis can be referred to as a surface phenomenon, the surface area is preferably maximized in order to increase the dispersion and number of active sites. Nanoparticles exhibit high surface area to volume ratios, and high activities can therefore be obtained with relatively small amounts of material; an important parameter in the industrial world.

The morphology of the nanoparticles is, however, not indifferent, since certain sites may be especially active for certain reactions. The reactivity and selectivity

of nanoparticles can therefore be tuned by controlling the morphology, since certain crystallographic planes are exposed, depending on the shape [14].

One way of predicting the equilibrium shape of a nanoparticle is by a Wulff construction, which relates the surface area of specific crystalline facets to the surface energy by minimizing the total surface energy of the nanoparticle. As the particle gets smaller, the number of undercoordinated sites such as edges, corners and kinks increases as well as the catalytic activity [15]. However, the Wulff construction is a continuum model and does therefore not apply for nanoparticles with a countable number of atoms, that is, nanoclusters, since these might have completely different properties [16, 17].

1.2 Our future with fossil fuels

One of the fields which has been, and still is, heavily dependent on the evolution and development of heterogeneous catalysis is the mineral oil refining industry. Since the industrialization and since World War II, in particular, oil has played an important role in the global energy balance [18, 19], but there are always two sides of the same story, and we are currently facing the darker one. The use of oil as an energy source has shown its downsides and the evidence is hard to ignore.

Crude oil is a mixture of different hydrocarbons, salts and metals, along with oxygen, nitrogen and sulfur [20]. Especially the presence of sulfur is met with much debate and the reasons are many. Air pollution and "acid rain" caused by the combustion of fossil fuels affect both urban and industrial areas. Furthermore, the formation of inorganic aerosol gases which are harmful to human health indicates that this is not only an environmental but also a societal problem. It remains the single largest health risk in Europe today [21] and we have "a public emergency" according to the World Health Organization [22].

One of the steps taken to minimize and circumvent the consequences of the problem has been the continuously tightened restrictions and legislation on the sulfur content in fuel for road transportation [23, 24].

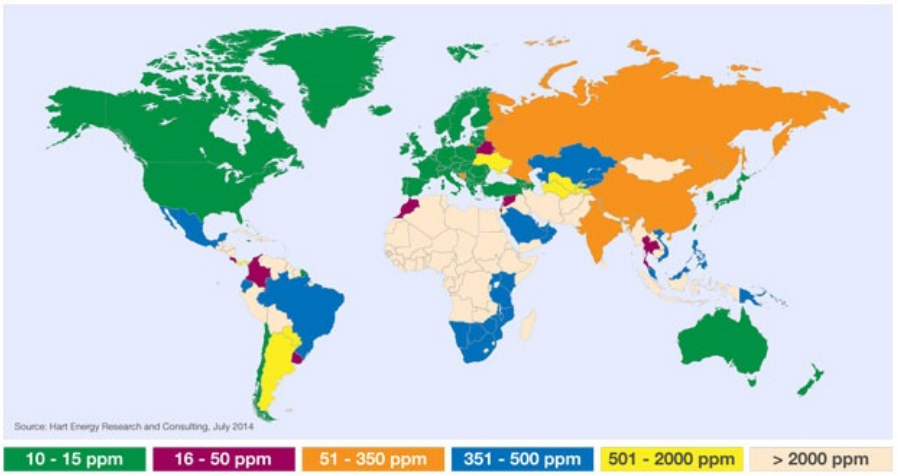

Figure 1.2: *Worldwide maximum on-road diesel sulfur limits in 2014. Reprinted from [25].*

During the last decade, diesel fuel specifications have tightened exponentially and pushed oil refiners to make great efforts to produce ultra-low sulfur diesel (ULSD), with a maximum sulfur content of 15 ppm [26]. In 2014, the emission regulations demanded that all diesel fuel should be ULSD in most of the Western World as can be seen in figure 1.2 and the development towards even tighter specifications can be expected to continue. But even though focus and awareness about the unintended and inappropriate consequences have been addressed since the late 1980's and the necessity of alternative energy solutions is widely recognized, oil and hydrocarbon still remain the most important energy source worldwide [27, 28].

As seen in figure 1.3a, the primary global energy consumption has steadily increased since 1965, with oil and gas as the most prevailing fuels. Even though the share in primary energy of oil is decreasing it still accounts for almost 30 % of the world's energy consumption [19]. Fossil fuels are predicted to still prevail for many years to come, and according to the British multinational oil and gas company, BP, the demand for oil will continue to grow, though at a slower pace [18].

This sets the stage for continuously expanding and exploiting technical solutions to the challenge of reducing the sulfur content in on-road transportation fuel in

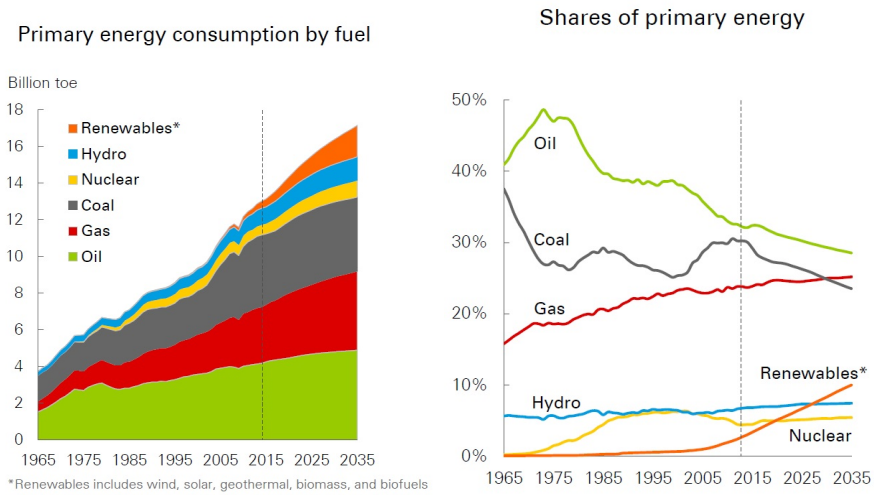

(a) Primary energy consumption by fuel *(b) Shares of primary energy*

Figure 1.3: *The gradual global transition in fuel mix considering the most likely path for the global energy markets over the next 20 years [18].*

the drive towards greener chemistry and more widespread sustainability [5, 29, 30].

1.2.1 Hydrodesulfurization (HDS)

With increasing focus on environmental protection a lot of research has been done with the aim of reducing both NO_x and SO_x emissions from cars [31, 32]. During the last decades the sulfur content in diesel fuel, hence the worldwide SO_2 emission, has been remarkably reduced in one of the most important hydrotreating processes, the hydrodesulfurization (HDS) process.

The HDS process removes sulfur impurities from crude oil by addition of hydrogen without changing the number of carbon atoms [20]. The reaction can be described by equation 1.1

$$RSH + H_2 \longleftrightarrow RH + H_2S \tag{1.1}$$

where R indicates the main body of the organic molecule to be desulfurized. It is a well-established process employed since the 1940's to increase the quality of the oil blend, and because of its dominance within the hydrotreating field, hydrotreating catalysts are commonly referred to as HDS catalysts [33, 34].

In the aftermaths of the first oil crisis in the 1970's the necessity of increasing the output of the remaining oil resources, typically containing more sulfur, became clear. As a result great effort was made to understand and improve the HDS catalyst and enable deep HDS[1] by fundamental and thorough research studies on these types of catalysts [37]. However, the industrial challenge in removing sulfur from diesel fuel completely still remains, and has formed the basis for the work presented in this thesis.

[1] Deep HDS is the desulfurization of the most refractory sulfur species (more than 95 % conversion) to obtain ULSD [34–36].

1.3 The HYDECAT project

In 2013 the HYDECAT project was launched, introducing a collaboration between Haldor Topsøe A/S, Aarhus University (AU) and the Technical University of Denmark (DTU), in order to make a targeted effort in the field of HDS. The following areas were in focus

- Obtaining detailed information on the different adsorption modes of dibenzothiophene (DBT) and 4,6-dimethyldibenzothiophene (4,6-DMDBT) on Co-Mo-S models on a Au (111) substrate using Scanning Tunneling Microscopy (STM)
- Density functional theory (DFT) calculations to support the observations from STM.
- Information on the active state and structure of a typical industrial HDS catalyst using Transmission Electron Microscopy (TEM)
- Synthesis and activity measurements of new catalysts performed at the combined ambient pressure and ultra-high vacuum (UHV) setup

The last mentioned being my share in the HYDECAT project.

1.4 Thesis Outline

Chapter 2 This chapter gives an overview of the industrial HDS process and serves to motivate and put this work into perspective, by zooming in from industrial scale to molecular understanding. It starts with a refinery walk-through and ends at the core of this thesis.

Chapter 3 The experimental techniques used the most in this project are presented in this chapter. The main emphasis is put on the µ-reactor platform and the TOF-MS. It covers both the design and dimensions of the µ-reactor, as well as the working principle of the TOF-MS. Finally, the current setup configuration is introduced, together with the specially designed flange with incorporated ion source and heat tracing.

Chapter 4 Due to the heavy amount of data obtained during every experiment, an entire chapter is dedicated to the explaining of data acquisition and data treatment. This forms the basis for understanding the results presented in the following chapters.

Chapter 5 Fundamental observations related to the experimental procedures are presented in this chapter. It covers the phase change of DBT and 4,6-DMDBT from solid compounds to their gaseous form and considerations related hereto, in order to perform gas phase HDS in the µ-reactor at ambient pressure. Furthermore, some of the unforeseen technical challenges are shortly reviewed.

Chapter 6 HDS of DBT and 4,6-DMDBT on mass-selected Pt nanoparticles and Pt single atoms are presented in this chapter. The sensitivity factor is introduced in order to estimate the conversion and turnover frequency.

Chapter 7 HDS of DBT on mass-selected NiMo-based nanoparticles are presented. Metallic as well as in-flight sulfided nanoparticles are tested, and the morphologies are correlated to the respective activities.

Chapter 2

From industrial scale to molecular understanding

Being a broad and highly complex field of study, understanding heterogeneous catalysis is often a task that involves several scientific disciplines. The detailed knowledge about technical industrial catalysts has been an interplay between theory and experimental techniques going from the microscopic to the macroscopic scale [3], allowing to bridge some of the gaps between real catalysts and surface science studies [5,9,38,39]. To pinpoint the role of the hydrodesulfurization process, a short refinery walk-through will be given in this chapter, followed by a review of advances within this field. Hopefully, this will clarify the purpose and importance of the present work when put into a broader perspective.

2.1 Refinery walk-through

Since the industrial revolution in the second half of the nineteenth century and the introduction of cars as a more and more common means of transport, oil refineries have converted crude oil into higher-value fuel products and petrochemicals all over the world. The concerns about the use and depletion of fossil fuels did not emerge until 100 years later [5].

Crude oil is an extremely complex chemical mixture consisting of alkanes, naphthenes, monoaromatics, polyaromatic hydrocarbons, traces of metals, sulfur, nitrogen and various salts among others [40]. The exact component mixture

depends on the geographical origin of the oil, while physical characteristics determine the optimum refining operating conditions [41–43]. The elemental composition of crude oil typically varies within the ranges seen in Table 2.1.

Table 2.1: *Elemental composition of conventional crude oil [20]*

Element	**Wt. %**
Carbon	83-87
Hydrogen	10.5-13.5
Sulfur	0.05-6
Nitrogen	0.02-1.7
Oxygen	0.05-1.8
Metals	0.00-0.15

Refining of crude oil involves several physical and chemical processes, including distillation, extraction, reforming, hydrogenation, cracking, and blending. One of the most important products resulting from these processes is diesel fuel [20, 34, 41]. From the first distillation process, in which the crude fractions are separated as a function of boiling point and molecular weight, until it ends up as diesel fuel, especially one process step is of great importance, namely the hydrodesulfurization.

2.1.1 Industrial HDS

The HDS process reduces the amount of sulfur not only to meet stringent environmental regulations, but also serves to prevent the poisoning and deactivation of other catalytic processes [44, 45].

In the HDS process, sulfur containing compounds are converted into hydrocarbons and hydrogen sulfide by addition of hydrogen under high pressures and elevated temperatures. The feed is normally very inhomogeneous and large demands are therefore put on the technical performance of the HDS catalyst in order to ensure a homogeneous product [46]. A hydrodesulfurization unit consists of several parts, but most importantly are the catalytic hydrotreater, the hydrogen sulfide removal unit, and the stabilizer where the desulfurized products are accumulated [20].

Sulfur containing gas oil fractions are pre-heated, mixed with gaseous hydrogen and trickled through a catalyst bed. Typical operating conditions vary within a temperature range of 300-400 °C and pressures between 20-100 bar [33, 47, 48].

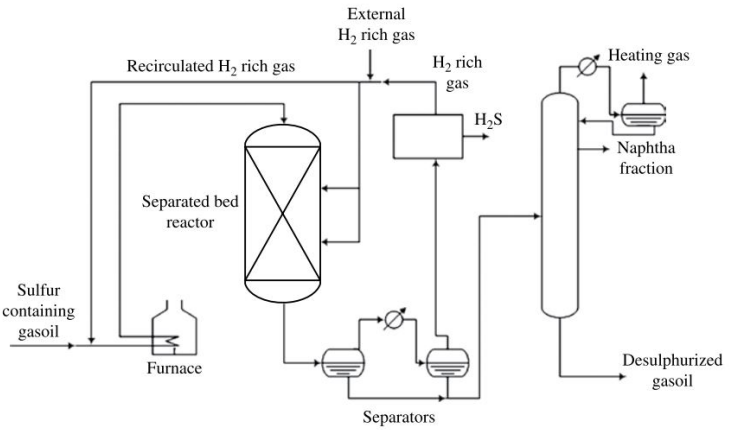

Figure 2.1: *Flow scheme of the industrial HDS process. The sulfur containing gas oil fractions are pre-heated and mixed with hydrogen and trickled through a catalyst bed. Sulfur is removed as H_2S, which is later separated and hydrogen is recirculated to the front of the process. Reprinted from [20].*

Sulfur heteroatoms are removed by the hydrogen and released from the organic molecule as gaseous H_2S, accordingly. The resulting effluent is separated into a liquid- and a vapor phase in two steps, hydrogen sulfide is absorbed and separated, and hydrogen is recovered for recirculation to the front of the process. Finally, the product mixture is separated in a fractionation column, desulfurized gas oil (diesel) being the main product.

2.2 Refractory sulfur compounds

A wide variety of sulfur containing compounds exists in crude oil, and current HDS catalysts are able to reduce the sulfur content to meet emission restrictions. However, since these restrictions can be expected to become even tighter, and feedstocks are increasingly heavy with a higher concentration of more refractory sulfur compounds, the need for new and more efficient HDS catalysts is a pressing matter. Historically, thiophene has been a popular model compound for understanding the HDS mechanism [49–53]. However, the relative ease with which thiophene is desulfurized makes it an inappropriate model molecule for

deep HDS studies.

The reactivity of the sulfur compounds decreases with increasing molecular geometry with the alkyl-substituted dibenzothiophenes (β-DBTs) representing the most refractory sulfur compounds, as illustrated in Figure 2.2 [33, 40].

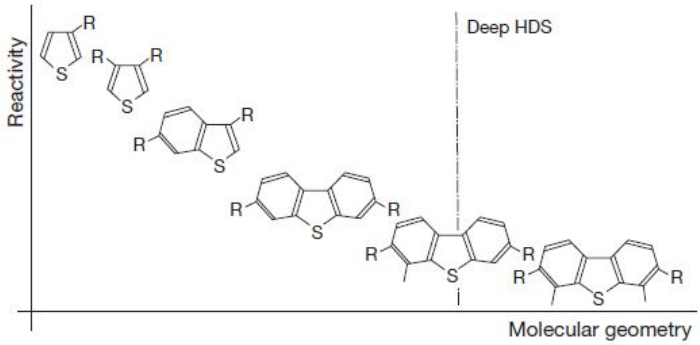

Figure 2.2: *Illustration of the decreasing reactivity with increased molecular geometry. Reprinted from [34].*

The nature of the β-DBTs makes them especially complicated to desulfurize, since the methyl groups located in the fourth and sixth position have a shielding effect on the sulfur atom, causing a steric hindrance [37, 54–59]. The very low HDS activity towards these compounds is the main industrial challenge which has to be overcome in the aim of producing essentially sulfur-free diesel fuel [58, 60].

2.2.1 The catalyst

The knowledge about the catalytic mechanisms in the HDS reaction is based on progressive research and extensive surface science studies. With the aim of engineering new catalysts that enable deep HDS, it is essential to understand some of the most important results from these studies, beginning with the structure and formation of the active sites.

The basic composition of the technical HDS catalyst is represented by a backbone of nanometersized molybdenum disulfide (MoS_2). The diverse properties of MoS_2 have gained increasing attention and countless studies have therefore been conducted, though for very different purposes, such as hydrogen evolution

and photooxidation [61–64]. Some of the most interesting features are attributed to its electronic properties, ability to form nanotubes and efficiency as a solid lubricant to mention a few [65].

Unpromoted MoS_2

MoS_2 has a layered two-dimensional strucuture. It consists of two hexagonal S-planes with an intermediate hexagonal Mo-plane, where the Mo-atoms are trigonal prismatically coordinated to the S-atoms. The resulting S-Mo-S sheets are stacked and held together by van der Waals forces [66], and each sheet features two low-index edge terminations, the $(10\bar{1}0)$ Mo-edge and the $(\bar{1}010)$ S-edge as shown in Figure 2.3 [67]. The morphology of MoS_2 nanoparticles depends on the relative stability of these edges, and since only the edge sites are known to be active in the HDS reaction [68], the exact morphology might have a critical effect on the HDS activity.

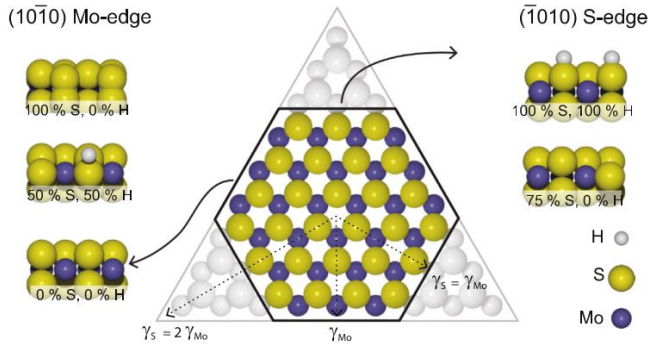

Figure 2.3: *Wulff construction of a hypothetical bulk-truncated MoS_2 nanoparticle were the exposed $(10\bar{1}0)$ Mo-edge and the $(\bar{1}010)$ S-edge terminations can be seen. When the edge free energies are equal, $\gamma_{Mo} = \gamma_S$, the particle will be a perfect hexagon, while $\gamma_S > 2\gamma_{Mo}$ results in a triangular particle with Mo-edge terminations. The ball models illustrate the possible edge structures of the different edge terminations, depending on varying S and H coverages. Reprinted from [69].*

The most active MoS_2-based nanoparticles in the HDS reaction have been shown to adopt a single-layer MoS_2 morphology. This morphology is sensitive to hydrogen adsorption, sulfur coverage and incorporation of promoter atoms, which will dictate the shape and edge terminations [69].

In the industrial HDS, a support material is typically impregnated with oxides of the metals which are turned into the active sulfide phase in a pre-sulfidation step in the reactor [34]. Under sulfiding conditions where the partial pressure ratio is $H_2S/H_2 > 500$, triangular MoS_2 nanoparticles are formed, exposing Mo-edges fully sulfided with sulfur dimers. Reducing this ratio to $H_2S/H_2 < 0.1$ the particles will adopt a truncated triangular shape with both Mo and S-edges, and this scenario very much reflects the commercial sulfiding conditions [70]. It can result in both a lower sulfur coverage at the edges (sulfur vacancies) and the formation of surface S-H groups [68]. However, hydrogen is only stable at the S-edges [65] and the change in S and H coverage also changes the edge free energies, which again drive the equilibrium shape from triangular to hexagonal. The morphology is therefore highly sensitive to the sulfiding agent [71].

Countless STM studies have imaged the MoS_2 nanoparticles with a bright "brim" structure, which is catalytically highly interesting [65, 70, 72–74]. The brim results from a reconstruction in the MoS_2 nanoparticle, so that the otherwise semiconducting nature of MoS_2 is only present at the interior of the particle, whereas the edge sites are metallic, thus appearing bright by STM.

Promoted MoS_2

For the HDS reaction, MoS_2 is usually promoted by nickel or cobalt, dispersed on a high-surface-area support like alumina (γ-Al_2O_3) [75]. The promotion by the first row transition metals appeared for the first time in literature already in 1959 [76], and later, detailed studies by Topsøe and co-workers resulted in the widely accepted Co(Ni)-Mo-S model based on Mössbauer spectroscopy [77]. Since then, especially the combination of STM and DFT complemented by electron microscopy have paved the way for understanding the origin of the HDS activity [66, 78–81].

When single-layer MoS_2 nanoparticles are promoted by cobalt, these preferentially decorate the S-edge where they substitute Mo atoms while the $(10\bar{1}0)$ Mo-edges remain unchanged [82]. The result is a hexagonally truncated Co-Mo-S shape (see Figure 2.4a) [78–80, 83, 84]. The coexistence of Co_9S_8 (cobalt sulfide) and Co incorporated into the support material have also been identified, however only the Co-Mo-S phase have shown activity in the HDS reaction [77].

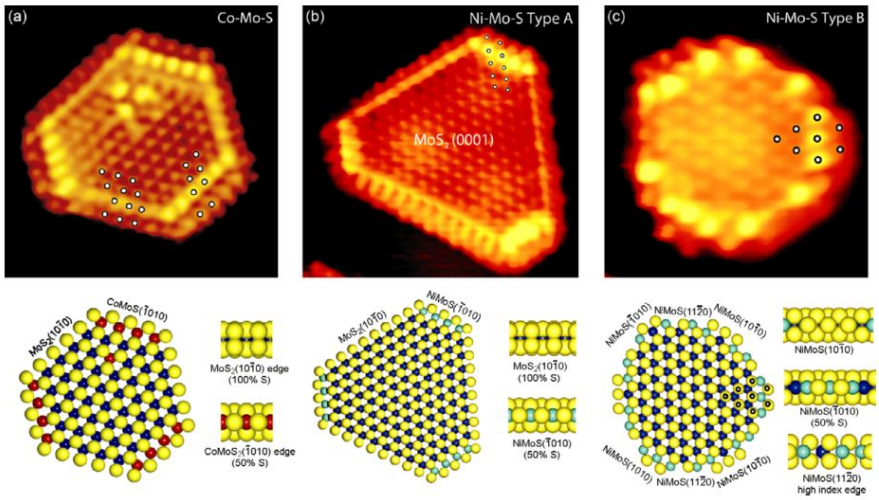

Figure 2.4: *Ball models of Co- and Ni-promoted MoS_2 structures. The incorporation of Co atoms results in a hexagonally truncated shape as seen from (a), whereas the incorporation of Ni atoms can result in a hexagonally truncated shape for larger nanoparticles (b) or a dodecagonal shape for smaller nanoparticles (c) [80]. Reprinted from [34].*

A similar Ni-Mo-S phase has been experimentally confirmed. However, in this case the affinity for Ni to substitute Mo depends on the cluster size: in larger Ni-Mo-S particles (Figure 2.4b, Type A), a truncated triangular shape similar to the one observed for the Co-Mo-S clusters appears, whereas the smaller ones adopt a dodecagonal shape (Figure 2.4c, Type B) [81, 85].

Typically, sulfided Ni-Mo catalysts are more efficient hydrogenation catalysts than the sulfided Co-Mo catalysts, and are preferred in order to treat feedstocks with a high concentration of unsaturated compounds [12]. However, the situation gets even more complicated by the fact that reactions besides the HDS

reaction (like for example the hydrodenitrogenation) occur simultaneously, introducing competitive adsorption and poisoning of other species, especially the carbazoles [46,86–88]. In the end, the choice of catalyst and operating conditions will, however, always be dictated by the exact feed composition [33, 36, 46, 79].

2.3 Reaction pathways

It is generally believed that the active sites are located at the edges of the catalyst particles and that they are associated with the presence of coordinatively unsaturated metal atoms (the brim) [33,65], though the exact mechanism is complex and still not completely understood. However, today it is generally accepted that the hydrodesulfurization process proceeds through one of two possible reaction pathways leading to different products: the direct desulfurization (DDS) pathway and the hydrogenation (HYD) pathway [37, 89–91].

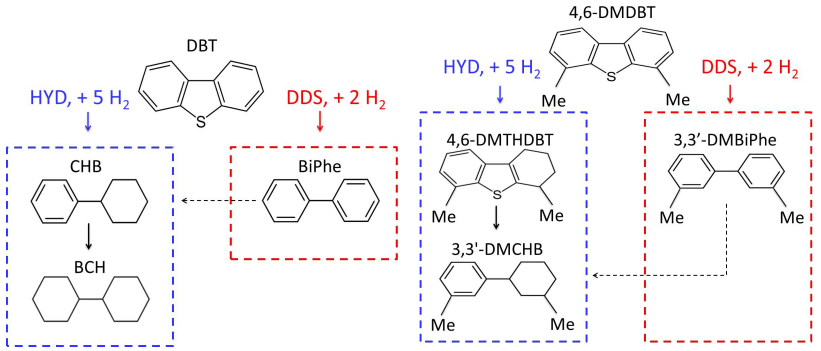

(a) Reaction pathways for DBT. *(b) Reaction pathways for 4,6-DMDBT.*

Figure 2.5: *Simplified sketches of the reaction pathways of DBT and 4,6-DMDBT proposed by Houalla et al. [54, 90].*

The HDS reaction networks of DBT and 4,6-DMDBT have been widely discussed, but most studies rely on the mechanisms proposed by Houalla et al. [54, 90]. Simplified sketches can be seen from Figure 2.5.

In the DDS pathway the sulfur atom is directly extruded from the molecule by hydrogenolysis of the C-S bonds, also known as the σ-mode, whereas the molecule adsorbs in π-mode and undergoes hydrogenation of the aromatic ring

prior to the actual desulfurization in the HYD pathway, which is much more hydrogen consuming [44]. The hydrogenation of cyclohexylbenzene (CHB) to form bicyclohexyl (BCH) is usually slow, and biphenyl (BiPhe) or CHB are typically the observed products, depending on the operating conditions. The corresponding alkyl-substituted hydrogenation product (not included here) is the 3,3'-dimethyl-bicyclohexyl (3,3'-DMBCH), and is usually not observed under industrial conditions, but has been included in discussions about the possible HYD reaction mechanism of 4,6-DMDBT [92]. It should be mentioned that additional reaction intermediates exist, but for simplicity, these are not included here.

The HYD pathway becomes more important as crude oils become heavier with a higher amount of refractory sulfur compounds. On the other hand, an excessive hydrogenation of the feedstock is a costly affair, which puts an emphasis on understanding the selectivity with respect to the DDS and HYD pathway for a given catalyst [69].

In the HDS of DBT over Co(Ni)-Mo-S catalysts it is generally seen that the DDS pathway is dominant, producing mainly BiPhe. The opposite is observed in the HDS of 4,6-DMDBT, which due to the steric hindrance follows the HYD pathway, resulting in mainly 3,3'-DMCHB [46, 93]. Under industrially relevant conditions the rate constants for the HYD reaction of DBT and 4,6-DMDBT are comparable, whereas the DDS reaction rate constant for DBT is much higher than for 4,6-DMDBT [57]. This again suggests that the steric hindrance in 4,6-DMDBT can only be circumvented through the HYD reaction pathway, where the sulfur extrusion happens after hydrogenation.

It is normally considered that the DDS reaction takes place by sulfur extrusion on the sulfur vacancies formed at the edges or corners of the MoS_2 nanoparticles, due to the very accessible binding sites [94]. For the HYD reaction the picture is more unclear, but it has been suggested that the hydrogenation might occur at one site, and the desulfurization at a different site, proposing an intermediate diffusion step to facilitate this [95, 96].

The adsorption of DBT has been observed by STM on sulfur vacancies on both unpromoted and promoted MoS_2 with a distinct preference for adsorption on corner Co-Mo-S sites [94,95], whereas the Mo-edge is only reactive at the corners [96]. Another interesting observation from STM studies was that DBT do not adsorb on edge vacancies when the MoS_2 cluster is lying flat on the substrate [94, 97], which is important to keep in mind when engineering new catalysts for the HDS reaction. The same studies showed that 4,6-DMDBT does not adsorb on sulfur vacancies nor corner sites. Instead, these molecules were observed to

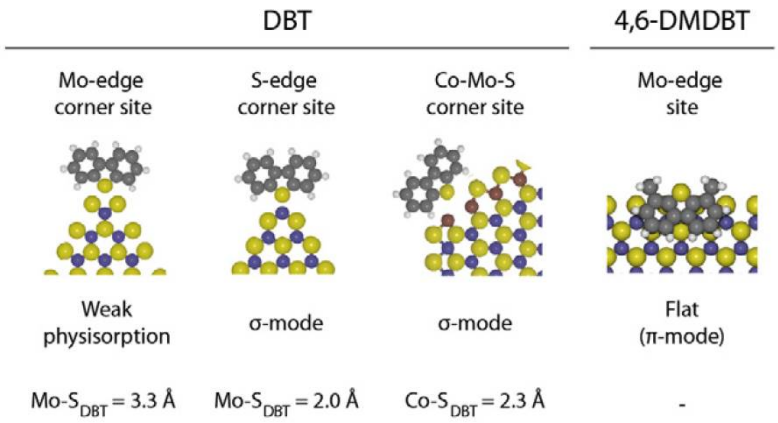

Figure 2.6: *Adsorption modes of DBT and 4,6-DMDBT observed by STM on unpromoted MoS_2 and promoted Co-Mo-S clusters. DBT preferentially adsorbs on corner sulfur vacancies, whereas 4,6-DMDBT adsorbs in a flat configuration on top if the clusters next to the brim sites. Reprinted from [94].*

only adsorb in a flat configuration on top of the clusters next to the brim sites. Figure 2.6 summarizes the different adsorption modes.

Altogether, increasing the number of active sites is always the aim in catalysis. In the case of the HDS of DBT and 4,6-DMDBT the task seems to be the formation of more coordinatively unsaturated sites like edges and kinks which spatially enables the desulfurization, since this step is included in both pathways. Tailoring nanoparticles to expose different morphologies is therefore an obvious approach.

2.4 The model system

In reality, the sulfur content of industrially desulfurized diesel fuel is measured as the total sulfur content without any specification of which sulfur compounds are present. One study did, however, emphasize the importance of proceeding with the most refractory sulfur compounds as test molecules in future catalyst development. Work by Knudsen et al. [46] showed the disappearance of the individual sulfur compounds as a function of the total sulfur content over an

industrial Co-Mo-S catalyst, and it was obvious that down to 1000 ppm total sulfur, only few 4,6-DMDBT molecules had reacted [36]. For this reason, especially 4,6-DMDBT has frequently been applied as a more appropriate probe molecule in the evaluation of the activity in deep HDS [98–100].

Understanding and improving the existing HDS catalyst cannot readily be done under industrially relevant conditions. As is evident from the numerous studies mentioned throughout this chapter, a surface scientific approach is therefore often assumed. These are very useful as controlled, well-defined model systems for gaining insights into the HDS reaction, but since they work under UHV conditions, they cannot be directly extrapolated to industrially relevant conditions.

The work presented in this thesis has focused on the gap between industrial reaction conditions and model systems investigated by surface scientific techniques. Activity measurements have been performed in a setup modified and reconstructed for the gas phase HDS of the model compounds DBT and 4,6-DMDBT under ambient pressure. The setup enables direct and fast product analysis under UHV conditions in a TOF-MS without the interaction of other compounds as seen in the industrial HDS reaction. In this way it is possible to correlate structure and activity and at the same time map out how it relates to the DDS pathway or the HYD pathway based on the observed products. It cannot mimic exact industrial conditions, but it can be useful in the screening for new and more efficient catalysts, where STM and DFT studies lack activity measurements to support their findings.

2.4.1 The challenge

Both DBT and 4,6-DMDBT are heavy molecules which appear as solid colorless crystals at room temperature and share one particular physical property, namely a very low vapor pressure as can be seen from Table 2.2 [101–103].

Table 2.2: *Physicochemical properties of DBT [104] and 4,6-DMDBT [105, 106]*

	DBT	**4,6-DMDBT**
Formula	$C_{12}H_9S$	$C_{14}H_{12}S$
Molecular weight (g/mole)	184.257	212.310
Melting point (°C)	99	153
Vapor pressure at RT (mbar)	$6.1{\cdot}10^{-3}$	$8.2{\cdot}10^{-4}$

Their very low vapor pressures have been one of the biggest challenges through-

out the entire project, since restrictions to the setup and its operating conditions were dictated accordingly. Furthermore, experimental reference data reported in literature has been very limited, complicating the process even more.

Throughout the experiments, the National Institute of Standards and Technology (NIST) database provided a useful guide in interpreting the obtained data. But also this turned out to some extend to be incomplete for the information we were searching for.

Before introducing the details of the experimental setup and the results obtained within the last couple of years, I find it reasonable to take a step back in time and present the reader to some of the technical and most time-consuming tasks.

A beginning, a detour, an open ending

At my time of arrival the setup meant for running my experiments already existed. It appeared to be a quite straightforward task, once familiar with the terms and principles of UHV. I was wrong.

The setup was there, working and ready, but it soon became clear that the molecules we wanted to desulfurize were refractory in more than one way. The very low vapor pressures of the compounds were not an issue when dosing them through a leak valve directly into the TOF-MS. Introducing them through an ambient pressure region into a UHV chamber was a completely different story. We realized the need for heating the compounds significantly, and took on different approaches, which meant that extensive heating of the entire setup was necessary in order to avoid cold spots and condensation of DBT and 4,6-DMDBT in unwanted places. This was also not trivial.

The setup was from the beginning provided with a considerable amount of pneumatic valves, which at an earlier point (and in most other cases), would ease the setup operation. However, these can only withstand temperatures up to 80 °C (this was verified by mistake), and therefore had to be exchanged for manual valves.

Two years into the project we were still searching for the ever-missing compound signal intensities in the TOF-MS and far from running actual activity measurements. We therefore realized that we might have underestimated the need for heating the surroundings, not only at the ambient pressure side, but also at the UHV side, despite what would have been expected based on the pressure differences. This led to drastic modifications of the setup, which are described in more detail in chapter 3, and activity measurement presented in this thesis have therefore been obtained within the last nine months.

Chapter 3

Experimental setup

The experiments described in this thesis were all conducted at the combined ambient pressure and UHV setup. As already mentioned, the setup existed at my time of arrival, but substantial modifications were implemented for this exact project. The changes resulting in the final configuration will be presented in this chapter.

3.1 The µ-reactor platform

The term µ-reactor can be found many places in literature referring to reactors of different dimensions and designs [107]. In the present context, the µ-reactor refers to a silicon based chemical reactor with dimensions in the µm range used for gas phase reactions. It was designed and fabricated at DTU in collaboration between DanChip and SurfCat (previously CINF) and was first introduced in 2009 [108]. A description of the actual fabrication of the chip can be found in [109]. Since then, several reactor designs have been tested in different setup configurations [110–112], which were all optimized for their specific purposes within the fields of heterogeneous catalysis, electrocatalysis and photocatalysis. The current design which has been used throughout the experiments presented in this thesis, is a reactor with outer dimensions of 16.1 x 27 mm, which can be seen in Figure 3.1.

The reactor introduces several advantages due to its clever design, which features two inlets (I1 and I2) and two outlets (O1 and O2). Reactant gases are

introduced through I1 and I2 into a meander structure, which ensures proper gas mixing. Most of the gas from the mixing channel is bypassed to O1 from where the pressure is adjusted with a pressure controller and a turbopump on the backside in a range of 0.1-5 bar and temperature up to 400 °C. Only around 0.01 % of the mixed gas flow will therefore enter the reaction chamber where it is exposed to the catalyst [108]. The resulting gas mixture flows from the reaction chamber through a channel terminated by a narrow capillary. This transition enables direct gas analysis by coupling to a mass spectrometer working under UHV conditions.

3.2 Design and dimensions

The circular reaction chamber has a diameter of 1 cm and a depth of 3 µm, resulting in a reaction volume of approximately 240 nL. The small volume makes it ideal for testing catalytic activity of clusters and nanoparticles, but minute amounts of supported catalyst that fits within the restricted dimensions can also be tested. The small volume also means that small amounts of reactant

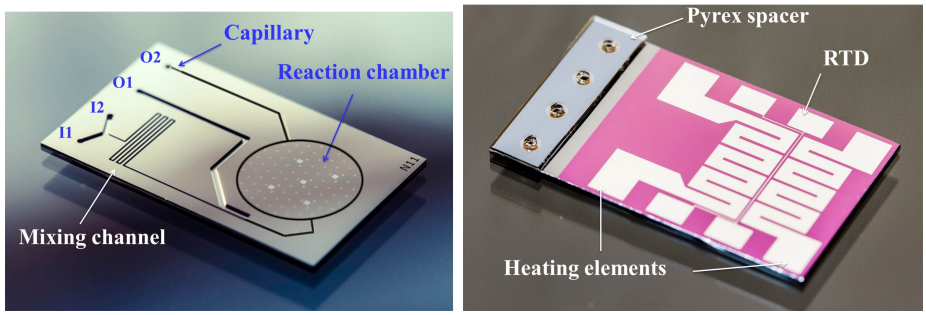

(a) The frontsize of the µ-reactor. *(b) The backside of the µ-reactor.*

Figure 3.1: *The newest µ-reactor design. The frontside has SEM grids for identical location, whereas the backside includes a Pyrex spacer, RTD and heating elements. Pictures by Thomas Pedersen, DTU Nanotech.*

gases are required and in case of explosive gas mixtures the safety issues are extensively diminished. The long mixing channel has a depth of 250 µm and a width of 150 µm. The same depth extends to the channel leading the gas

through the main outlet, O1, but the width is here 500 µm in order to obtain a high flow conductance.

The channel directing the remaining gas fraction into the chamber, the chamber itself, as well as the channel leaving the chamber are only 3 µm deep. Since the gas exiting O2 is entering a mass spectrometer, which operates under UHV, a flow-limiting capillary is included at the end of the channel from the reaction chamber to O2. This capillary is 5 µm wide, 3 µm deep and 1500 µm long resulting in a gas flow through the reaction chamber of around $5{\cdot}10^{14}$ molecules s^{-1}.

3.2.1 Gas flow

The controlled introduction of gas from a high-pressure region to a mass spectrometer working under UHV conditions induces several flow- and pressure regimes. These are especially important to consider when dealing with catalysis, since pressure and temperature will have an effect on the capillary flow, hence also the signal observed in the mass spectrometer [113, 114]. The flow can be sketched as seen in figure 3.2

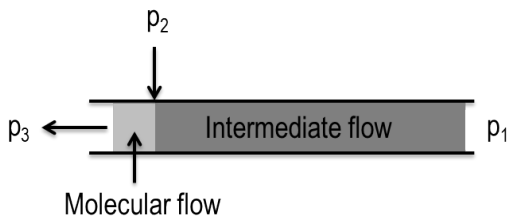

Figure 3.2: *A sketch of the different gas regimes induced by the pressure drop from ambient pressure, p_1, through intermediate flow and pressure, p_2, to UHV conditions, p_3.*

The channel can be divided into two sections, an intermediate flow section and a molecular flow section. The total length of the capillary, l, is therefore divided into l_{int}, being the length of the intermediate flow regime and l_{mol}, which is the length of the molecular flow regime. In order to determine the flow rate through the capillary, both sections have to be considered.

In the intermediate flow section mainly gas-wall collisions occur and the Knudsen

number[1] is $0.01 < {}^{\lambda}/_{d} < 1$. However, at p_2 the flow changes from intermediate to molecular and the Knudsen number is ${}^{\lambda}/_{d} > 1$, which means that gas molecules no longer collide with one another. This transition pressure can be calculated according to

$$p_2 = \frac{k_B T}{\sqrt{2}\pi s^2 \lambda} \tag{3.1}$$

where k_B is the Boltzmann constant, T the temperature, s the molecular diameter and λ the mean free path [113]. At p_2 the mean free path and the capillary diameter become comparable and the flow through the intermediate section is given by

$$\dot{N} = \frac{1}{k_B T}\left(\frac{\pi}{8}\frac{\bar{p}a^4}{\eta l_{int}} + \frac{8}{3}\sqrt{\frac{\pi}{2}}\frac{a^3}{l_{int}\upsilon}\frac{1+2\frac{a\upsilon\bar{p}}{\eta}}{1+2.48\frac{a\upsilon\bar{p}}{\eta}}\right)(p_1 - p_2)\,, \tag{3.2}$$

where a is the capillary radius, η is the gas viscosity, $\bar{p} = \frac{p_1+p_2}{2}$, $\upsilon = \sqrt{\frac{m}{k_B T}}$ and m is the molecular mass.

When the pressure p_1 is assumed to be equal to the pressure within the reaction chamber of the µ-reactor, the pressure p_3 can be assumed to be zero, since $p_3 \ll p_1$. This is a reasonable assumption since the pressure drop through the capillary is dominant [109].

The flow rate through the molecular regime of the capillary can be expressed as

$$\dot{N} = \frac{1}{k_B T}\frac{8}{3}\sqrt{\frac{\pi}{2}}\frac{a^3}{l_{mol}\upsilon}(p_2 - p_3) \tag{3.3}$$

Applying the previously mentioned relation $l = l_{int} + l_{mol}$ and solving for l_{mol} in 3.3, the following expression is obtained

$$l_{mol} = \frac{1}{k_B T}\frac{8}{3}\sqrt{\frac{\pi}{2}}\frac{a^3}{\dot{N}\upsilon}(p_2 - p_3) \tag{3.4}$$

When this is inserted into 3.2 the total flow rate through the capillary is derived as

[1] The Knudsen number is a dimensionless number describing the ratio of the molecular mean free path length to a physical length scale.

$$\dot{N} = \frac{1}{k_B T}\frac{1}{l}\left[\left(\frac{\pi}{8}\frac{\bar{p}a^4}{\eta} + \frac{8}{3}\sqrt{\frac{\pi}{2}}\frac{a^3}{\upsilon}\frac{1+2\frac{a\upsilon\bar{p}}{\eta}}{1+2.48\frac{a\upsilon\bar{p}}{\eta}}\right)(p_1 - p_2) + \frac{8}{3}\sqrt{\frac{\pi}{2}}\frac{a^3}{\upsilon}(p_2 - p_3)\right] \tag{3.5}$$

Equation 3.5 is obviously a very complicated expression depending on several parameters. What is however important to realize is the temperature and pressure dependence, which means that an increase in temperature will decrease the flow, whereas an increase in pressure will increase the capillary flow.

3.2.2 Deposition and bonding

There are several ways of depositing catalyst into the µ-reactor. Macroscopic amounts of supported catalysts can also be deposited, however involving a few steps prior to the actual loading. Essentially, this kind of sample is ground into particles of $< 3\,\mu m$ (the depth of the reactor chamber) and diluted with an appropriate solvent to form a suspension of known concentration. When drop-casting this into the reactor volume, an uneven dispersion of catalyst particles might however arise, due to the surface tension of the solvent, which tends to affect the drying pattern of the droplet. Ideally, mass-selected nanoparticles or thin films can be desposited directly into the reactor by magnetron sputter deposition [112], making the process of sealing the reactor quite smooth.

Mass-selected nanoparticles

The samples applied for HDS measurements in this thesis were all mass-selected nanoparticles deposited by magnetron sputter deposition. I never operated the cluster source myself and a detailed description will therefore not be given. However, the basic principles of this technique appear below.

The production of mass-selected nanoparticles can be divided into three main steps: magnetron sputtering, gas-phase aggregation and filtering.

Sputtering a target of desired material by noble gas ions, typically helium, results in the formation of a metal "vapor". This "vapor" can agglomerate into clusters or nanoparticles in an aggregation zone, facilitated by cooling with liquid nitrogen[2] . Some of the samples were prepared using a synthesis method

[2]Liquid nitrogen is used for cooling and helium and argon mediate heat transfer from the chamber walls to the particles without contributing significantly to the sputtering.

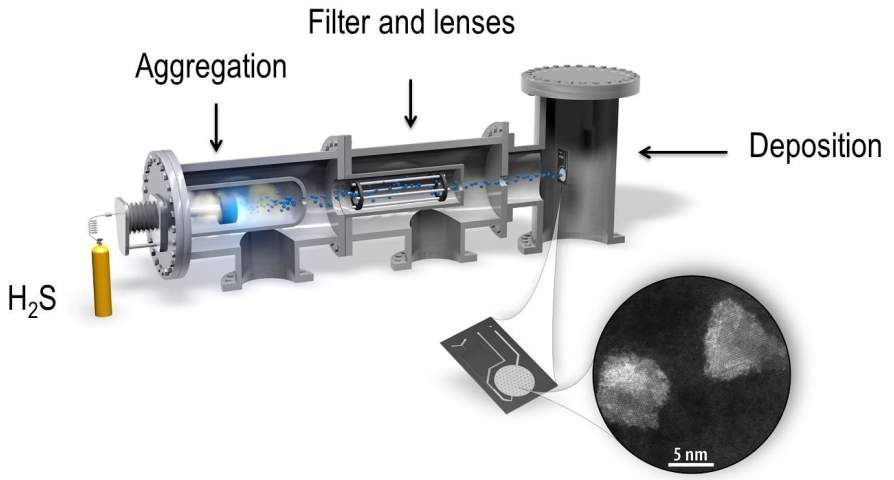

Figure 3.3: *The cluster source* STM 312 *where the target is sputtered to form a metal "vapor", which can agglomerate into clusters or in the aggregation zone, before they are mass-filtered and deposited directly into a µ-reactor. Image by Jakob Kibsgaard.*

enabling in-flight sulfidation of metallic nanoparticles, and H_2S was in this case introduced in this step.

The nanoparticles are accelerated and focused into a narrow beam, before pressure differences create a gas flow from the aggregation zone into the filtering zone. Most of the particles are charged and can therefore be filtered by an electric field in either a quadropole mass spectrometer (QMS) or a lateral time-of-flight mass filter (TOF-MS). The deposition of nanoparticles is controlled by measuring the deposition current when depositing directly into a µ-reactor.

Anodic bonding

After deposition, the reactor is sealed with a Pyrex lid by anodic bonding, also known as field-assisted thermal bonding [115]. In this process, a large negative bias (∼1 kV) is applied to the Pyrex, causing the alkali cations in the Pyrex to migrate away from the interface [116–118]. The result is an almost hermetic sealing between the silicon reactor and the Pyrex lid.

Since extensive heating is applied, an anodic bonding setup with cooling of

heat-sensitive areas was previously designed by Vesborg et al. [118], preventing potential sintering of catalyst particles. This can be seen from Figure 3.4.

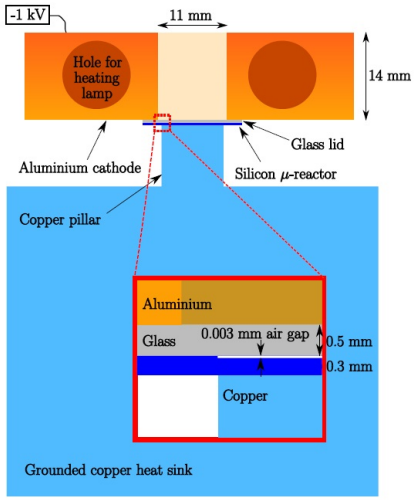

Figure 3.4: *The cold finger enabling cooling of heat sensitive areas. Reprinted from [118].*

In this setup, local cooling ensures that a minimum of heat is transferred to the reaction chamber, while the cathode is kept at high temperature and simultaneously heats the Pyrex lid.

No matter how practical this way of sealing the reactor seems, it unfortunately also has some drawbacks. Post-characterization of samples is not straightforward, due to the more or less permanent sealing between the Pyrex and the silicon. This means that all methods for opening the reactors are destructive. Additionally, great caution should be taken when preparing for the bonding process, since dust and other particles will prevent a perfectly alligned sealing, which cannot be corrected once the bonding process has been initiated.

3.2.3 Heating mechanisms

On the backside of the reactor a platinum resistance temperature detector (RTD) and two separate heating elements are deposited. Eight spring loaded

Au-coated pogo pins (see Figure3.5a) ensure contact to the platinum patches and the temperature is determined with a four-point-probe measurement of the resistance of the integrated RTD. From figure 3.1b a small Pyrex spacer covering the inlet and outles holes can be seen. This serves to protect the Kalrez O-rings seen in Figure 3.5a from being overheated and degrade, and also to improve the temperature distribution along the chip.

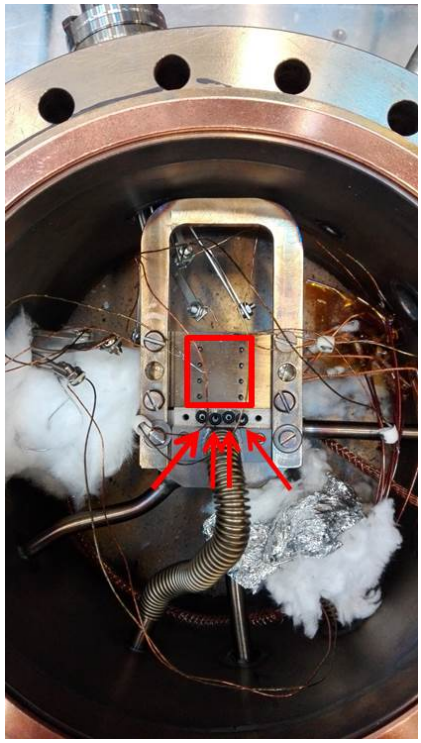

(a) *The inside of the containment volume without reactor.*

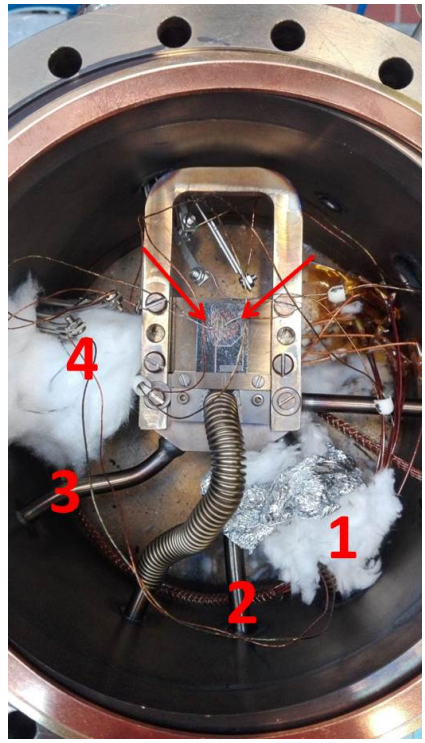

(b) *The inside of the containment volume with reactor.*

Figure 3.5: *The inside of the containment volume. In Figure 3.5a the red square marks the eight pogo-pins; the four arrows show the O-rings. Figure 3.5b shows arrows that point at the two thermocouples placed on top of a mounted reactor. The numbers indicate gas lines: 1) and 2) gas inlets 3) main outlet and 4) capillary outlet.*

Figure 3.5 shows a stainless steel manifold in which the reactor is fixed by tightening a bar over the inlet and outlet holes. The manifold is encapsuled in a stainless steel container which in daily terms is referred to as the containment volume, and this is sealed by Cu gaskets. It is connected to a roughing pump and can thus be evacuated to vacuum to minimize leaking of atmospheric air through the O-rings (they are not completely leak tight).

Inside the containment volume several thermocouples are mounted: one at each gas inlet line and one on the capillary gas line. Furthermore, two thermocouples are placed on top of the reactor lid. Initially, only one thermocouple was mounted in order to verify the temperature measured by the RTD mentioned above. At some point during a measurement it became clear that the RTD was not stable and that the temperature had been much higher than expected. The result was a reactor with a Pyrex lid completely deformed into a half sphere and a much increased reactor volume.

(a) *The result of a defect RTD heating reactor more than expected.*

(b) *The new arrangement for temperature measurements.*

Figure 3.6: *3.6a) A failed attempt to control the temperature by the RTD resulted in softening of the Pyrex lid. 3.6b) The following experiments were controlled by a thermocoupled mounted on top of the reactor, insulated by glass wool and kept in place by a mini CF blind flange.*

From this point we mounted an additional thermocouple and tried to insulate it with glass wool and a mini conflat (CF) blind flange as a partial fix - see Figure 3.6b.

Besides from keeping the surroundings under vacuum, the containment volume in this case also serves to ease the heating of the µ-reactor platform and corresponding gas lines. Since this is a substantial amount of stainless steel to be heated, an insulating unit made from two cylinders of aluminum stuffed with

glass wool was designed. Heating tapes are placed around the containment volume and the heating unit is designed so that it fits perfectly on top.

3.3 The better half

One of the greatest advantages of the µ-reactor design is the narrow capillary, which enables a direct connection to a mass spectrometer working under UHV conditions. Mass spectrometry is primarily concerned with measuring ions according to their mass-to-charge ratio (m/z) when moving at high speed in a vacuum [119]. The basic principles of a TOF-MS rely on Newton's laws of motion. Qualitatively this means that equally charged ions experiencing the same external force will have equal kinetic energy when moving in the same direction. The respective mass distribution will result in a corresponding velocity distribution (hence the name time-of-flight) inversely proportional to the square root of m/z.

Not only is the TOF-MS very convenient but it is also highly necessary in the analysis of heavy molecules like DBT and 4,6-DMDBT. Besides from its very high mass resolution ($m/\Delta m = 2500$) and a high mass range, the full range of masses are recorded simultaneously, and time resolved experiments can therefore easily be performed. The combination of the µ-reactor platform and the TOF-MS has been described in [111], and information on how and from which UHV components the setup was assembled can be found in [120]. However, extensive modifications were made during my time working at this setup.

3.3.1 Instrumentation

The TOF-MS basically consists of three regions (see Figure 3.7); the source region where the ions are created and accelerated, the field free region, which in daily terms is referred to as the flight tube, and the reflectron.

Two detectors are available, one behind the reflectron, and one next to the entrance of the flight tube. Only the latter comes into play in this work. The chamber has a 120 l/s ion pump, for pumping the flight tube, a 400 l/s ion pump and a 450 l/s turbo pump which both pump the source region. At a daily basis the base pressure is close to $\sim 10^{-11}$ mbar.

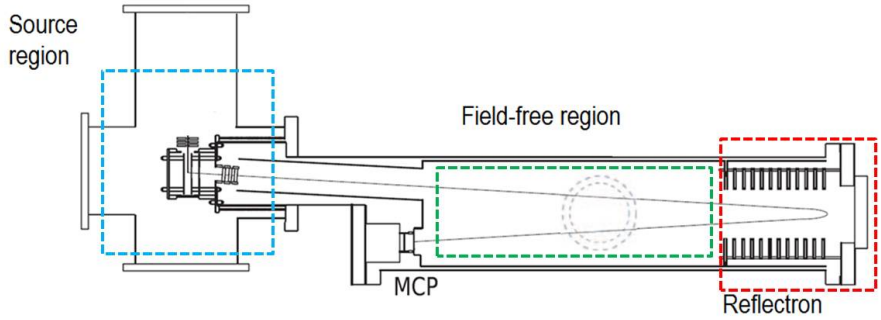

Figure 3.7: *A sketch of the TOF-MS. Blue square marks the source region, where ions are created and accelerated. Green square marks the field-free region (the flight tube) and the red square marks the reflectron.*

Ionization

Gas exiting the capillary outlet is led directly into the TOF-MS through an ionization zone. This is an essential step and also what caused most of the trouble during the last three years. As described in previous work conducted on the exact same setup, the original ionization source was made from a modified Bayard-Alpert ion gauge [120]. During the first two years of my PhD project the same configuration was used, but no matter what we tried, it seemed more or less impossible to gain a satisfactory signal intensity. In the first place we realized that the DBT was most probably deposited on the inner walls of the TOF chamber since the distance between the ion gauge and the internal lenses was too long. As an easy fix we mounted two light bulbs for internal heating and our suspicion was soon confirmed. After several discussions within the group we decided to implement some drastic changes to this part of the setup.

We agreed on a new ionization source originally intended for a QMS [121], and realized that it would require further re-arrangements of the entire ionization zone. Its gas-tight design lets the gas enter axially through a ceramic spring mounted fitting, which should be especially well-suited for small volumes of sample gas, or to reduce the background. The Bayard-Alpert ion gauge from before was removed, and instead we wanted to move the new ionization source as close to the internal TOF-MS lenses as possible. With great help from the workshop we managed to design a flange with four feedthroughs, a stabilizing

construction for the ion source, internal heating and thermocouples. The sketch of the new flange and its components can be seen in Figure 3.8.

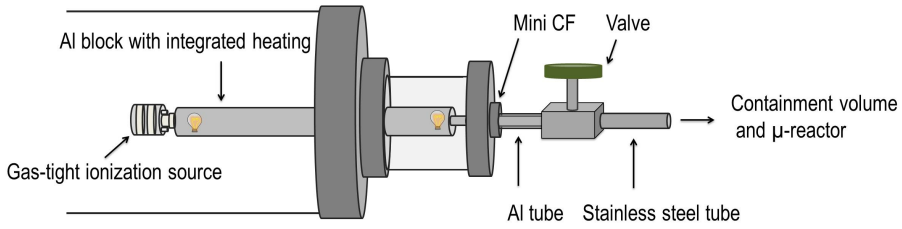

Figure 3.8: *A simplified sketch of the special designed flange with implemented ion source and internal heating. A stainless steel tube connects the capillary outlet and the TOF, separated by a valve. On the TOF-MS side of this tube, the inside is extended with an aluminium tube and an aluminium block with integrated light bulbs to enable internal heating in the TOF-MS.*

From the capillary outlet (through the containment volume) a stainless steel tube is connected to a valve, separating the µ-reactor platform and the TOF-MS and wrapped with heating tape. This part was re-arranged a couple of times, to minimize the length of the tubing. At the opposite side of this valve (facing the TOF-MS) the inside of the tube is extented with an aluminium tube. The stainless steel tube ends in a mini conflat (CF) at the entrance of the TOF-MS, while the aluminium tube proceeds inside. Here, it meets an aluminium block that has been designed so that its inner diameter fits the diameter of the tube. In the opposite end it meets the ceramic springmounted fitting of the ionization source. Furthermore, the aluminium block has been tailored so that a light bulb of 150 W fits in each end, enabling heat tracing all the way to the internal TOF-MS lenses.

The travelling ions

When gas molecules enter the new ionization zone they will collide with electrons continuously emitted from a hot tungsten filament at 28 eV and 1 mA leaving them positively charged. These values were a compromise between measuring a satisfactory reactant signal while at the same time suppressing the He signal.

Ions enter orthogonally to the flight direction where they meet a number of electrostatic lenses (A-E) which serve to focus the ions as well as possible. The

ions enter at the top of Figure 3.9a, before they experience a pulse of +800 V from the acceleration plate (A1) 4000 times per second.

Since the pulse is positively charged and the grid (A2) is grounded, the ions will be pushed away. In the ideal case, the ions will enter the region in the exact center between A1 and A2, leaving them with the potential energy of +400 V. The ions are accelerated by the negatively biased liner (L) at ∼-2500 V which pulls them down the flight tube. The liner is the inner out of two concentric tubes constituting the flight tube. Since the liner is kept at high voltage, the outside tube is grounded ensuring that the TOF-MS can be safely operated.

Before entering the flight tube, the ions are deflected (DEF) to what corresponds to an angle of 7 ° in order to compensate for the initial velocity orthogonal to the flight direction. Subsequently ions are focused (FOC) and accelerated away from the source region and into the field free region and the reflectron.

Ions will travel almost one meter, which is the length of the flight tube, before entering the reflectron (Figure 3.9b). The reflectron can be seen as a hilltop with respect to the total potential which the ions will experience during their journey. It serves to stop and re-accelerate them by pushing them symmetrically back through the flight tube with the same 7 ° tilt. At this point, the width of the peaks in the final mass spectrum is determined as is any dispersion in the flight velocity. Well through the mass spectrometer, the ions now reach the detector, which in this case is a micro channel plate (MCP).

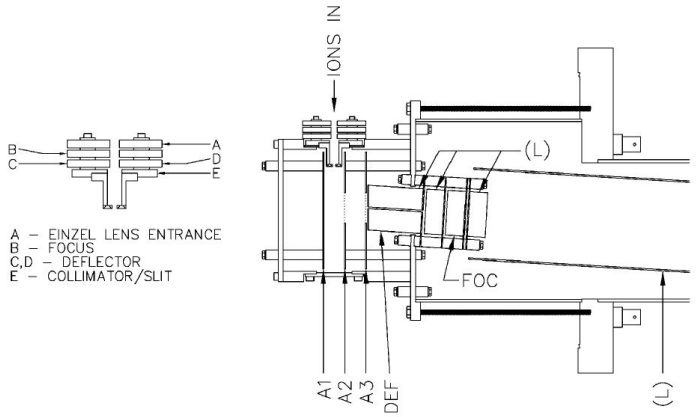

(a) *Source region.*

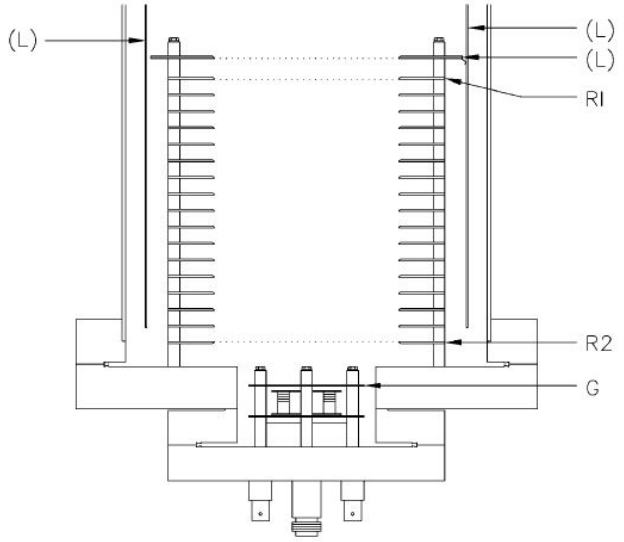

(b) *The reflectron.*

Figure 3.9: *Schematics of 3.9a) the source region where a set of Einzel lenses focuses the incoming ions before they are accelerated down the flight tube, and 3.9b) the reflectron of the TOF-MS where ions are stopped and re-accelerated back through the flight tube. Reprinted from [122].*

3.4 Reactant dosing

The µ-reactor platform has been developed for gas phase catalytic measurements, and since DBT and 4,6-DMDBT are both solid compounds at room temperature and ambient pressure, we had to come up with a clever way of introducing them into the system in their gaseous form. Several options were discussed and the combination of a solvent and a carrier gas seemed as the most convenient approach. However, since both molecules are quite heavy and have complicated cracking patterns in themselves, the use of solvent, hence more peaks to identify, would only further complicate the data interpretation. We therefore wanted to design a practical arrangement that took into consideration the physical properties of both compounds as mentioned in section 2.4.1 and use them as a guideline. Instead of using a solvent, helium was used as a carrier gas due to its inertness and low mass, which would not interfere with other masses in the cracking patterns. Having settled on these parameters, we needed to design a container from which the compounds could be dosed. This container will from now on be referred to as *source*. Different designs were tested during the last three years, and only recently the newest one was implemented. None of the designs have been flawless, and I am now certain that a better option exists, but it was not possible to implement this within the limited time frame (more on that in chapter 8). The only requirement for the source design was the need for a heat resistant material like stainless steel. Exactly how to proceed from that point was not obvious.

In the first design we aimed for a high dispersion of the compounds in order to increase the surface area from which they could evaporate upon heating. This resulted in two separate 1 m long cylinders with a volume of 500 ml each. Glass beads and the solid compound were added, the cylinder was evacuated to vacuum and heated to approximately 100 °C for 2–3 days. We hoped that this dispersion would ensure that the carrier gas was fully saturated with the respective compound before entering the reactor. For a long time this was the procedure, though we skipped the point of evacuating the cylinder and just refilled it and pumped it out through the reactor instead.

Within the last six months the latest source design was implemented. It is designed as a small stainless steel container with a mini CF window on top so it was clear when it was time for a refill. During measurements the window was covered with aluminium foil in order to avoid condensation of the crystals at the window.

3.5 The final setup configuration

When all the practical contents of the previous sections in this chapter are combined, they result in the final setup configuration as of today. A sketch can be seen from Figure 3.10.

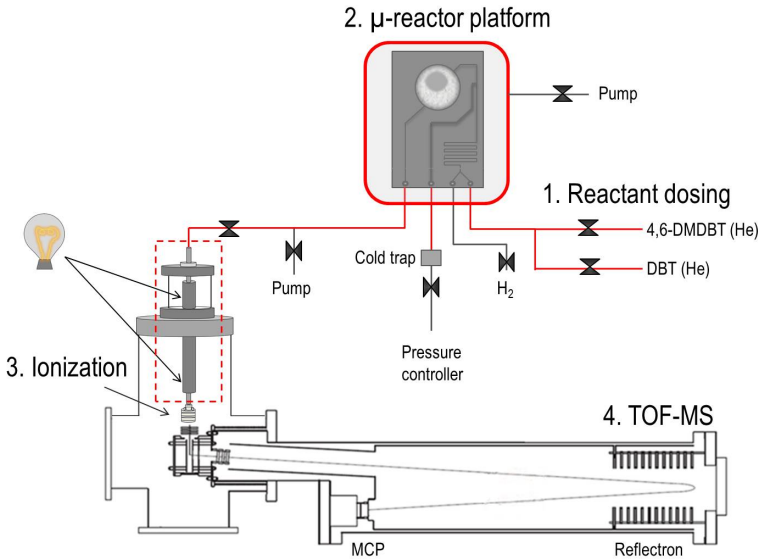

Figure 3.10: *The final setup configuration used for the experiments presented in this thesis. The four main parts are 1) the reactant dosing zone featuring two sources of DBT and 4,6-DMDBT, respectively. 2) The µ-reactor platform where the catalytic activity measurements are performed. 3) The new ionization zone featuring heat tracing to the Einzel lenses inside the 4) TOF-MS.*

The red lines indicate heat traced tubing from the reactant dosing zone to the TOF-MS. The outlet side of the containment volume is kept at 130 °C, and the bold red line surrounding the µ-reactor indicates the containment volume which is pumped by a roughing pump. When a new sample is mounted the capillary is pumped down through an alternative pumping way so that the TOF-MS can still be kept at UHV even though the µ-reactor platform is vented.

Even though both compounds are known to be very refractory, 4,6-DMDBT is still considered the worst. We therefore wanted to be able to test both DBT

and 4,6-DMBT back-to-back in order to compare their activity over relevant catalysts and detect their preferred reaction pathways. With this setup the catalyst was not exposed to air, as would have been necessary if only one source was connected at a time. As can be seen from Figure 3.10 the two sources are separated by valves but share the same gas inlet tube. Sources as well as gas lines were wrapped in heating tapes, and thermocouples were attached in the reactant dosing zone, the containment volume and the TOF-MS. The positions are listed in Table 3.1.

Table 3.1: *Overview of thermocouples monitoring the temperatures in the reactant dosing zone, the containment volume and the TOF-MS.*

Reactant dosing	Containment volume	TOF-MS
DBT valve	Reactor lid x 2	Al-block
DBT source	DBT/4,6-DMDBT line	New flange
4,6-DMDBT source	Capillary line	Inlet valve
4,6-DMDBT valve	Vacuum	-
-	Main outlet	-

As is obvious from the number of thermocouples in Table 3.1, controlled heating of the entire setup was a tricky task, and since the thermocouples might have been slightly displaced from time to time, the heating was never more precise than this. The number of thermocouples did, however, enable us to followlw the heating quite closely.

Chapter 4

Data treatment

The advantages of using an advanced mass spectrometer like the TOF-MS could not be fully exploited without an additional number of technical equipment to support the operation and data acquisition. At the same time, the amount of data and the related data interpretation is quite substantial, and a chapter of its own is therefore dedicated to a description hereof.

4.1 Electronics and data acquisition

Aside from all the vacuum components which make up most of the physical appearance of the TOF-MS, a large number of electronic devices drive the instrument. As already mentioned, several high voltage supplies are necessary for running the liner, focus lens , deflection plate , acceleration plate, reflectron voltages and the MCP detector. Furthermore, the five entrance lenses (A-E) shown in Figure 3.9a all need different voltages. The disadvantage of this is, however, not the number of power supplies but the enormous parameter space that needs to be considered when optimizing the system. The basic settings were adjusted whenever the chamber had been baked or shut down for other reasons.

As previously mentioned, a pulse of +800 V is initiated at the acceleration plate, A1, with a frequency of 4000 Hz. Whenever a pulse is initiated, a multiple-event digitizer (model $MCS6A$[1]) is notified and starts detecting the number of ions

[1] The time resolution of this device is 400 ps, which is much faster than a peak width.

that reaches the MCP, referred to as counts. This number depends on the number of iterations, i, according to equation 4.1

$$\sum i = \nu\tau \tag{4.1}$$

where ν is the pulse frequency and τ is the iteration time. This should be at least 250 µs which corresponds to 4000 Hz. But since the number of counts within this timeframe is limited, the TOF-MS signal intensity is limited as well.

The TOF-MS signal intensity, I, will therefore scale with the number of iterations

$$I_t = \sum_i I_{t,i} \tag{4.2}$$

where i is the iteration and t is the flight time of a given ion.

In order to compare spectra obtained at different iteration times, one should normalize to the number of iterations.

$$< I_t >= \frac{\sum_i I_{t,i}}{\sum i} \tag{4.3}$$

For most of the experiments included in this thesis, scans of $2.4 \cdot 10^5$ iterations were recorded every second minute during most of a day, producing sometimes more than 1000 individual spectra. It is obviously an enormous amount of data to store, and going through every spectrum in detail is quite an immense task.

4.2 TOF data

The raw spectra obtained from the TOF-MS are plotted as the number of counts (TOF signal intensity) as a function of flight time (µs). For most people this seems rather useless and impossible to interpret. It is therefore helpful to know how to derive m/z from the flight time. Additionally, complete data set consisting of more than 1000 spectra have to be presented in the most simple, yet suitable way.

4.2.1 From time to mass

The transformation of the time axis into a mass axis is not a trivial task. As mentioned in section 3.3, mass scales with the square root of the flight time - this can be seen in the reference spectra obtained for both DBT (Figure 4.1) and 4,6-DMDBT (Figure 4.2).

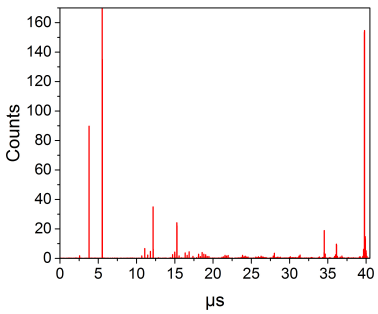

(a) Spectrum of DBT as a function of time.

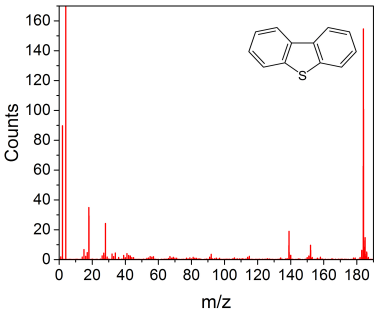

(b) Spectrum of DBT as a function of mass.

Figure 4.1: *Spectrum of DBT as a function of time and mass. The lower masses are more clearly separated at the time axis than the mass axis. This is explained by a square root relation between time and mass.*

In order to perform this transformation different approaches exist. In previous work [111] it was shown how known geometric dimensions from CAD drawings of the TOF-MS can be combined with measured voltages to calculate the flight time of the entire range of masses. However, the accuracy of this estimation is only approximately one amu, which makes it difficult to separate individual masses and therefore does not do the TOF-MS justice. Another drawback in this approach is the fact that the flight tube will mechanically expand with temperature of the surroundings, changing the flight path and therefore also the flight time.

Another approach which offers much more accurate results is to fit peaks of already known masses. In this way five or more known compounds are selected and peaks are fitted to their respective masses. This results in an accuracy of around 0.05 amu, and is therefore the go-to approach used in the present work.

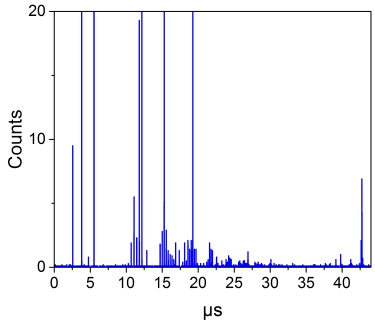

(a) Spectrum of 4,6-DMDBT as a function of time.

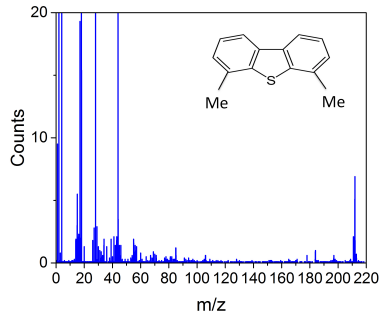

(b) Spectrum of 4,6-DMDBT as a function of mass.

Figure 4.2: *Spectrum of 4,6-DMDBT as a function of time and mass. The lower masses are more clearly separated at the time axis than the mass axis. This is explained by a square root relation between time and mass.*

In reality, a Python script was written for this task and can be found in [123] if interested.

4.2.2 Spectrum plotter

For the sake of keeping track of the large number of mass spectra, a procedure for handling the heavy amount of data had to be established once experiments started runnning. In that connection, my colleague Robert Jensen assisted in developing software to plot the evolution of specified peaks as a function of time and temperature [124]. This is considered a reasonable approach since the peak intensities are proportional to the concentration of the respective compounds. It is, however, very important to mention the compound specific ionization cross section. When interpreting the evolution of the signals as just described, one should keep in mind that the signal intensities of two different compounds cannot be directly compared since one compound may be easier to ionize than the other. However, it has not been possible to find the ionization cross sections for most of the relevant species considered in this thesis, and the raw signals are therefore presented instead. In terms of describing conversion, a sensitivity factor, x, is estimated later in the process and will be discussed in chapter 6. Regardless of the lack of ionization cross sections, spectra should of course

still be investigated in order to see if any new features appeared and should be included in the plots, and to ensure that only one compound is present at a desired peak position.

Once the compounds of interest have been identified, the integrated area of the base peaks (specified in the Python script) can be plotted over an entire experiment. In practice, the Python script performs a Gaussian peak fit and normalizes the integrated peak area to the number of iterations. An example can be seen from Figure 4.3.

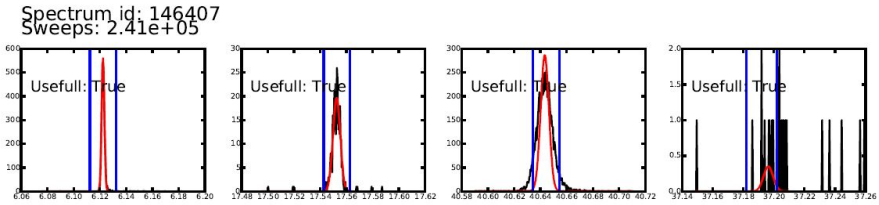

Figure 4.3: *An example of the Gaussian peak fits performed in the plotting of specified peaks and their evolution. "True" indicates that the script has identified a peak and made a successful fit.*

The Gaussian peak fits are used as a means to find the integrated peak area normalized to the number of counts and information about the evolution in reactants and products can thereby be derived. What should however be noticed is that a drift in the voltages from the power supplies might evoke dislocations of the peaks along the time axis which will cause misinterpretation of the data if the peak positions are not corrected in the Python script before plotting. Furthermore, peak intensities are also heavily dependent on the stability of the power supply and can therefore vary accordingly, which will be observed in the following results.

4.2.3 Data presentation

In the following chapters the data will be presented as explained in this chapter. When raw mass spectra are presented, they will be imaged as the m/z as a function of counts. The Python script plots the evolution of specified masses represented by the normalized integrated peak area found by a Gaussian peak fit as a function of time. These are co-plotted with temperature profile and can

be seen as the summary of an experiment. This type of plots will be reffered to as activity plots.

Chapter 5

Experimental procedures

The task of introducing the reactant compounds into the system was without a doubt the most complex and time-consuming factor in the process towards enabling activity measurements. Some of the artefacts complicating the process even more was discovered only recently but will be introduced in this chapter in order to get a more coherent overview of the following results.

5.1 The model compounds

As stated several times through this thesis, it is well known that both DBT and 4,6-DMDBT have low vapor pressures. In order to get an idea about how we could expect the compounds to behave, going through literature and the NIST database was the obvious choice. However, information on these compounds was not readily available.

We managed to find some reported physical properties of DBT [101], indicating how much heat should be applied in order to introduce it through the µ-reactor. The same kind of data was pursued for 4,6-DMDBT but is to my knowledge not available. However, at room temperature the vapor pressure of 4,6-DMDBT is approximately one tenth of the vapor pressure of DBT [103] and only makes matters worse. Based on calculated and measured data from Edwards et al. [101] the vapor pressure of DBT can be depicted as a function of temperature as shown in Figure 5.1.

Here, it is clearly seen that DBT needs a high temperature before a reasonable

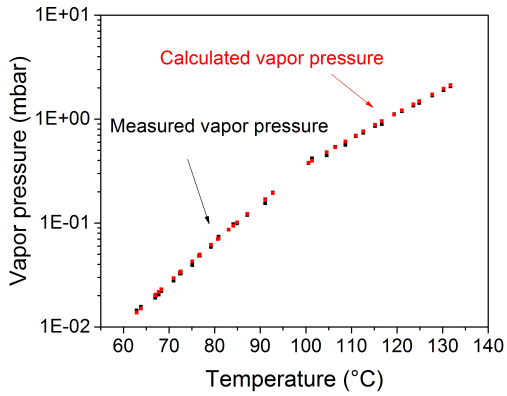

Figure 5.1: *Measured and calculated vapor pressure of DBT as a function of temperature. Based on data from [101].*

vapor pressure is reached. To avoid condensation of DBT (or 4,6-DMDBT) and clogging of pipes, everything downstream from the source should ideally be heated even more. At some point it became clear that DBT should be heated to temperatures above its melting point, typically around 110 °C hence resulting in a DBT vapor pressure of ∼0.6 mbar.

Most experiments were conducted at 800 mbar. In reality, this was the result of our initial attempts to dose DBT through the reactor at 200 mbar and a subesequent twofold doubling of the pressure. It was a compromise between the TOF-MS signal and the relative amount of DBT in the reactor which only accounted for a very small part of the total gas composition in the reactor (<1 %). The experimental test conditions illustrated in Figure 5.2 soon became implemented as default settings. These conditions apply when the source temperature is kept at 110 °C, hence resulting in a partial pressure of 0.4 mbar in the reactor.

Whenever a reactor was mounted in the stainless steel manifold, the pressure controller was set to 1200 mbar in order to investigate if the sealing between the reactor and the O-rings was properly tight. If the pressure approached ambient pressure, it was a failed attempt and this step was repeated until satisfactory. Subsequently the pressure was stepwise decreased to zero, and the capillary pumped down as well. At this point in the process it is also important to make

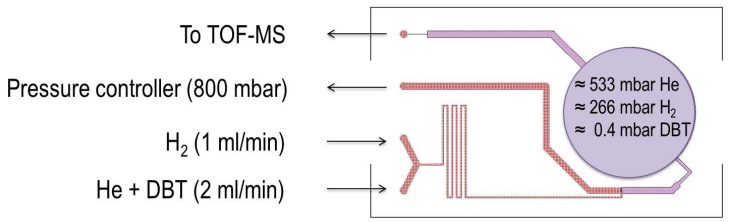

Figure 5.2: *The gas composition during applied experimental conditions (in the HDS of DBT): 2 ml/min DBT in He, 1 ml/min H_2, a total pressure of 800 mbar resulting in a partial pressure of DBT of 0.4 mbar.*

sure that the springmounted pogo pins are in physical contact with the Pt heating elements on the backside of the reactor, so that heating of the reactor is possible. Only then the thermocouples, glass wool and mini CF is placed on top of the reactor as shown in Figure 3.6b, and the containment volume evacuated to vacuum.

After a vaguely defined period of time of pumping down the gas lines (preferably overnight) the valve between the µ-reactor platform and the TOF-MS is opened and a series of scans initiated.

Dibenzothiophene through µ-reactor

As established above, the source was operated at elevated temperatures, and the remaining parts of the setup was ideally kept even warmer. This meant that after the above mentioned procedures, but before heating the source and initiating an experiment, the containment volume and both source valves were heated to temperatures slightly higher than the applied source temperature, which in the case of DBT was 110 °C. An example of the evolution of the integrated peak area of DBT as a function of time while heating the µ-reactor platform can be seen from the activity plot in Figure 5.3. The TOF signal in terms of the integrated peak area is read from the left y-axis while temperatures are read at the right y-axis. Before heating the source, it was made sure that potential adsorbed species had degassed from pipes and catalyst so that the TOF signal of the model compounds were dosed from the inlet side of the reactor.

The solid red line shows the containment volume temperature as measured on top of the µ-reactor. The dashed red line shows the temperature measured by

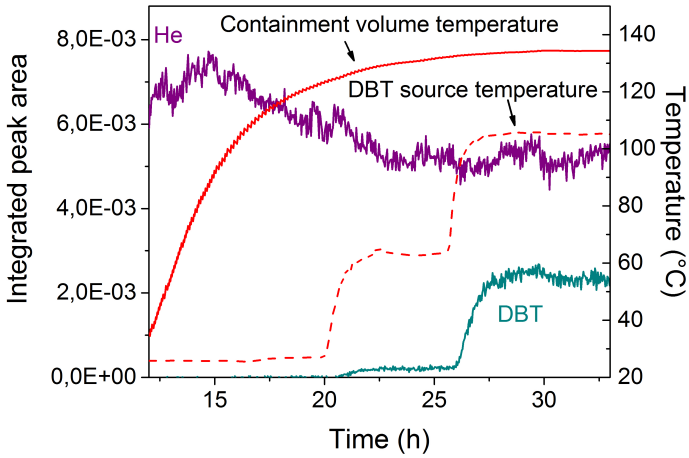

Figure 5.3: *The evolution of DBT as a function of time while heating the containment volume, source valve and source.*

the thermocouple located at the DBT source, and in that connection several features need to be explained.

The first shoulder in the source temperature is caused by heating of the source valve, but since they are physically close, some heat transfer to the source will occur. At the same time the DBT signal (greenish-blue) obviously starts to increase which was frequently observed during this procedure. It is caused by deposition of the DBT at the inside walls of the tubing and valve which was difficult to completely avoid.

The second shoulder is the result of the actual heating of the source. What can also be observed is the decrease in He signal over time. As mentioned in section 3.2.1, the capillary flow will decrease with increasing temperature, and is therefore in good agreement with what is observed in this case.

As a measure of the relative signals a blank reactor was tested. Applied reaction conditions were as shown in Figure 5.2 over a temperature ramp from 170-380 °C (and down again) with steps of 15 °C and 30 minutes per step. Hydrogen is left out in this plot on purpose due to a very dominating signal. In this way, details about the remaining compounds are more easily observed. The potential products, BiPhe and H_2S are included in the plot, but are basically non-existent

and emphasize the inactivity of a blank reactor. The result can be seen from Figure 5.4.

As is obvious from this plot, no conversion of DBT occurred which can be seen in the lack of BiPhe and H_2S (CHB was left out of the plot because the peaks were simply too small to fit). However, in this case and opposite to what was

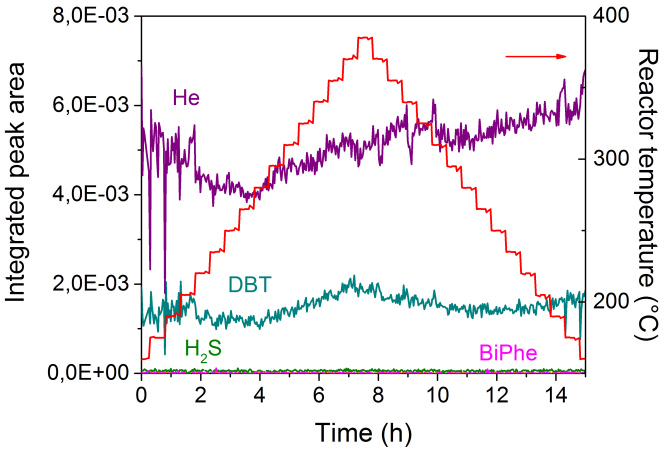

Figure 5.4: *DBT through an empty reactor. The left y-axis shows the integrated peak areas of DBT and He (no H_2S or BiPhe is observed). The red curve shows the temperature ramp of an experiment and is read at the right y-axis.*

observed in Figure 5.3, the He signal seems to increase with time and does not follow the same trend as would have been expected with increasing temperature.

No outright explanation could be found for this gas signal behavior. We discussed it within the group and the most reliable explanation we could come up with was the fact that something inside the TOF-MS is mechanically strained or stretched with temperature.

4,6-Dimethyldibenzothiophene through µ-reactor

Only within the last six months, 4,6-DMDBT was succesfully introduced into the µ-reactor, and if we thought that DBT was a complicated affair, we were

about to get an unpleasant surprise. Since experience from DBT indicated that heating above its melting point was necessary, we encountered physical limitations of the equipment when shifting to 4,6-DMDBT.

The internal parts of the containment volume, specifically the wires connecting the pogo pins through a feedthrough, should not be exposed to temperatures much higher than 150 °C, which was not a problem during the experiments with DBT. However, since the melting point of 4,6-DMDBT is 153 °C, this restricted the being able to use the same procedure, and we hoped that small amounts of 4,6-DMDBT could be observed at temperatures below the melting point.

At first, it seemed more or less impossible to get this compound through the system. Even though both the source and its valve were heated to approximately 130 °C, degassing of DBT was the only thing observed, as can be seen in Figure 5.5.

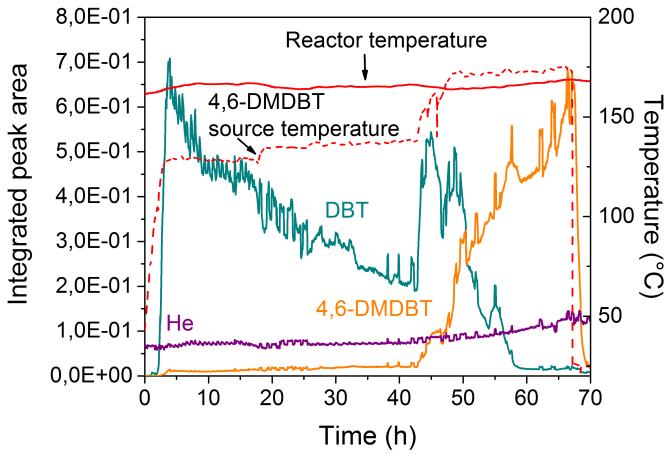

Figure 5.5: *The evolution of 4,6-DMDBT as a function of time while heating the 4,6-DMDBT source. The left y-axis shows the integrated peak areas of 4,6-DMDBT, DBT and He. The red curves show the temperatures of the source (dashed line) and the reactor temperature (solid line) and are read at the right y-axis.*

When dosing DBT the 4,6-DMDBT valve was closed and vice versa, resulting in a small volume of stagnant gas in front of the closed valve. The reason for this amount of DBT degassing is therefore attributed to this setup configura-

tion where gas is suddenly pushed through the aforementioned stagnant volume when shifting between the two sources. After degassing for more than 40 hours at 130 °C the source was basically empty and no significant increase in TOF signal had appeared. Looking back, it would have probably been wise to accept the limited signal. Instead, the 4,6-DMDBT source temperature was further increased and the compound suddenly seemed to get through. Not until the next reactor was mounted did we realize that the 4,6-DMDBT was not only deposited at the inside of the gas lines, but had accumulated and completely blocked the main outlet in the valve between the reactor and the pressure controller. The valve and tube were therefore disconnected and cleaned, and this experience led us to develop a cold trap (see Figure 3.10) in order to prevent similar scenarios in future experiments.

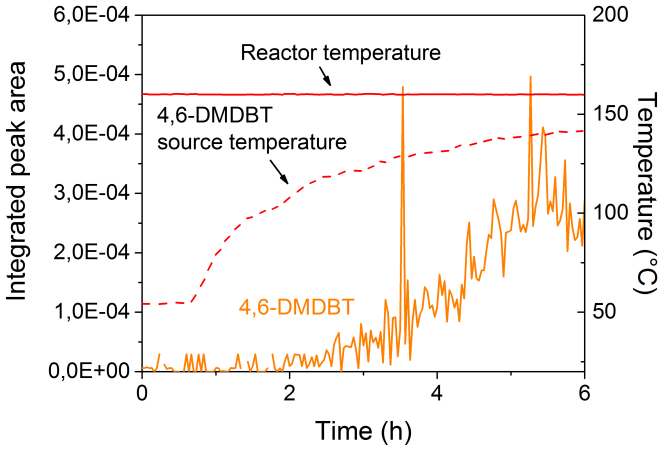

Figure 5.6: *The evolution of 4,6-DMDBT through empty µ-reactor at the final settings. The left y-axis shows the integrated peak areas of 4,6-DMDBT and the red curves show the temperatures of the source (dashed line) and the reactor temperature (solid line) and are read at the right y-axis.*

Since then, it has been possible to introduce 4,6-DMDBT through the µ-reactor in a more controlled manner. However, the peak intensities never reached the same level as we experienced during the accumulation in the outlet valve. But in reality, it would have been difficult to determine whether the intense signal originated from degassing at the outlet side of the reactor or the source. An

example of the evolution of 4,6-DMDBT with time and temperature can be seen from Figure 5.6. The signal in this plot is quite noisy, which is difficult to avoid when dealing with such small signals.

Furthermore, a temperature ramp was also performed for 4,6-DMDBT to rule out any conversion through an empty reactor. In this case 3,3'-DMBiPhe is included as an example of the most probable product in the activity plot, Figure 5.7, but again peaks can barely be seen and are likely non-existent.

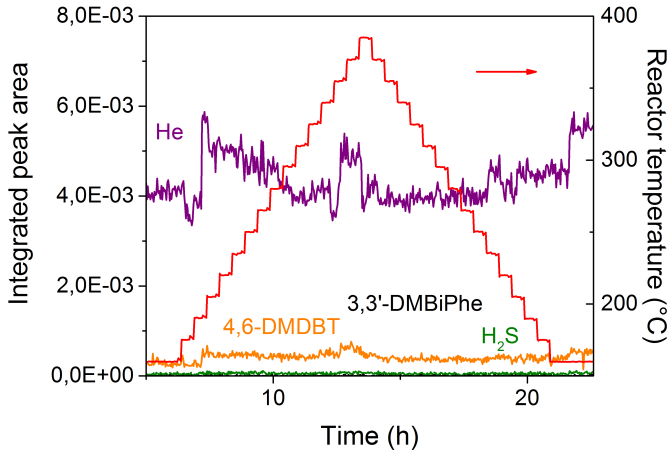

Figure 5.7: *4,6-DMDBT through empty reactor under typical reaction conditions. The left y-axis shows the integrated peak areas of 4,6-DMDBT and He (no H_2S or 3,3'-DMBiPhe is observed). The red curve shows the temperature ramp of an experiment and is read at the right y-axis.*

5.2 The jokers

For a substantial amount of time a few phenomena kept on blurring the results. We did not realize the underlying reasons nor did we comprehend the effects until recently. A short discussion serves to unravel some of the mysterious features - the jokers - which can be observed in the following results.

5.2.1 The unidentified peak

During the process of determining appropriate test conditions for the activity measurements, a commercial supported catalyst was provided by Haldor Topsøe A/S. We knew what products to expect, but the only peak appearing with an increase in temperature was $m/z = 85$ and unidentified. Quite some time was spent speculating about what this could be. At some point we decided to leave out helium, hence DBT, and therefore also leave out any reactants, in order to exclude catalytic conversion. The result can be seen from Figure 5.8a.

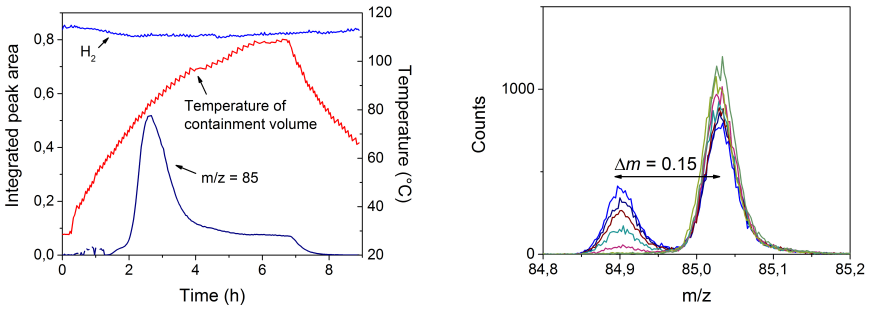

(a) *The evolution of mass 85 with heating.* ***(b)*** *Two peaks separated by 0.15 amu.*

Figure 5.8: *The ever appearing mass 85. Figure 5.8a shows the substantial degassing of the O-rings. and Figure 5.8b shows two peaks separated by less than one amu, which illustrates the high resolution of the TOF-MS.*

The containment volume was heated as usual and we soon came to realize that the compound, whatever it was, originated from the tubing made from stainless steel or something related to the reactor itself. The situation was a bit critical since the reactor was supposed to be an excellent inert substrate for the nanoparticles we were planning to deposit and test. Unidentified peaks were the

last thing we needed in a spectrum of a heavy compound with already many peaks.

Going through literally all spectra of compounds with a molecular mass of 85 at NIST did not clarify matters. Expanding this to a detailed investigation of every peak in the spectrum finally paid off. At $m/z = 104$ the mystery was solved and the compound we had been chasing revealed itself as SiF_4, most probably originating from the O-rings. The mass spectrum of SiF_4 has its base peak at $m/z = 85$, which is why the identification was difficult. In future data interpretation this peak will be notated SiF_3, since this corresponds to the fragment at $m/z = 85$.

Even though the O-rings were supposed to be inert and leak tight to operating temperatures above 300 °C, they were apparenly degassing well below this point. In that connection, we realized that the beauty of the TOF-MS and its high resolution had also become a curse. This is well demonstrated in Figure 5.8b where two peaks are separated by less than one amu. From that point on, the O-rings were degassed at 300 °C overnight in a H_2 atmosphere before use.

5.2.2 An unfortunate correlation

For a long time it had been clear that the source temperatures were not stable even though the same conditions were applied from time to time. Since the sources were heated by heating tapes and insulated by aluminium foil, one explanation could be the change in the indoor temperature in the experimental hall varying from day to day if the source was insufficiently insulated. Another straightforward explanation could be that the thermocouples were not placed at the exact same place from time to time. However, we were focused on measuring samples and not so much on the actual data interpretation at that point.

The problem was as such not the varying DBT signals, since these appeared to correspond impeccably with the temperature changes. The problem arose in the data interpretation when the activity of different samples and conversion of DBT and 4,6-DMDBT were attempted. No amounts of aluminium foil did however seem to be sufficient for the insulation task.

During one of the last group meetings we discussed the probability of fluctuations in the grid voltage of 230 V. Fortunately this is a voltage that is logged in our laboratory and could therefore readily be investigated. The result can be seen from Figure 5.9.

As can be seen, the temperature varies within a range of five degrees. However, since the vapor pressure is a logarithmic function of the temperature these

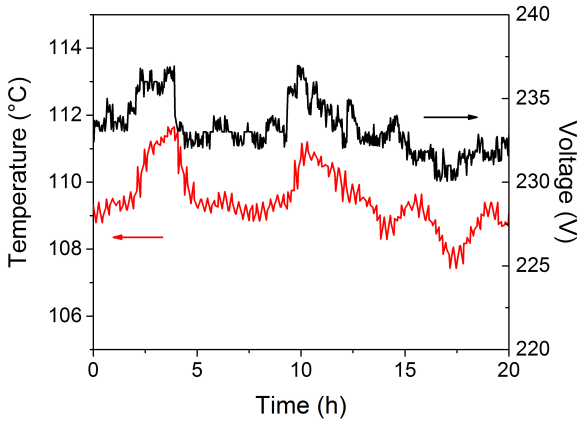

Figure 5.9: *The correlation between fluctuations in the voltage grid and the source temperature.*

variations result in substantial changes in the DBT signal. During activity measurements these are very unfortunate since it can be difficult to separate conversion from this effect. However, the source temperature can only account for some of the variations in DBT.

During the final activity measurement, it became clear that the initial intensity of DBT was extremely low, despite the fact that the temperature settings had not been changed. At that point another unfortunate effect revealed itself. Previously, low intensities of DBT before initiating experiments had been explained by the change in capillary width. Since the intensities of all peaks had suddenly seemed to decrease by a factor of ten, we decided to go through the settings of some of the technical equipment behind. In that connection it was found that the voltage driving one of the internal TOF-MS lenses had been drifting drastically. Few days after it was clear that the same phenomena could be observed again, and the voltage supply was obviously facing the end of its life. The effect of this drift will be evident for some of the results presented in chapter 6.

Chapter 6

Unsupported mass-selected Pt Nanoparticles

After the amount of time spent on optimizing and re-building the experimental setup it was in everyones interest to prove the advanced technical aspects in catalytic tests of well-defined model systems. Mass-selected nanoparticles were synthesized by my good colleagues, PhD students Anders Bodin and Jakob Ejler Sørensen and characterized by Anders Bodin and Christian Fink Elkjær, who has a postdoctoral position at Haldor Topsøe A/S in the Hydecat project. I was responsible for the catalytic activity measurements and everything related to this myself.

6.1 Pt as a HDS catalyst

Conventional HDS catalysts typically consist of MoS_2 nanoparticles promoted by either Ni or Co as explained in chapter 2. These are very complex systems, where composition, structure and preparation method all affect the catalytic activity [43, 71, 72]. For the purpose of establishing experimental procedures on a given setup, a more simple approach is therefore to study monometallic catalysts.

To promote the hydrogenation of the aromatic rings, noble metals have been investigated in the HDS of both DBT and 4,6-DMDBT due to their exceptional

hydrogenation activity [10, 12, 48, 125–127]. Different outcomes have been reported, though it is generally said that HDS of DBT follows the DDS pathway, whereas the HDS of 4,6-DMDBT requires hydrogenation of one of the aromatic rings prior to sulfur extraction. Niquille-Röthlisberger et al. [125] found that 85 % of the HDS of 4,6-DMDBT occurs through the HYD pathway and 15 % through the DDS pathway at 300 °C and 50 bar over alumina-supported Pt.

Other studies have shown that Pt favors the DDS pathway in the HDS of both DBT and 4,6-DMDBT under industrially relevant pressures [128] as well as atmospheric pressure [129], hence resulting in BiPhe and 3,3'-DMBiPhe, respectively. Finally, studies by Baldovino-Medrano et al. [130] and Chen et al. [131] suggest that the desulfurization of 4,6-DMDBT on noble metal based catalysts is similar through both the DDS and HYD pathway.

6.2 Mass-selected Pt nanoparticles

Ten reactors with mass-selected Pt nanoparticles were prepared. Difficulties in the bonding process, unsuccesful mountings and defect Pt heating elements on the backside of the reactors, resulted in only four reactors suitable for catalytic tests: two reactors with 185 kamu nanoparticles (~ 3 nm) and two reactors with 1500 kamu nanoparticles (~ 6 nm). All four reactors had been deposited with a loading of 10 % (projected surface area).

Table 6.1: *Overview of mass selected Pt nanoparticle samples.*

Sample (ID)	Size (nm)	Mass (kamu/ particle)	Number of particles (sample)
MR-04	3	185	$9.02 \cdot 10^{11}$
MR-06	3	185	$9.02 \cdot 10^{11}$
MR-01	6	1500	$2.23 \cdot 10^{11}$
MR-02	6	1500	$2.23 \cdot 10^{11}$

Particles prepared under similar conditions were deposited onto lacey carbon covered Cu grids and characterized by TEM. The resulting particle size distributions can be seen in Figure 6.1. Size and shape are uniform and especially for the 185 kamu sample the size distribution is narrow, whereas two maxima can be observed for the 1500 kamu sample. The second maximum appears because some of the particles will carry double charge and double mass (*2m/2z*)

and therefore pass the mass filter exactly like the single charged particles in the cluster source.

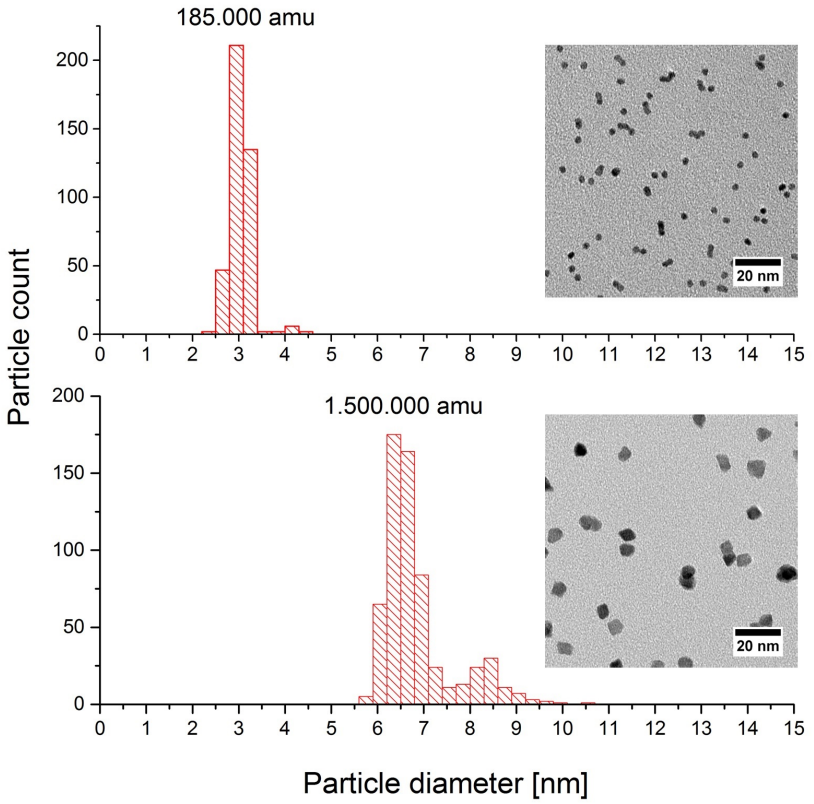

Figure 6.1: *Particle size distribution of mass selected Pt nanoparticles of 185 kamu (∼3nm) and 1500 kamu (∼6nm), respectively. TEM images show particle sizes and shapes. The particles were deposited on lacey carbon covered Cu grids under similar conditions as the μ-reactor samples. Image by Anders Bodin.*

6.2.1 HDS of DBT

The experimental conditions explained in chapter 5 were applied during all experiments presented in this chapter. The same temperature program was followed, however, a mistake in the file running the program resulted in a different temperature ramp for one of the 185 kamu samples (MR-06).

The flows were stabilized, the containment volume and the DBT source heated and the DBT signal stabilized as well as possible. Altogether, these pre-experimental procedures typically took more than 12 hours.

In order to pinpoint which products were formed (hence which peaks to fit in the activity plots), the recorded spectra were examined. An example of spectra

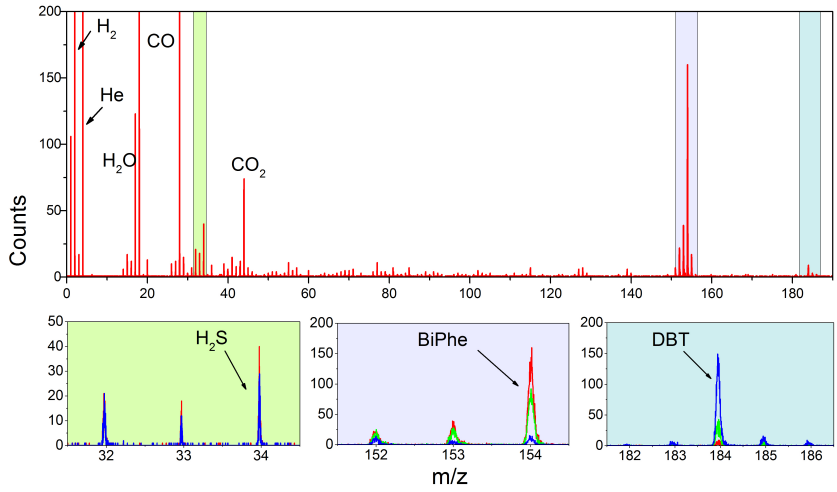

Figure 6.2: *TOF mass spectrum of the HDS of DBT on a 1500 kamu (∼6 nm) Pt sample (MR-02). The red and uppermost spectrum was obtained at 350 °C and shows masses* m/z = *0-190. The insets below illustrate close-ups of three regions. In all insets the colors indicate: red spectrum: 350 °C; green spectrum: 275° C; and blue spectrum: 200 °C.*

recorded at three different temperature steps in the HDS of DBT on a 1500 kamu Pt sample can be seen in Figure 6.2. Corresponding spectra for the three other samples can be found in Appendix A.

The uppermost TOF spectrum was obtained at 350 °C - this is also included in the insets below (red) together with spectra obtained at 200 °C (blue) and 275 °C (green).

What is readily observed is the number of peaks below $m/z = 50$. Besides from H_2 and He which are introduced through the µ-reactor, H_2O, CO and CO_2 can also be observed. Water is by definition difficult to get completely rid of in a UHV chamber, whereas CO and CO_2 are assigned to adsorbed carbon species degassing from the surface of the filament. One of the peaks in the same mass range is found at $m/z = 34$ and can also be seen in the leftmost inset below. It corresponds to the formation of H_2S - a product of the HDS reaction.

In the high mass range primarily two peaks dominate. The intense peak at $m/z = 154$ shows the formation of BiPhe, whereas the small peak at $m/z = 184$ shows the depletion of DBT. Since no other products than BiPhe and H_2S are observed, the DDS pathway must be assumed to prevail under these reaction conditions. This corresponds well with findings of Haji et al. [132], who tested Pt-based catalysts in the HDS of DBT in the temperature range 310-400 °C at atmospheric pressure.

Having identified the reaction products, activity plots were created - see Figures 6.3 and 6.4.

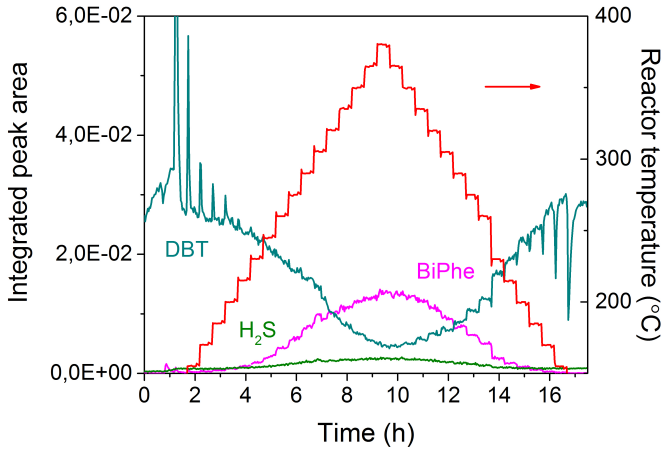

(a) HDS of DBT on 3 nm Pt (MR-04).

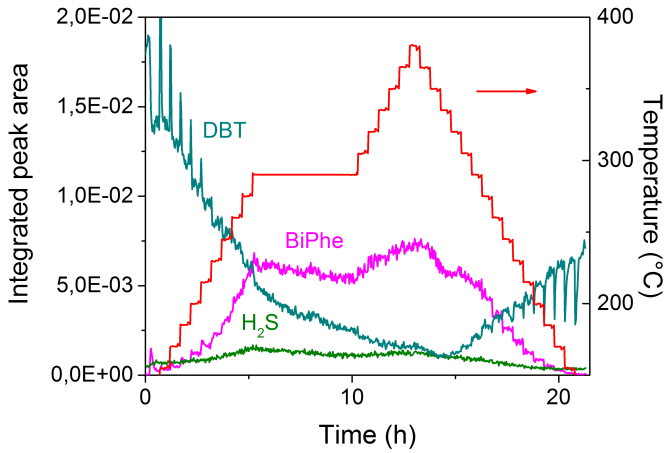

(b) HDS of DBT on 3 nm Pt (MR-06).

Figure 6.3: *HDS of DBT on 3 nm Pt samples. The left y-axis shows the integrated peak areas of DBT, BiPhe and H_2S. The red curve shows the temperature ramp and is read at the right y-axis.*

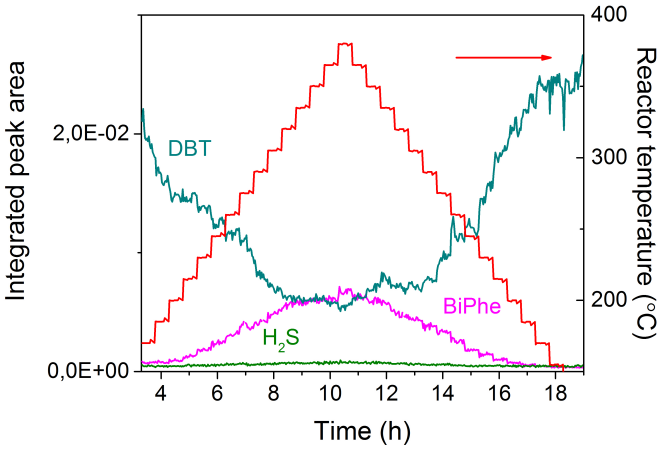

(a) HDS of DBT on 6 nm Pt (MR-01).

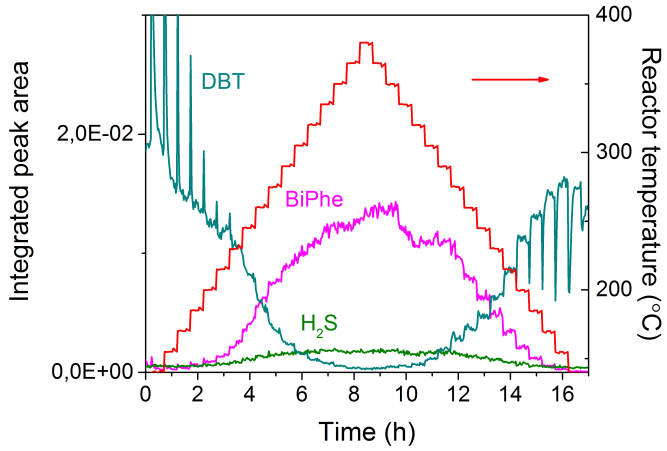

(b) HDS of DBT on 6 nm Pt (MR-02)

Figure 6.4: *HDS of DBT on 6 nm Pt samples. The left y-axis shows the integrated peak areas of DBT, BiPhe and H_2S. The red curve shows the temperature ramp and is read at the right y-axis.*

In all four measurements significant variations in the DBT signal can be observed. However, the large spikes are not related to the unstable DBT temperature mentioned previously, but degassing of adsorbed DBT from the catalyst surface due to the sudden heating. It seemed difficult to avoid and therefore means that the partial pressure of DBT is transiently higher (lower at the temperature ramp down) at the time of the spikes than what can be estimated based on the measured DBT source temperature.

What can also be observed when comparing the four plots is the different DBT level from sample to sample at the point of initiating the experiments. These variations were discussed heavily and for a long time it was designated to possible variations in the capillary width, but since the operating pressure of the TOF-MS did not vary much this was ruled out.

Since it was difficult to establish the exact initial DBT level, conversion was defined as the products formed at time t relative to the combined reactant and product signal at the same time. However, since ionization cross sections were not available, a sensitivity factor was derived, based on one of the 1500 kamu samples (MR-02).

6.2.2 The sensitivity factor

As can be seen from Figure 6.4b the sample approaches full conversion and DBT is practically depleted at the highest reaction temperature of 380 °C. Since the ionization cross sections are unknown, the conversion cannot be directly calculated from the raw signals of DBT and BiPhe, which is why the following conversion expression is introduced

$$X = \frac{xA_{BiPhe}}{xA_{BiPhe} + A_{DBT}} \tag{6.1}$$

where X is conversion, x is a sensitivity factor, and A_{BiPhe} and A_{DBT} are the integrated peak areas of BiPhe and DBT, respectively. As is obvious from equation 6.1 the sensitivity factor is at this point an unknown quantity.

The first step in the derivation of x is an estimation of the DBT signal calculated from its vapor pressure. In order to make this estimation, a simplified version of the Antoine equation is applied [101, 133, 134]

$$log(P) = B - C/T \tag{6.2}$$

where P is the vapor pressure, T is the temperature, and B and C are the compound-specific constants, $B = 21.1$ and $C = 8353$. Combining the calculated DBT vapor pressure, P_{DBT}, found by equation 6.2 with the measured TOF-MS signal, $DBT_{measured}$, at a given time where no BiPhe is formed, a conversion factor, k, can be estimated from the following equation, taking the flow ratios into account

$$k = \frac{P_{DBT}}{DBT_{measured}} \cdot \left(\frac{F_{DBT}}{F_{total}} \right) \tag{6.3}$$

Here, F_{DBT} is the DBT flow entering the µ-reactor and F_{total} is the total flow entering the µ-reactor. The factor, k, is specific to each experiment, since a drift in the lenses, thus TOF-MS signal, can change the relative peak intensities. However, it will only be used in this connection.

The TOF-MS signal $DBT_{calculated}$ can now be predicted using k and P_{DBT}

$$DBT_{calculated}(t) = \frac{P_{DBT}(t)}{k} \cdot \left(\frac{F_{DBT}}{F_{total}} \right) \tag{6.4}$$

where $P_{DBT}(t)$ is obviously dependent on the temperature of the DBT source at time, t.

The result of this estimation can be seen from Figure 6.5, where the dashed greenish-blue line indicates the calculated DBT signal, $DBT_{calculated}$, based on the measured DBT source temperature (dashed red line). This signal represents the amount of DBT that can be converted by the catalyst.

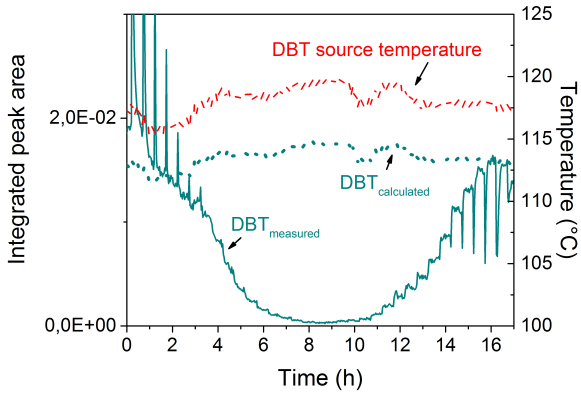

Figure 6.5: *Left y-axis shows the integrated peak area of $DBT_{measured}$ and the corresponding $DBT_{calculated}$ as a function of DBT source temperature on the right y-axis (MR-02). The obvious undershoot during the first two hours can be explained by degassing from the catalyst surface, thus cannot be accounted for by the DBT source temperature.*

Due to mass conservation, the sum of the reactants and products should be constant. Since one DBT molecule is converted into one BiPhe molecule and no other products are formed (the H_2S signal is not included here in order to find the sensitivity factor relating DBT and BiPhe specifically), the sum, A_{sum}, hence the BiPhe signal, would ideally reach the level of $DBT_{calculated}$ at full conversion. As was seen in Figure 6.4b the decrease in DBT signal did not correspond to the increase in the BiPhe signal, and in order to fulfill this requirement equation 6.5 was defined

$$A_{sum} \approx A_{DBT} + x \cdot A_{BiPhe} \tag{6.5}$$

With these assumptions it was found that BiPhe and DBT are related by a sensitivity factor of $x = 1.3$.

The resulting corrected BiPhe signal can be seen in Figure 6.6 labelled $xBiPhe$, and from this point on, $x = 1.3$ will be applied in all following data evaluation.

As can be seen in Figure 6.6 the sum of $DBT_{measured}$ and $xBiPhe$ is not completely constant but does, however, reach the same level as $DBT_{calculated}$, which shows that this is a reasonable approach, even though not perfect. This

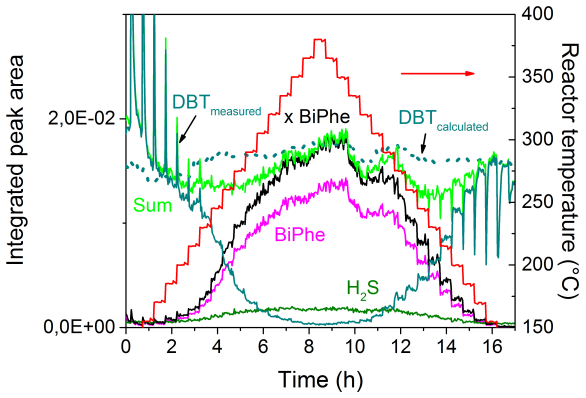

Figure 6.6: *The left y-axis shows the integrated peak areas of DBT, BiPhe and H_2S. The red curve shows the temperature ramp and is read at the right y-axis. Based on the calculated DBT signal, $DBT_{calculated}$, the sensitivity factor, $x = 1.3$ was derived, resulting in the black line ($xBiPhe$).*

was also evident for the remaining samples where the sum did not reach the same level as the $DBT_{calculated}$, and the DBT signal decreased more than the BiPhe signal increased. Since no other products were observed, the most obvious cause is deposition of DBT in the tubing, due to insufficient heating. This approach was, however, still applied in order to compare and interpret the results with respect to conversion.

In Figure 6.7 the conversion calculated from equation 6.1 can be seen for the four Pt nanoparticle samples. The included data points are calculated as the mean value of the conversion of all spectra obtained at the corresponding temperature step on the upward ramp, together with the standard deviations as error bars.

As can be seen from Figure 6.7 the relative conversion of the four Pt samples follow the same trend, though at the highest temperature, the two 6 nm samples are the most and the least active samples, respectively. Comparing the samples in a region of less than 50 % conversion, no obvious size effect can be observed, but conversion was obtained and the setup had been proved applicable for gas phase HDS of DBT. In the next step we therefore approached a drastically different scenario.

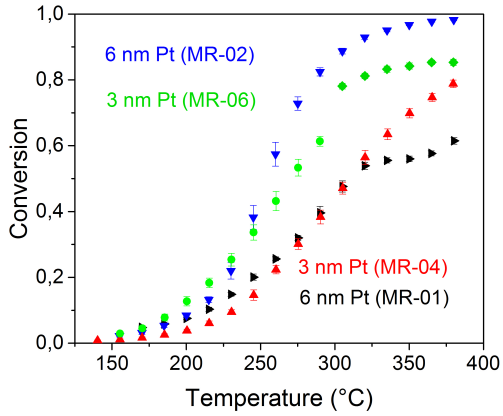

Figure 6.7: *Relative conversion of DBT on 3 nm Pt and 6 nm Pt samples. Black: 6 nm Pt (MR-01), blue: 6 nm Pt (MR-02), red: 3 nm Pt (MR-04) and green: 3 nm Pt (MR-06).*

6.3 Pt single atoms

The steric hindrance in 4,6-DMDBT as opposed to DBT encouraged us to go to more extreme situations. We wanted to test Pt nanoclusters consisting of only few atoms, but since the deposition current was too low, we ended up testing samples of Pt single atoms instead, since these were more easily prepared within the technical capabilities of the cluster source. Again, my colleague Anders Bodin provided the samples and also performed the sample characterization. Two µ-reactors were prepared and additionally scanning TEM (STEM) images were obtained.

Table 6.2: *Overview of Pt single atom samples*

Sample (ID)	Size (nm)	Mass (amu/ particle)	Number of atoms (sample)
AnluMR-12	single atoms	195	$6.49 \cdot 10^{13}$
AnluMR-13	single atoms	195	$6.49 \cdot 10^{13}$

The white spots in Figure 6.8 show Pt single atoms deposited onto lacy carbon

covered Cu grids with small areas of graphene. Mostly well-distributed Pt single atoms can be observed, but a fraction of the atoms seems to have agglomerated into clusters of various sizes.

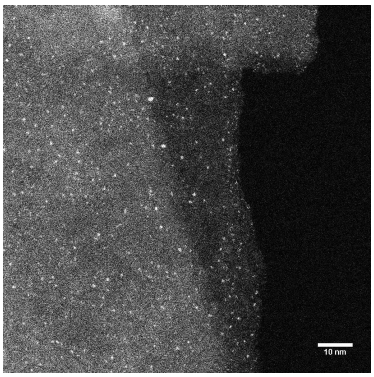

Figure 6.8: *STEM image of Pt single atoms deposited onto lacey carbon covered Cu grids with small areas of graphene. Image by Anders Bodin.*

Both samples were tested in the HDS of DBT and the sensitivity factor derived in the previous section was included in the data interpretation. Examples of the obtained spectra can be found in Appendix A, and the activity plots can be seen from Figure 6.9.

During these measurements we struggled with very low overall signal intensities and small amounts of BiPhe were observed. Due to limited amount of time, the temperature of the sample seen from Figure 6.9b was ramped up more harshly to rule out if an increase in temperature could at all induce any activity.

Comparing the two samples in terms of the previously defined conversion, some variations are again observed above 250 °C in Figure 6.10. It is unclear why two identically prepared samples vary this much, but at the time of the experiments the extreme drifts in the voltage supply driving the internal lenses in the TOF-MS had not been established, and it might definitely have had an effect.

Additionally, it should be mentioned that all samples were sputter cleaned with Ar^+ ions for 45 minutes prior to deposition. This might have introduced a roughness in the bottom of the reaction chamber, which could effect the relative accessibility of the Pt, especially pronounced for single atoms.

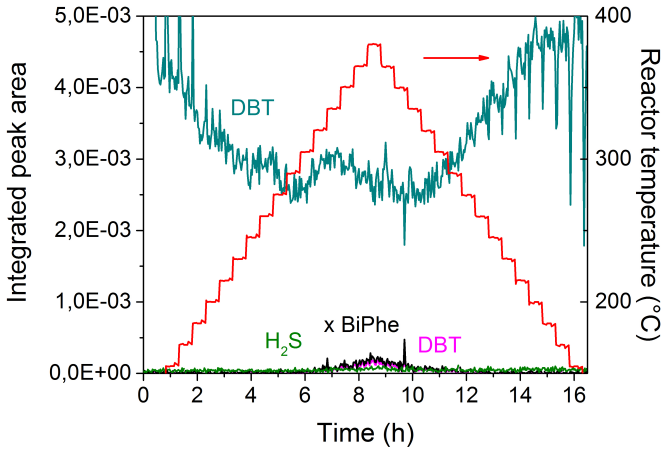

(a) HDS of DBT on Pt single atoms (AnluMR-12).

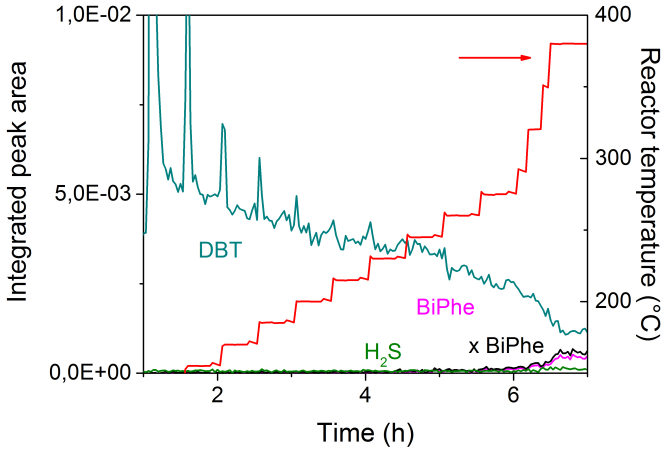

(b) HDS of DBT on Pt single atoms (AnluMR-13).

Figure 6.9: *HDS of DBT on Pt single atoms. The left y-axis shows the integrated peak areas of DBT, BiPhe and H_2S. The red curve shows the temperature ramp and is read at the right y-axis.*

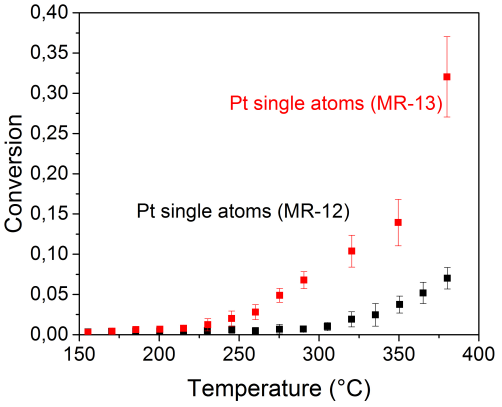

Figure 6.10: *Relative conversion of DBT on Pt single atoms. Black: AnluMR-12 and red: AnluMR-13.*

6.3.1 Estimating the intrinsic activity

Despite the fact that no clear trends could be observed for the Pt nanoparticles or the Pt single atoms, we wanted to make a comparison of all six samples. Therefore, mass activity and turnover frequency were calculated at 245 °C (on the upward temperature ramp), based on information from Table 6.1 and 6.3.

Table 6.3: *Number of surface atoms for all Pt samples. The number of surface atoms per Pt nanoparticle sample was based on Wulff constructed faceted Pt(111).*

	No. of surface atoms/particle	No. of surface atoms/sample
Single atoms	1	$6.49 \cdot 10^{13}$
3 nm	378	$3.41 \cdot 10^{14}$
6 nm	1722	$3.84 \cdot 10^{14}$

The number of surface atoms in the ~3 nm (185 kamu) and ~6 nm (1500 kamu) samples were based on Wulff constructions assuming (111) surface atom density. The number of active sites used in the calculation of the turnover frequencies was derived from the assumption that every surface atom constitutes an active site.

The calculated Wulff constructions were performed by my colleague Søren Berthelsen Scott and the results can be seen from Figure 6.11.

In order to estimate mass activity and turnover frequency, the reaction rate, r, were calculated according to equation 6.6.

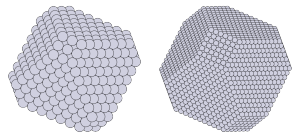

(a) 3 nm Pt. *(b) 6 nm Pt.*

Figure 6.11: *Wulff constructed 3 nm and 6 nm particles of Pt(111) surface density. Image by Søren Scott.*

$$r = \frac{F_{capillary}}{P_{Reactor}} \bar{P}_{DBT} \left(\frac{F_{DBT}}{F_{Total}} \right) X \tag{6.6}$$

where $F_{capillary}$ is the flow through the capillary, $P_{reactor}$ is the total reactor pressure and $\bar{P}_{DBT}$ is the mean vapor pressure of DBT, calculated over the values obtained over the entire temperature step. The results can be seen from Figure 6.12.

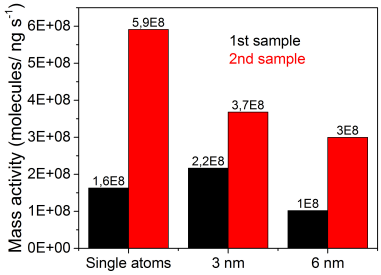

(a) Mass activity of Pt samples tested in the HDS of DBT.

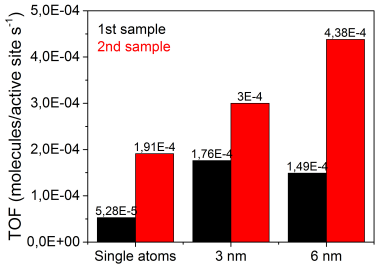

(b) Turnover frequency of Pt samples tested in the HDS of DBT.

Figure 6.12: *Mass activity and turnover frequency of the Pt samples tested in the HDS of DBT at 245° C.*

From a technical point of view, the mass activity is an interesting parameter, since economical considerations would probably rely on this. However, as is obvious from Figure 6.12, the variations between samples which in principle are pairwise identical are very significant, and since only two samples of each size were tested, statistically based analyses are not an option. However, in order to

make a reasonable comparison, the operating conditions should have been the same for all samples. Due to the unstable DBT source temperature it might be argued that this temperature, thus amount of DBT, is the reason for the variations observed. In order to evaluate this explanation, data from Figure 6.12 is normalized to the respective vapor pressures calculated from equation 6.2 - see Figure 6.13.

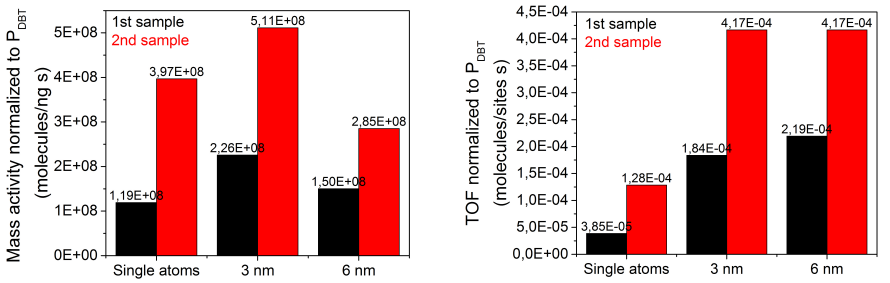

(a) Mass activity normalized to P_{DBT}. *(b) Turnover frequency normalized to P_{DBT}.*

Figure 6.13: *Activities at 245 °C normalized to P_{DBT}.*

As can be seen from Figure 6.13 the trend is still ambiguous, and the results can therefore not only be explained by the varying DBT vapor pressure.

Another explanation can be a variation in the reaction temperatures, because of the uncertainties in mounting and insulating the thermocouple at the exact same spot. If data is presented in the form of Arrhenius plots [3], the temperature dependence of the reaction rate is illustrated. Figures 6.14 and 6.15 show Arrhenius plots for the Pt nanoparticle samples, and as is evident, the activation energies are very similar, except from one 3 nm sample (MR-04), which has a slightly lower activation energy.

In order to estimate the temperature difference that would have resulted in the different turnover frequencies observed for the 6 nm samples, equation 6.7 is applied

$$r = \kappa \cdot e^{-\frac{E_a}{k_B T}} \Rightarrow \kappa = r \cdot e^{\frac{E_a}{k_B T}} \tag{6.7}$$

where κ is a pre-exponential factor and E_a is the activation energy.

Assuming that κ is identical for these two samples, equation 6.7 can be written for both by insertion of the turnover frequencies from Figure 6.12a (as the

rate) along with the calculated activation energies seen in Figure 6.14 and 6.15. This allows us to estimate the relative temperature difference which could have resulted in the different turnover frequencies.

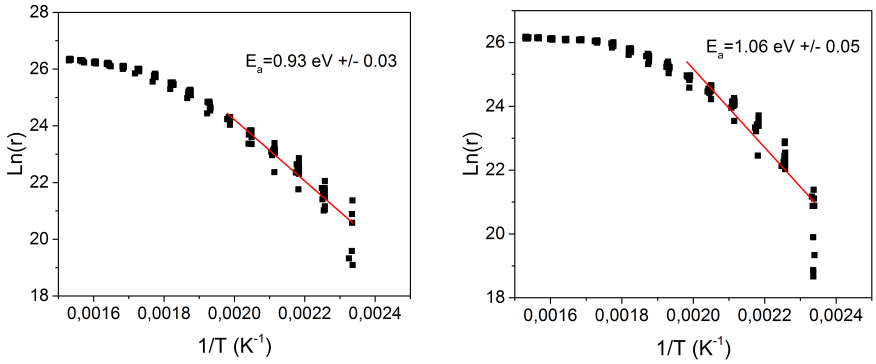

(a) 3 nm Pt (MR-04) *(b) 3 nm Pt (MR-06)*

Figure 6.14: *Arrhenius plots of the two 3nm (185kamu) samples and the corresponding activation energies with standard deviation.*

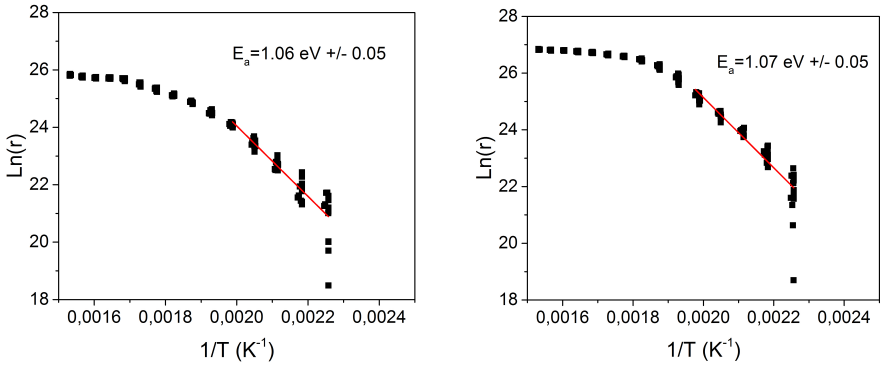

(a) *6 nm Pt (MR-01)* **(b)** *6 nm Pt (MR-02)*

Figure 6.15: *Arrhenius plots of the two 6 nm (1500 kamu) samples and the corresponding activation energies with standard deviation..*

The calculation results in a temperature difference of 30 °C. At this point it should again be mentioned that the temperature in the reaction chamber was controlled by a thermocouple mounted on top of the Pyrex lid. If this thermocouple was not directly in contact with the lid, insufficiently insulated or mounted in a different position from time to time, the actual temperature in the reaction chamber might have been very different from the one measured

However, an alternative explanation could be the deposition. If the size of particles deposited in what was assumed to be similar samples varies significantly from each other, the number of active sites will vary accordingly, and this could explain the different activities observed.

6.4 HDS of 4,6-DMDBT

As previously mentioned, the current setup configuration was designed to enable back-to-back HDS of DBT and 4,6-DMDBT. Due to the lack of information regarding 4,6-DMDBT with respect to vapor pressure and ionization cross section, the same mass activity and turnover frequency could not be calculated, and the results are therefore qualitatively evaluated.

Due to time constraints and technical difficulties, only the four Pt nanoparticle samples were tested with this approach. Because of the lack of intensities experienced when dosing DBT in both Pt single atom samples, we did not attempt to test them with 4,6-DMDBT.

The same procedure was followed. Spectra were examined and an overview of the peaks observed at three different temperature steps can be seen in Figure 6.16.

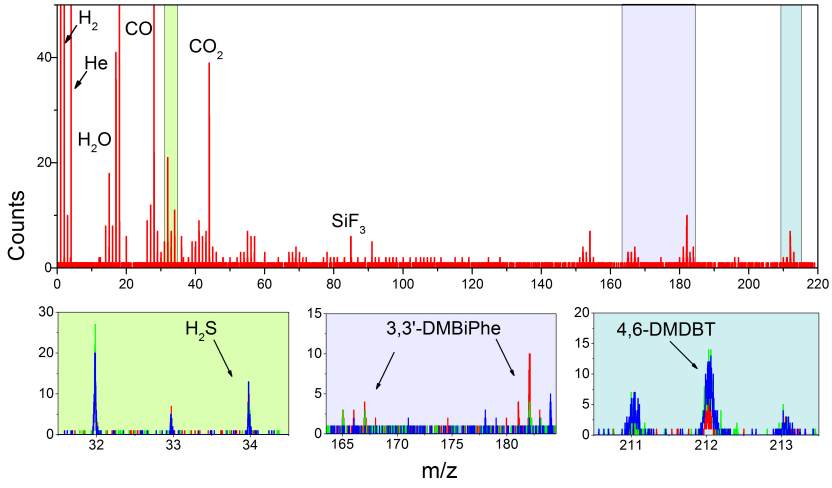

Figure 6.16: *TOF mass spectrum of the HDS of 4,6-DMDBT on a 3 nm Pt sample (MR-02). The red and uppermost spectrum was obtained at 350° C and shows masses from* m/z = *0 to* m/z = *220. The insets below illustrate close-ups of three regions. Red spectrum: 350° C; green spectrum: 275° C; and blue spectrum: 200° C.*

In general, the peak intensities are quite low. The obvious reason is the lim-

itation in heating the containment volume, which also puts an upper limit to the temperature of the 4,6-DMDBT source. This means that limited amounts of 4,6-DMDBT is available for the HDS reaction. Furthermore, the ionization cross sections are also not known for 4,6-DMDBT and its respective potential HDS products, which might also effect the relative peak intensities. In addition to this, the compound specific constants necessary for the Antoine equation (eq.6.2) are unknown too, and a sensitivity factor could therefore not be derived for 3,3'-DMBiPhe.

In the low mass range, the same compounds appear as seen from Figure 6.2. The peaks observed in the mass range $m/z = 50$-80 do, however, seem more distinct than in Figure 6.2. These are attributed to fragments of various carbon species that were also present during the HDS of DBT, but since the remaining peaks are not very intense, and the y-axis narrower they seem more distinct in Figure 6.16.

The most prominent peak appears at $m/z = 182$, and belongs to the fragmentation of 3,3'-DMBiPhe as do the peaks observed at $m/z = 165$ and 167. These can be seen from the middle inset, where it is also evident that the number of counts is very low. The peak at $m/z = 154$ belongs to BiPhe, which is not a product of this reaction, but can either be a remainder from the HDS of DBT performed immediately before, or conversion of traces of DBT introduced from the inlet side of the reator.

Since 3,3'-DMBiPhe is the only product observed, this will be included in the plot showing the reaction progress. The same sensitivity factor was applied in the data interpretation, hence assuming the same relation between 4,6-DMDBT and 3,3'-DMBiPhe as for DBT and BiPhe. This might of course change the relative activities, if the derived value of $x = 1.3$ is too far from the ratio between the actual ionization cross sections.

The results can be seen from Figure 6.17 and 6.18.

It is clear that the trend of degassing from the catalyst occurs in a similar way for 4,6-DMDBT as was seen with DBT. Besides from that, some unfortunate effects of the fluctuating 4,6-DMDBT source temperature can be observed, especially for the samples shown in Figure 6.17a and 6.17b, where the 4,6-DMDBT signal decreases over the entire reaction period.

From Figure 6.18a the initial 4,6-DMDBT signal is a factor of ten higher than the initial signal in Figure 6.18b. However, the formation of 3,3'-DMBiPhe seems unaffected by the initial 4,6-DMDBT signal indicating that the active sites might have been blocked or that the 4,6-DMDBT is simply degassing from other spots in the system.

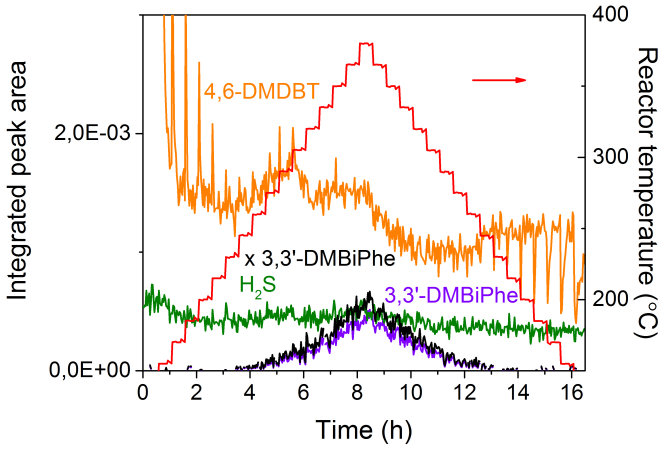

(a) HDS of 4,6-DMDBT on 3 nm Pt (MR-04).

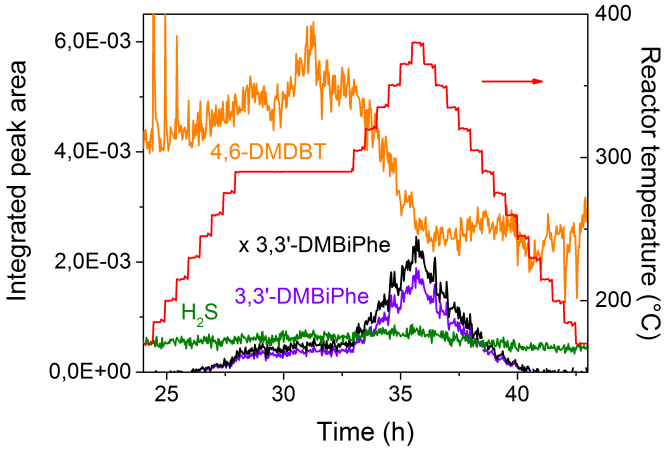

(b) HDS of 4,6-DMDBT on 3 nm Pt (MR-06).

Figure 6.17: *HDS of 4,6-DMDBT on 3 nm Pt samples. The left y-axis shows the integrated peak areas of 4,6-DMDBT, 3,3'-DMBiPhe and H_2S. The red curve shows the temperature ramp and is read at the right y-axis.*

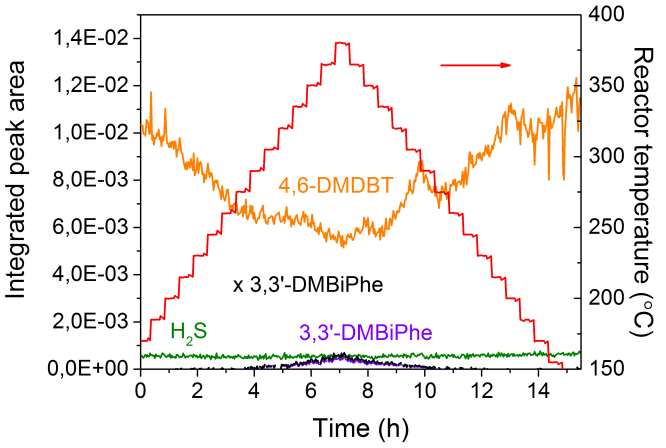

(a) HDS of 4,6-DMDBT on 6 nm Pt (MR-01).

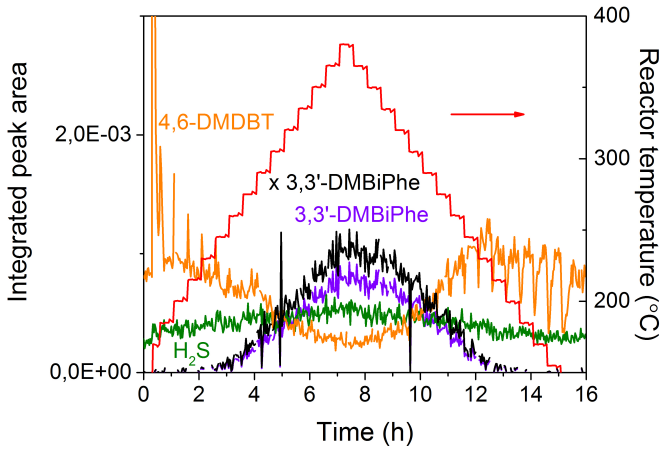

(b) HDS of 4,6-DMDBT on 6 nm Pt (MR-02).

Figure 6.18: *HDS of 4,6-DMDBT on 6 nm Pt samples. The left y-axis shows the integrated peak areas of 4,6-DMDBT, 3,3'-DMBiPhe and H_2S. The red curve shows the temperature ramp and is read at the right y-axis.*

The relative conversion was calculated for each sample and can be seen from Figure 6.19. Here, it is evident that the HDS of 4,6-DMDBT follows the exact same trend as was observed for the same samples in the HDS of DBT.

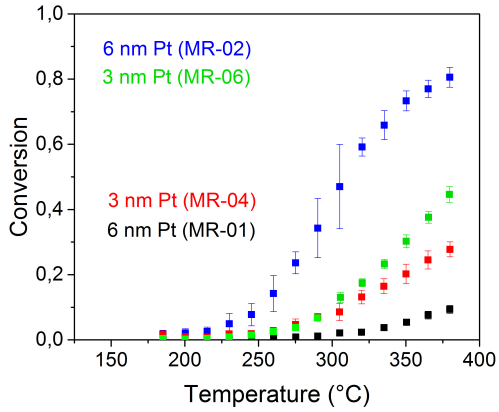

Figure 6.19: *Relative conversion of 4,6-DMDBT on 3 nm Pt and 6 nm Pt samples. Black: 6 nm Pt (MR-01), blue: 6 nm Pt (MR-02), red: 3 nm Pt (MR-04) and green: 3 nm Pt (MR-06).*

Since these four samples were the only samples which I managed to test in the HDS of 4,6-DMDBT on this setup, this part of the study will be left here. A lot of practical work still needs to be done and especially the heating of the containment volume which limits the temperature of the 4,6-DMDBT source could be improved.

6.5 Conclusion

In general it is difficult to draw unambiguous conclusions or make statistics based on only few samples. Furthermore, if the samples assumed to be idential in reality were far from, it only makes the results more unclear.

If the, in theory, identical Pt samples were significantly different with respect to the number of particles deposited, hence the number of active sites, the activity difference observed in these experiments are not surprising. However, the reaction temperature also has an important effect on the reaction rate, and

an increase of 30 °C could account for the differences observed in the turnover frequencies.

The Pt single atom samples were presumably affected by a drift in the TOF-MS lenses. These would have been interesting to test in the HDS of 4,6-DMDBT as well.

No direct size effects were observed during these experiments, due to the inconsistent results. One trend was, however, consistent, which was the trend of all Pt samples - nanoparticles and single atoms - to favor the DDS pathway under the applied reaction conditions.

What is also worth noticing and maybe most importantly of all, is that we enabled gas phase HDS of the solid compounds DBT and 4,6-DMDBT at ambient pressure which was a success in itself. Preparing for running these experiments addressed a lot of technical issues which we could benefit from before the following experiments.

Chapter 7

NiMo based mass-selected nanoparticles

The core of the HYDECAT project was to improve the already existing MoS_2 based HDS catalyst. The most promising way to do so is by creating well-defined model systems of different sizes and shapes and perform controlled catalytic activity measurements [135]. We therefore decided to test NiMo-based nanoparticles in the HDS of DBT and again Anders Bodin did a great job preparing every sample presented in this chapter, as well as the X-ray photoelectron spectroscopy (XPS) analyses. Characterization by TEM and scanning TEM (STEM) was performed by Anders Bodin and Christian Fink Elkjær, and some of the impressive images obtained can also be found in this chapter.

To correlate the HDS activity with specific structures, samples of different sizes and metal loadings were prepared. An overview of the samples is presented in Table 7.1.

Both metallic samples (MR-10 and MR-11) and in-flight sulfided samples (MR-05 and MR-12) were prepared for testing. For the last mentioned, H_2S was introduced in front of the sputter target inside the aggregation zone (as shown in Figure 3.3), and Anders spent a substantial amount of time optimizing the synthesis conditions. I therefore refer to his PhD thesis for more details. Common to all samples was the bimetallic sputter target of 75 atomic % Mo and 25 atomic % Ni from which they were synthesized, and the designation *NiMo* does therefore not correspond to the stoichiometric ratio, but will be applied for the

Table 7.1: *Overview of mass selected NiMo based samples*

Sample (ID)	Size (nm)	Mass (kamu/ particle)	Mass (ng metal/sample)	No. particles (sample)
MR-10	3.5	134	72	$3.24 \cdot 10^{11}$
MR-11	3.5	134	72	$3.24 \cdot 10^{11}$
MR-05	5	200	375	$1.13 \cdot 10^{12}$
MR-12	6.5	440	75	$1.03 \cdot 10^{11}$

samples in this chapter.

7.1 Sample characterization

As a standard procedure XPS was measured after each deposition. A detailed description of the XPS peak fitting and experimental procedure will not be provided here, however, the main features will shortly be reviewed.

In Figure 7.1 XPS spectra of metallic NiMo and in-flight sulfided $NiMoS_x$ are compared with a MoS_2 single crystal as reference.

As can be seen the Mo3d peaks shift towards higher binding energies from metallic at 227.5 eV to 228.2 eV in the in-flight sulfided sample and 228.8 eV in the reference MoS_2 single crystal. The intermediate binding energy of the in-flight sulfided sample and the assymetric peak shape suggest that the particles have not been fully sulfided, which is also confirmed by the quantification. This also means that several oxidation states might be present in the sample from metallic Mo(0) to sulfided Mo(IV).

Metallic NiMo nanoparticles were imaged by STEM in high-angle annular dark-field (HAADF) mode, and the particles therefore appear light on a dark background. Figure 7.2 shows the STEM images of a metallic NiMo (134 kamu) sample and an in-flight sulfided (200 kamu) sample. The metallic sample features small spherical particles of a very narrow size distribution, whereas the in-flight sulfided sample has particles of a very different morphology, explaining the wide size distribution. The same amount of metal was deposited on both grids and therefore not reflecting the loading of the ones tested.

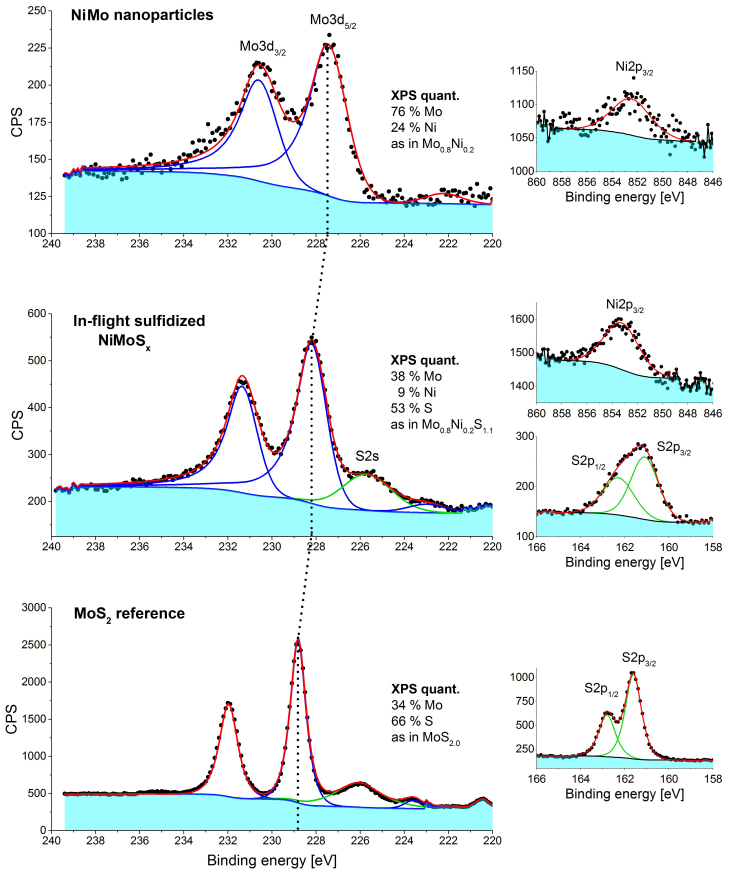

Figure 7.1: *XPS spectra of metallic NiMo nanoparticles, in-flight sulfided nanoparticles and a MoS_2 single crystal as a reference. The Mo3d peaks shift towards higher binding energies upon sulfidation, and the intermediate binding energy of $NiMoS_x$ indicates that the sample has not been fully sulfided, which is evident from the quantification as well. The more narrow peaks in MoS_2 can be explained by a higher ordered crystal structure. Image by Anders Bodin.*

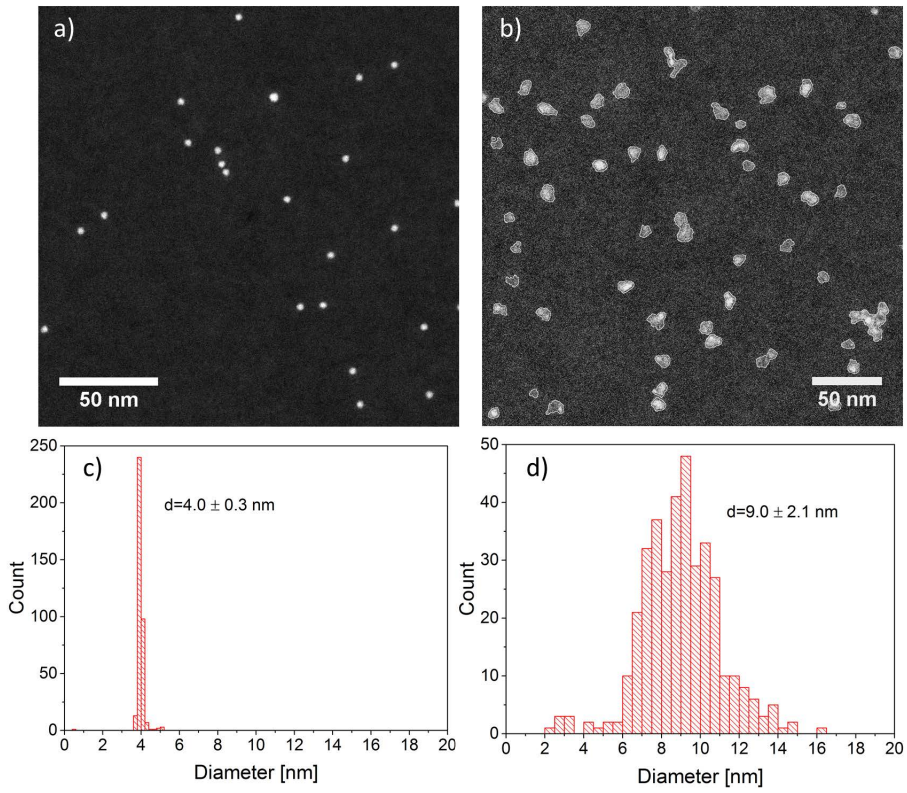

Figure 7.2: *a) STEM image of metallic NiMo nanoparticles of 134 kamu deposited on a SiO_2 TEM grid. b) In-flight sulfided $NiMoS_x$ nanoparticles of 200 kamu deposited on a SiO_2 TEM grid. The same amount of metal was deposited in both grids. c) Size distribution of the metallic nanoparticles. d) Size distribution of the in-flight sulfided $NiMoS_x$ nanoparticles.*

From the deposition until the µ-reactor experiments were performed, exposing the samples to air was unevitable. The structure and composition derived from Figure 7.1 and 7.2 was therefore most likely not completely reflecting the state of the sample once it was mounted in the µ-reactor platform and ready for catalytic activity measurements. Additional XPS spectra were therefore measured after exposing the samples to air for an hour, and in this way get a better understanding of the effect. The result can be seen in Figure 7.3.

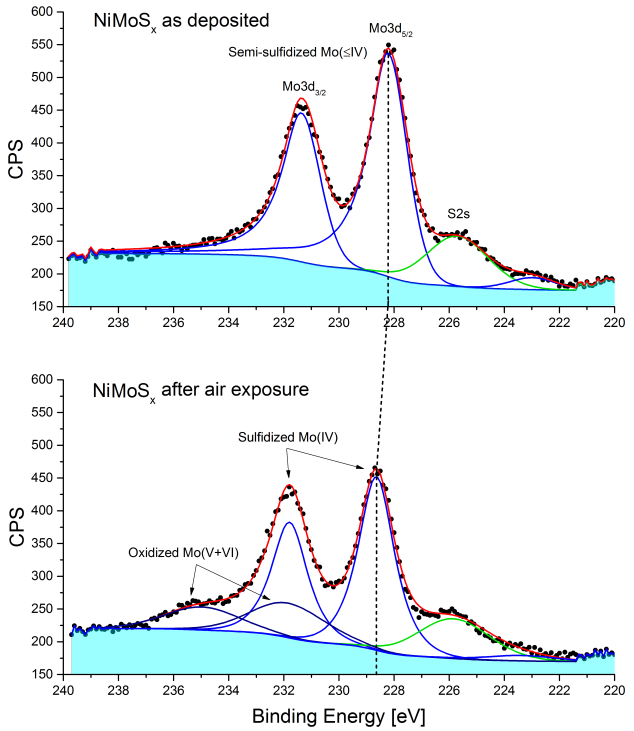

Figure 7.3: *XPS spectra of the Mo3d and S2s regions showing an additional set of Mo3d peaks, corresponding to the oxidized Mo(V+VI). Image by Anders Bodin.*

As can be observed from Figure 7.3, air exposure affects the sample, which has also earlier been reported [74, 136], though the change was not dramatically. A shoulder appears on the high binding energy side of the $Mo3d_{3/2}$ peak and at the same time, the $Mo3d_{5/2}$ peak is shifted towards slightly higher binding energies by 0.4 eV. The observed changes can be explained by oxidation of the unsaturated bonds in the Mo atoms. This results in a mixture of oxidized and sulfided Mo with oxidation states IV, V and VI. After air exposure the majority of the particle remains sulfided with 73 % of the Mo in the Mo(IV) state and 27 % in Mo(V+VI) states.

Looking more detailed at the in-flight sulfided sample (Figure 7.4), it is obvious that different particle shapes are present, however, with a tendency to form platelet-like structures.

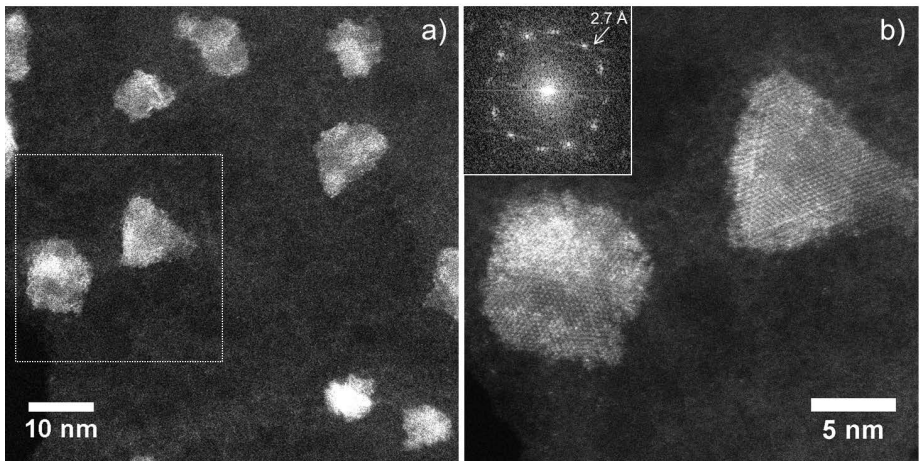

Figure 7.4: *a) $NiMoS_x$ nanoparticles of 200 kamu deposited on a graphene substrate. The particles in the dashed square can be seen in b) a high-magnification image which reveals a hexagonal structure of the basal plane. Image by Anders Bodin.*

The dashed square in Figure 7.4a is shown in a high-magnification image in Figure 7.4b, where the individual atomic columns are visible. Fourier transform (inset) reveals a hexagonal lattice with a periodicity of 2.7 Å, corresponding to the $MoS_2(100)$ [82]. The triangular shaped particle in Figure 7.4b is somewhat similar to the structure of an unpromoted MoS_2 nanoparticle as described in chapter 2, but was not representative to the majority of the particles. However, the particles in Figure 7.4 were not annealed and these are therefore not their

equilibrium structures.

Anders and Christian also obtained EDX spectra of the 200 kamu sample, and I once again refer to Anders' thesis for more details. The result showed that Ni was homogeneously distributed in the particles, and only present together with Mo, thus no indication of a separate NiS_x phase.

A similar approach was used in the synthesis of 440 kamu nanoparticles (MR-12) as for the 200 kamu sample, and the structural composition is therefore assumed to be the same, though an actual quantification by XPS was not calculated. When the 440 kamu samples were imaged by STEM some very interesting features were observed.

As can be seen from Figure 7.5, most particles expose upright standing layers, and from the Fourier transform in the inset in Figure 7.5b the in-plane (100) distance and inter-plane (001) lattice distances expected for MoS_2 confirm this structure [137].

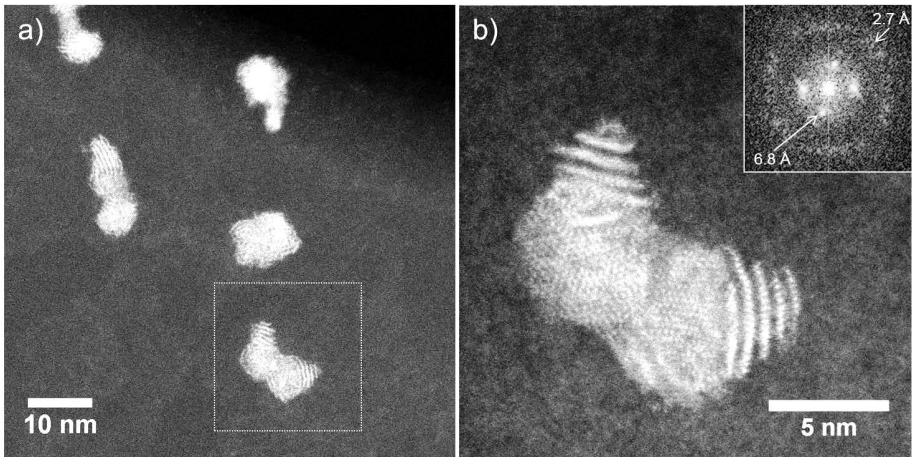

Figure 7.5: *a) $NiMoS_x$ nanoparticles of 440 kamu deposited on a graphene substrate. The dashed square shows b) a high-magnification image of a nanoparticle that exposes its basal planes orthogonal and perpendicular to the substrate. The Fourier transform confirms the in-plane (100) distance and the inter-plane (001) lattice distances expected for MoS_2 [137].*

According to the literature reviewed in chapter 2, HDS of DBT takes place on the brim of the nanoparticles with the coordinatively unsaturated sites and with the upright standing particles observed here, this might facilitate a higher

activity. Furthermore, the steric hindrance in 4,6-DMDBT could potentially be circumvented when the molecules can access the edges in a perpendicular mode.

7.2 HDS of DBT

All of the above mentioned samples were tested in the HDS of DBT. The experiments were conducted as previously described, however, the findings from XPS and STEM combined with previous studies [33, 70, 71] encouraged us to add an additional step to the experimental routine.

7.2.1 200 kamu $NiMoS_x$

Before presenting the results of the 200 kamu sample (MR-05), a few things should be mentioned.

At the time of testing this sample, the RTD discussed in chapter 3 was still used for temperature measurements. Therefore, the temperature was probably much higher in reality than what will appear in the included plots. However, for comparison, the reported temperature will still be used.

Since XPS revealed an impact on the sample composition after exposure to air, the influence on the activity was investigated as well. The sample was tested as-prepared and no products were observed (Figure B.1B.1). After a one hour sulfidation step at 350 °C in one bar of 10 % H_2S in H_2, simulating the industrial sulfidation process [33], the sample was tested again, showing the formation of BiPhe, again suggesting the DDS reaction pathway as observed with the Pt samples in chapter 6. An example of the resulting spectra can be seen from Figure 7.6.

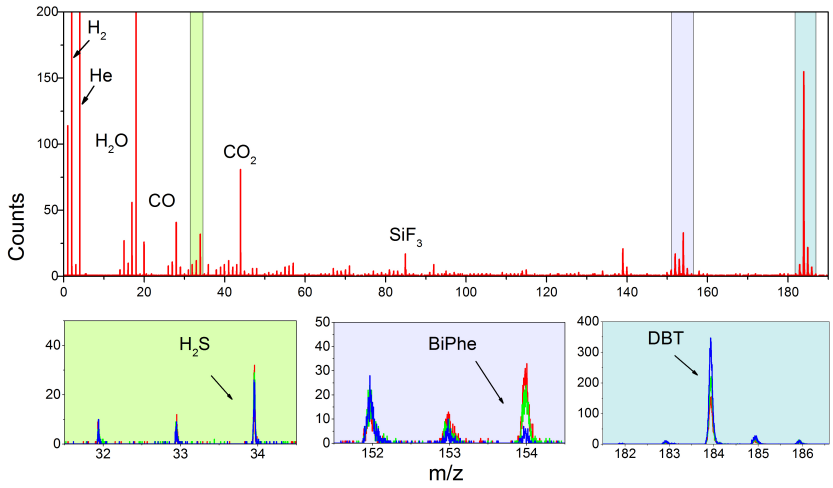

Figure 7.6: *TOF mass spectrum of the HDS of DBT on 200 kamu in-flight sulfided $NiMoS_x$ (MR-05) re-sulfided in the μ-reactor at 1 bar 10 % H_2S in H_2 at 350 °C for an hour. The red and uppermost spectrum was obtained at 300 °C and shows masses from* $\mathrm{m/z} = 0$ *to* $\mathrm{m/z} = 190$*. The insets below illustrate zooms of three regions. Red spectrum: 300 °C; green spectrum: 250° C; and blue spectrum: 200 °C*

In order to investigate the influence of the sulfidation step on the particle morphology, 200 kamu nanoparticles were deposited on SiO_2 TEM grids, simulating the substrate of the µ-reactor, and sulfided in a tube furnace under the exact same sulfiding conditions as in the µ-reactor.

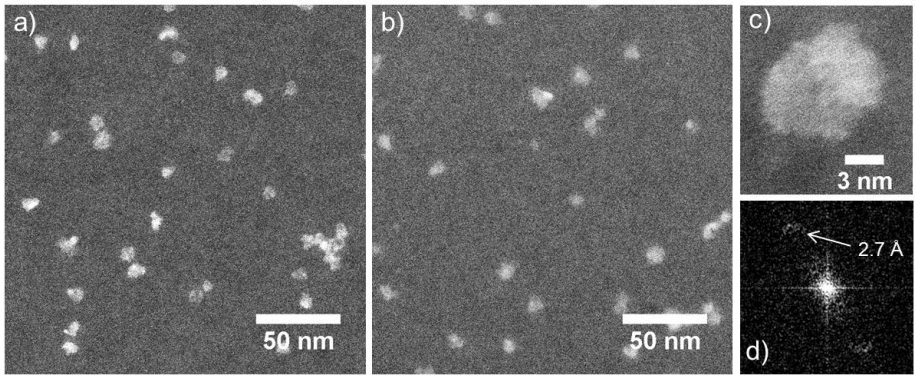

Figure 7.7: *The effect of re-sulfiding in-flight sulfided 200 kamu $NiMoS_x$. a) Shows the in-flight sulfided $NiMoS_x$ nanoparticles deposited on a SiO_2 TEM grid, b) shows particles from the same deposition after re-sulfidation in a tube furnace - the morphology is retained. c) High resolution image of one of the particles seen in b), displaying a MoS_2 (100) periodicity, which is also evidenced in the Fourier transform seen in d).*

The STEM images from Figure 7.7 indicate that the particles retain their shape during the sulfidation step, and the activity seen from Figure 7.8 indicates that surface oxides has been successfully re-sulfided.

As can be seen from Figure 7.8, plateaus of BiPhe is observed at every temperature step between 200-300 °C. However, a slight deactivation at 300 °C can be observed. Since full conversion is obviously not obtained, mass transport limitation is eliminated, but an explanation could be that the relatively high metal loading (375 ng) of flat lying particles simply had a shielding effect on each other, thus preventing access to all active surface sites.

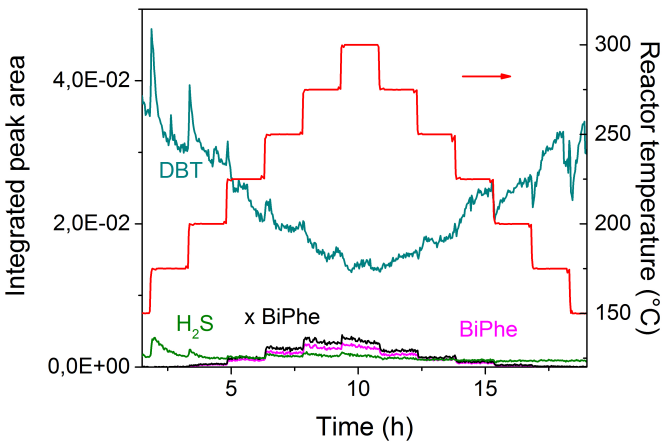

Figure 7.8: *HDS of DBT on 200 kamu in-flight sulfided $NiMoS_x$ nanoparticles (MR-05) re-sulfided in the μ-reactor at 1 bar 10 % H_2S in H_2 at 350 °C for an hour.*

For the sake of underlining the importance of the sulfidation step, an additional oxidation step was included, in order to deactivate the sample and compare the activities. The sample was deactivated for one hour in 400 mbar of air at 200 °C, before being tested and re-activated by the above mentioned sulfidation step again - activity plots can be seen in Appendix B, Figures B.2 and B.3. The relative conversions for the upward temperature ramp were calculated according to equation 6.1 and are plotted in Figure 7.9 with the standard deviations as error bars.

The oxidation step deactivated the sample as expected, but the activity was not entirely regained after the second sulfidation as seen from the black data points in Figure 7.9. This might be caused by segregation of Ni and Mo as the sulfide sample is oxidized. On the other hand, under industrial conditions, the regeneration of the catalyst only results in 70 % of the initial activity, and a slight deactivation is therefore not surprising.

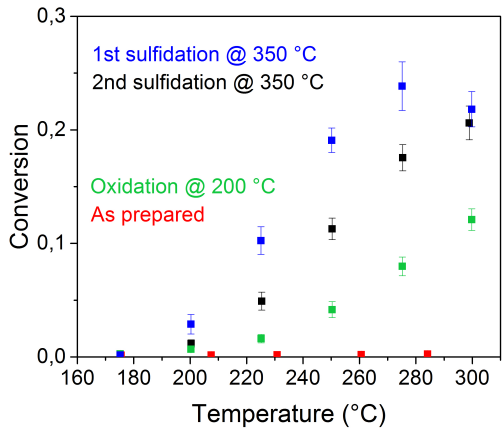

Figure 7.9: *Relative conversion of four different experiments on the 200 kamu in-flight sulfided $NiMoS_x$ sample (MR-05). Red: as-prepared, green: after a one hour oxidation at 400 mbar and 200° C, blue: after the first one hour re-sulfidation in 1 bar of 10 % H_2S in H_2 at 350 ° C in the μ-reactor, black: after the second one hour re-sulfidation in 1 bar of 10 % H_2S in H_2 at 350 ° C.*

7.2.2 Metallic NiMo

Having established the need for a sulfidation step prior to catalytic measurements in the µ-reactor, metallic NiMo nanoparticles were tested following the same procedure. When comparing these results with the ones obtained from re-sulfiding the in-flight sulfided sample (MR-05), it could be clarified if the morphology induced by the in-flight sulfidation during the synthesis procedure had an impact on the activity. Spectra and activity plots can be found in Appendices A and B.

Conversion of DBT on the samples MR-10 and MR-11 before and after the one hour sulfidation step can be seen in Figure 7.10.

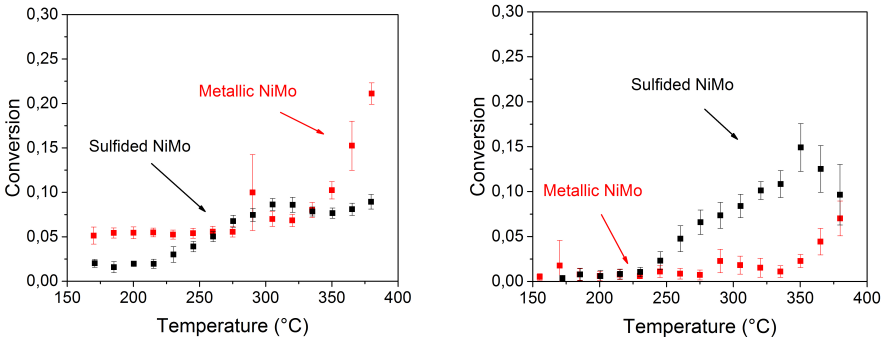

(a) *Conversion on 134 kamu NiMo (MR-10)* ***(b)*** *Conversion on 134 kamu NiMo (MR-11).*

Figure 7.10: *Conversion of as-prepared and sulfided 134 kamu NiMo samples (MR-10 and MR-11). Red: as-prepared metallic NiMo nanoparticles; black: after a one hour sulfidation in 1 bar of 10 % H_2S in H_2 at 350° C.*

Comparing Figure 7.10a and 7.10b it is obvious that the two samples show different trends. From Figure 7.10a it is clear that both activity runs - before and after sulfidation - show conversion even at the lowest temperatures. However, I suspect that the first run for the metallic NiMo (MR-10) was affected by a high background, potentially deposited at the stainless steel tubing. This is supported by the fact the the same sample shows a lower conversion at the lower temperatures after sulfidation. If this background is left out of account, the conversions alo correspond well with the, in theory, identical sample seen from Figure 7.10b.

Furthermore, sulfiding a metallic material might be more energy costly than sulfiding an oxide, since in the oxide structure the sulfur atoms would have to substitute the oxygen atoms, whereas in the pure metal, a completely new structure would have to be formed.

7.2.3 440 kamu $NiMoS_x$

Due to the interesting STEM images revealing upright standing layers of the 440 kamu $NiMoS_x$ sample, we were curious about the activity of this sample compared to the other NiMo-based samples. Again, the spectra can be found in Appendix A, and the activity of the as-prepared in-flight sulfided sample and the same sample after re-sulfidation in the µ-reactor can be seen in Figure 7.11.

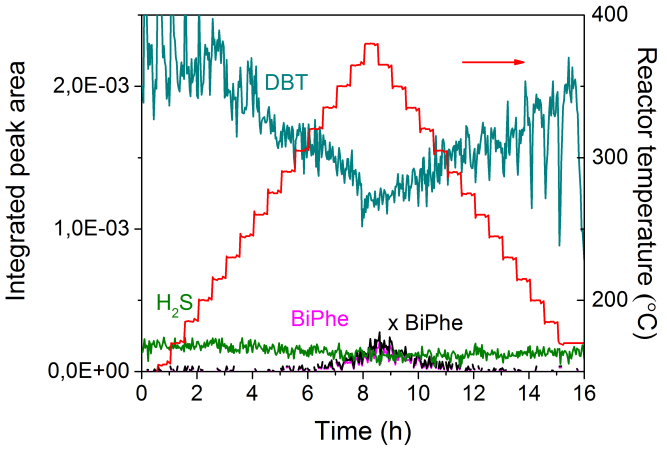

(a) HDS of DBT on 440 kamu in-flight sulfided $NiMoS_x$ (MR-12).

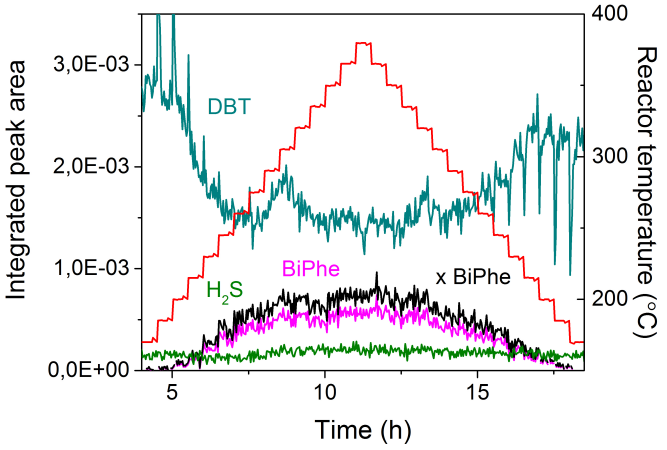

(b) HDS of DBT on 440 kamu in-flight sulfided $NiMoS_x$ (MR-12) re-sulfided in the µ-reactor for one hour at 350 °C in 1 bar of 10 % H_2S in H_2.

Figure 7.11: *Activity plots of HDS of DBT on in-flight sulfided 440 kamu $NiMoS_x$ (MR-12) as-prepared and after re-sulfidation in the µ-reactor.*

In this case, the sulfidation has a pronounced effect on the activity and the decrease in DBT signal corresponds well with the observed shape of the formed BiPhe. In order to compare this sample with the two metallic NiMo samples and the 200 kamu in-flight sulfided $NiMoS_x$ sample, the conversions were calculated and can be seen from Figure 7.12.

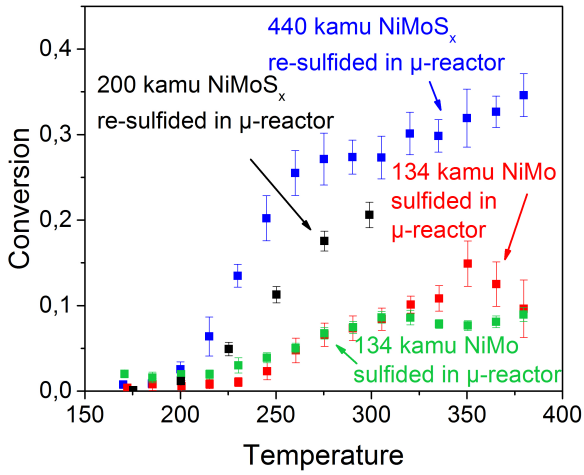

Figure 7.12: *The relative conversions of all Mo-based samples. Green: sulfided 134 kamu NiMo (MR-10), red: sulfided 134 kamu NiMo (MR-11), black: 200 kamu in-flight sulfided $NiMoS_x$ (MR-05) re-sulfided in the µ-reactor, blue 400 kamu in-flight sulfided $NiMoS_x$ (MR-12) re-sulfided in the µ-reactor.*

The relative conversions of all the NiMo-based samples illustrate the effect of the sulfidation step in the µ-reactor. However, since different amounts of metal were deposited in the µ-reactors (see Table 7.1) a more logical comparison is based on data normalized to the metal loading.

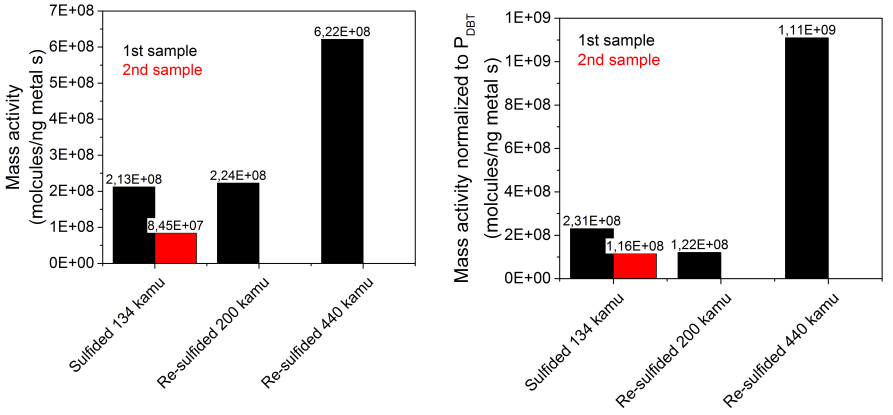

(a) *Mass activity normalized to metal content.* ***(b)*** *Mass activity normalized to* P_{DBT}.

Figure 7.13: *Mass activity at 245 °C of metallic 134 amu NiMo samples sulfided in the μ-reactor, in-flight 200 and 440 kamu* $NiMoS_x$ *re-sulfided in μ-reactor for one hour in 10 %* H_2S *in* H_2 *at 350 °C.*

The plot in Figure 7.13a shows the mass activity at 245 °C normalized to metal loading. As can easily be seen, the re-sulfided 400 kamu in-flight $NiMoS_x$ sample stands out with a threefold higher activity than both the sulfided metallic NiMo samples and the 200 kamu re-sulfided in-flight sulfided sample. However, as was observed with the Pt samples, the deviations in DBT signals might change the relative activities. Figure 7.13b therefore illustrates the effect of this normalization. However, this only makes the difference even more pronounced and the 400 kamu sample now exceeds the 200 kamu sample by an order of magnitude.

Again, the difference between the activities observed for the two identically prepared samples, MR-10 and MR-11, corresponds will with the results obtained in the HDS of DBT on Pt nanoparticles, where two similar samples also varied ~50 %.

The most obvious explanation to the high activity observed for the 440 kamu sample can be related to the findings from the STEM images showing primarily upright standing layers of $NiMoS_x$ nanoparticles. This was unfortunately the only sample of this configuration which was tested, but certainly suggests that this kind of nanoscale engineering offers highly interesting results in the HDS reaction.

7.3 Conclusion

The HDS of DBT on the NiMo-based sample showed conversion through the DDS pathway, hence resulting in BiPhe as the main product. Even though only few samples were tested, the results indicate that the 440 kamu sample has a higher mass activity than the three other samples. This is not surprising since DBT is known to adsorb on both sulfur vacancies next to the brim sites on the S-edges and on coordinatively undersaturated sites like corners and kinks. With the upright standing $NiMoS_x$ nanoparticles the density of these sites are most likely increased. However, one should keep in mind that the STEM images only show a small part of a sample similar to the one being tested, and if the actual sample has the exact same features is dificult to say. It is, however, the most obvious explanation for the increased activity observed in these experiments.

Even though the sulfidation procedure was reflecting the industrial sulfidation process, the test conditions with much lower operating pressure can have had an effect on the reaction pathways observed. Usually, the introduction of pressurized hydrogen creates sulfur vacancies, and these might therefore not have been present here to the same extent.

Finally, the different temperature measurements might also have had an effect. However, experience with deformation of the reactor lids as shown in Figure 3.6a indicates that the temperature reported by the RTD shows values that are too low. If this is the case, the difference between the 200 kamu and 440 kamu samples would be even more clear.

Chapter 8

Conclusion and outlook

The description of my share in the HYDECAT project was related to the synthesis and activity measurements of new catalysts for deep HDS. However, the task of optimizing and modifying the experimental setup was more time-consuming than expected. The number of activity measurements presented in this work is therefore not overwhelming, and more samples should of course be tested in order to draw final conclusions. However, I like to believe that the work presented in this thesis was a success, given the circumstances, and if others can benefit from this contribution, I am more than happy.

8.1 The experimental setup

The µ-reactor and the TOF-MS formed the basis for all the measurements presented in this thesis. A lot of time and effort were put into optimizing the already existing setup and with the final setup configuration it was demonstrated that this was successfully done. The specially designed flange with implemented ion source and internal heating increased the signal intensities so that activity measurements were enabled.

Measuring HDS activity of DBT and 4,6-DMDBT on different catalysts in a back-to-back mode ensured that the catalyst was not exposed to air in between the two measurements. However, this configuration also meant that it was difficult to avoid deposits of the compounds on the inner walls of the tubing, partially due to a stagnant gas volume in front of the closed source valve. The

extremely low vapor pressure of 4,6-DMDBT made it more difficult to handle than DBT, since physical limitations of the equipment were encountered when we tried to reach the melting point of 4,6-DMDBT at temperatures of more than 150 °C.

With respect to the heating of the compound sources, the unfortunate effect of the fluctuations in the grid voltage was discovered only recently. An easy fix is therefore to change to a DC power supply. But for future experiments, a new source design should also be considered. Since the current approach is to mount a thermocouple on the outside of the source, the actual temperature of the compound is only a rough approximation, and the uncertainty in the exact location between different measurements only makes this more pronounced.

At the same time, a temperature control should also be implemented, so that the heating of the source is not controlled by how much power is applied, but instead controlled by a temperature setpoint measured at the inside of the source. In the case of 4,6-DMDBT it might be advantageous to reconsider the use of a solvent to avoid clogging of the tubing.

When it comes to the RTD measurements and the reported temperature, which was much lower than measured with a thermocouple on top of the µ-reactor, it is an on-going process to identify the exact reason. It is of course essential to be able to control and measure the temperature during activity measurements, and if the problems encountered with the RTD are not fixed, an alternative arrangement of ensuring the same thermocouple location from time to time should instead be implemented.

With respect to the drifting lenses inside the TOF-MS, a new power supply can of course fix the problem. However, data logging should also be enabled so that a potential drift can be discovered between consecutive experiments, and an alarm given if a drift is detected.

8.2 Activity measurements

Despite the fact that the operating conditions were difficult to keep completely constant, the HDS of DBT and 4,6-DMDBT did demonstrate the technical advances of the setup, even though only few samples were tested, and reproducibility was a problem.

8.2.1 HDS on Pt samples

At 800 mbar and temperatures up to 380 °C the only products observed in the HDS of both DBT and 4,6-DMDBT were the DDS products, BiPhe and 3,3'-DMBiPhe, respectively. No HYD products were observed, but since the minimum H_2 pressure employed in industrial HDS is 20 bar, the low pressure employed in these experiments seems like a reasonable explanation. Keeping that in mind, it is therefore interesting that conversion of 4,6-DMDBT was obtained through the DDS pathway, since this is known to be the less active reaction pathway. However, both the DDS and the HYD pathways have been reported in the HDS of 4,6-DMDBT on Pt, and again the pressure must be a key factor.

Since most ionization cross sections were unknown, the sensitivity factor, x, relating DBT and BiPhe, was introduced in order to estimate the conversion. The 6 nm sample (MR-02) reached full conversion, and was therefore used in the derivation of x. However, no clear trends were observed, even though the mass activity and turnover frequency were normalized to the DBT vapor pressure. Again, the reaction temperature could be explain the large variations observed between two, in theory, identical samples.

8.2.2 HDS on NiMo-based samples

For the HDS on NiMo-based samples, the same trend was observed with respect to the reaction pathway, and again, only BiPhe was formed. A sulfidation step prior to the reaction increased the activity for all samples, but was most pronounced for the already in-flight sulfided $NiMoS_x$ samples. This was not surprising since XPS confirmed the formation of an oxide layer that needed to be resulfided after exposure to air, even though the particles retained their shape.

The 440 kamu in-flight sulfided $NiMoS_x$ nanoparticles imaged by STEM revealed upright standing particles. When these were resulfided in the µ-reactor and compared to the remaining samples after the same sulfidation step, an activity exceeding the others by an order of magnitude was observed. An explanation could be the morphology of upright standing particles, which expose more edge sites than the flat lying particles, hence more active sites. This therefore indicates that this type of sample is interesting to proceed with in the aim of enabling ultra deep HDS.

Bibliography

[1] Http://www.nobelprize.org/nobel_prizes/chemistry/laureates/1918/, "The Nobel Prize in Chemistry 1918," 1918.

[2] Http://www.nobelprize.org/nobel_prizes/chemistry/laureates/1931/, "The Nobel Prize in Chemistry 1931," 1931.

[3] J. Niemantsverdriet and I. Chorkendorff, *Concepts of Modern Catalysis and Kinetics*. 2003.

[4] V. Smil, "Detonator of the population explosion," *Nature*, vol. 400, p. 415, 1999.

[5] M. Boudart, B. H. Davis, and H. Heinemann, "Principles of Heterogeneous Catalysis," in *Handbook of Heterogeneous Catalysis*, pp. 1–48, 1997.

[6] J. Berzelius, "Quelques Idées sur une nouvelle Force agissant dans les Combinaisons des Corps Organiques," *Annales de chimie et de physique*, vol. 61, pp. 146–151, 1836.

[7] G. Ertl and H.-J. Freund, "Catalysis and Surface Science," *Physics Today*, vol. 52, no. 1, pp. 32–38, 1999.

[8] Http://goldbook.iupac.org/C00876.html, "IUPAC Compendium of Chemical Terminology, Electronic version."

[9] B. Hammer and J. Nørskov, "Theoretical Surface Science and Catalysis - Calculations and Concepts," in *Advances in Catalysis*, vol. 45, pp. 71–128, 2000.

[10] T. Pecoraro and R. Chianelli, "Hydrodesulfurization Catalysis by Transition Metal Sulfides," *Journal of Catalysis*, vol. 67, pp. 430–445, 1981.

[11] S. Harris and R. R. Chianelli, "Catalysis by Transition Metal Sulfides: The Relation between Calculated Electronic Trends and HDS Activity," *Journal of Catalysis*, vol. 86, pp. 400–412, 1984.

[12] R. R. Chianelli, G. Berhault, and B. Torres, "Unsupported transition metal sulfide catalysts: 100 years of science and application," *Catalysis Today*, vol. 147, no. 3-4, pp. 275–286, 2009.

[13] M. Turner, V. Golovko, O. Vaughan, P. Abdulkin, A. Berenguer-Murcia, M. Tikhov, B. Johnson, and R. Lambert, "Selective oxidation with dioxygen by gold nanoparticle catalysts derived from 55-atom clusters," *Nature*, vol. 454, pp. 981–983, 2008.

[14] H. Lee, S. E. Habas, S. Kweskin, D. Butcher, G. a. Somorjai, and P. Yang, "Morphological control of catalytically active platinum nanocrystals.," *Angewandte Chemie (International ed. in English)*, vol. 45, pp. 7824–7828, nov 2006.

[15] M. Andersson, F. Abild-Pedersen, I. Remediakis, T. Bligaard, G. Jones, J. Engbaek, O. Lytken, S. Horch, J. Nielsen, J. Sehested, J. Rostrup-Nielsen, J. Nørskov, and I. Chorkendorff, "Structure sensitivity of the methanation reaction: H 2 -induced CO dissociation on nickel surfaces," *Journal of Catalysis*, vol. 255, pp. 6–19, 2008.

[16] A. S. Crampton, M. Rötzer, C. Ridge, F. Schweinberger, U. Heiz, Y. Bokwon, and U. Landman, "Structure sensitivity in the nonscalable regime explored via catalysed ethylene hydrogenation on supported platinum nanoclusters," *Nature Communications*, vol. 7, p. 10389, 2016.

[17] J. V. Lauritsen, J. Kibsgaard, H. Topsøe, S. Helveg, B. S. Clausen, E. Laegsgaard, and F. Besenbacher, "Size-dependent structure of MoS2 nanocrystals.," *Nat. Nanotechnol.*, vol. 2, no. 1, p. 53, 2007.

[18] BP, "BP Energy Outlook 2017 edition," tech. rep., 2017.

[19] World Energy Council, "World Energy Resources 2013," tech. rep., World Energy Council, 2013.

[20] S. Srivastava and J. Hancsók, "Fuels from Crude Oil (Petroleum)," in *Fuels and Fuel-Additives*, pp. 48–120, 2014.

[21] E. Ortiz, "Air quality in Europe - 2015 report," Tech. Rep. 5, 2015.

[22] World Health Organization, "Ambient air pollution: A global assessment of exposure and burden of disease," tech. rep., World Health Organization, 2016.

[23] Http://eur-lex.europa.eu/, "Official Journal of the European Union," 2009.

[24] Https://www.dieselnet.com/standards/eu, "Automotive Diesel Fuel."

[25] Https://www.uop.com/, "More Diesel to Reflect A Changing Market."

[26] Http://www.hydrocarbonprocessing.com/magazine/2016, "Business Trends: Clean fuels - a global shift to a low-sulfur world," 2016.

[27] M. Booth, J. G. Buglass, and J. F. Unsworth, "Tailoring fuels for the new millennium," *Topics in Catalysis Vols*, vol. 16, pp. 1–4, 2001.

[28] D. Coley, *Energy and climate change: creating a sustainable future*. John Wiley, 2008.

[29] J. Dumesic, G. Huber, and M. Boudart, "Principles of Heterogeneous Catalysis," in *Handbook of Heterogeneous Catalysis*, pp. 1–15, Weinheim, Germany: Wiley-VCH Verlag GmbH & Co. KGaA, mar 2008.

[30] J. M. Thomas, "The societal significance of catalysis and the growing practical importance of single-site heterogeneous catalysts," *Proceedings of the Royal Society A: Mathematical, Physical and Engineering Sciences*, vol. 468, no. 2143, pp. 1884–1903, 2012.

[31] M. Männikkö, X. Wang, M. Skoglundh, and H. Härelind, "Characterization of the active species in the silver/alumina system for lean NO x reduction with methanol," *Catalysis Today*, vol. 267, pp. 76–81, 2016.

[32] L. Ström, A. Carlsson, M. Skoglundh, and H. Härelind, "Hydrogen-assisted SCR of NO x over alumina-supported silver and indium catalysts using C 2 -hydrocarbons and oxygenates," *Applied Catalysis B-Environmental*, vol. 181, pp. 403–412, 2016.

[33] H. Topsøe, B. Clausen, and F. Massoth, *Hydrotreating Catalysis Science and Technology*. Springer Verlag, 1996.

[34] W. Bensch, *Comprehensive Inorganic Chemistry II*. Elsevier, 2013.

[35] T. C. Ho, "Deep HDS of diesel fuel: chemistry and catalysis," *Catalysis Today*, vol. 98, no. 1, pp. 3–18, 2004.

[36] K. G. Knudsen, B. H. Cooper, and H. Topsøe, "Catalyst and process technologies for ultra low sulfur diesel," *Applied Catalysis A: General*, vol. 189, pp. 205–215, 1999.

[37] D. D. Whitehurst, T. Isoda, and I. Mochida, "Present State of the Art and Future Challenges in the Hydrodesulfurization of Polyaromatic Sulfur Compounds," *Advances in Catalysis*, vol. 42, pp. 345–471, 1998.

[38] N. Musselwhite and G. a. Somorjai, "Investigations of Structure Sensitivity in Heterogeneous Catalysis: From Single Crystals to Monodisperse Nanoparticles," *Topics in Catalysis*, vol. 56, pp. 1277–1283, aug 2013.

[39] D. Blakely, E. Kozak, B. Sexton, and G. Somorjai, "New instrumentation and techniques to monitor chemical surface reactions on single crystals over a wide pressure range (10-8 - 10 5 Torr) in the same apparatus," *Journal of Vacuum Science and Technology*, vol. 13, pp. 1091–1096, 1976.

[40] R. Hua, J. Wang, H. Kong, J. Liu, X. Lu, and G. Xu, "Analysis of sulfur-containing compounds in crude oil by comprehensive two-dimensional gas chromatography with sulfur chemiluminescence detection," *Journal of Separation Science*, vol. 27, no. 9, pp. 691–698, 2004.

[41] T. Olson, "An Oil Refinery Walk-Through," *Chemical Engineering Progress*, 2014.

[42] Https://www.eia.gov/energyexplained/, "Where Our Oil Comes From - Energy Explained, Your Guide To Understanding Energy - Energy Information Administration."

[43] A. Stanislaus, A. Marafi, and M. Rana, "Recent advances in the science and technology of ultra low sulfur diesel (ULSD) production," *Catalysis Today*, vol. 153, pp. 1–68, jul 2010.

[44] M. L. Vrinat, "The kinetics of the hydrodesulfurization process - a review," *Applied Catalysis*, vol. 6, no. 2, pp. 137–158, 1983.

[45] I. Babich and J. Moulijn, "Science and technology of novel processes for deep desulfurization of oil refinery streams: a review," *Fuel*, vol. 82, pp. 607–631, 2003.

[46] H. Topsøe, K. Knudsen, L. Byskov, J. Nørskov, and B. Clausen, "Advances in Deep Desulfurization," in *Science and Technology in Catalysis*, pp. 13–22, 1998.

[47] Q. Qusro and F. Massoth, "Comparison of high and low pressure HDS activities for Mo/Al2O3 Catalysts." 1987.

[48] R. Shafi and G. Hutchings, "Hydrodesulfurization of hindered dibenzothiophenes: an overview," *Catalysis Today*, vol. 59, no. 3-4, pp. 423–442, 2000.

[49] L. D. Rollmann, "Catalytic Hydrogenation of Model Nitrogen, Sulfur, and Oxygen Compounds," *Journal of Catalysis*, vol. 46, pp. 243–252, 1977.

[50] D. Kilanowski, H. Teeuwen, V. de Beer, B. C. Gates, G. Schuit, and H. Kwart, "Hydrodesulfurization of thiophene, benzothiophene, dibenzothiophene, and related compounds catalyzed by sulfided CoO-MoO3/y-Al2O3: Low-pressure reactivity studies," *Journal of Catalysis*, vol. 55, no. 2, pp. 129–137, 1978.

[51] A. Borgna, E. Hensen, J. Van Veen, and J. Niemantsverdriet, "Intrinsic kinetics of thiophene hydrodesulfurization on a sulfided NiMo/SiO 2 planar model catalyst," *Journal of Catalysis*, vol. 221, pp. 541–548, 2004.

[52] P. Moses, B. Hinnemann, H. Topsoe, and J. Norskov, "The hydrogenation and direct desulfurization reaction pathway in thiophene hydrodesulfurization over MoS2 catalysts at realistic conditions: A density functional study," *Journal of Catalysis*, vol. 248, pp. 188–203, jun 2007.

[53] P. G. Moses, B. Hinnemann, H. Topsøe, and J. K. Nørskov, "The effect of Co-promotion on MoS2 catalysts for hydrodesulfurization of thiophene: A density functional study," *Journal of Catalysis*, vol. 268, pp. 201–208, dec 2009.

[54] M. Houalla, D. H. Broderick, A. V. Sapre, N. K. Nag, V. H. J. de Beer, B. C. Gates, H. Kwart, and O. F. Catalysis, "Hydrodesulfurization of methyl-substituted dibenzothiophenes catalyzed by sulfided Co-Mo γ-Al2O3," *Journal of Catalysis*, vol. 61, no. 2, pp. 523–527, 1980.

[55] T. Kabe, A. Ishihara, and H. Tajima, "Hydrodesulfurization of Sulfur-Containing Polyaromatic Compounds in Light Oil," *Industrial & Engineering Chemistry Research*, vol. 31, pp. 1577–1580, 1992.

[56] T. Kabe, A. Ishihara, and Q. Zhang, "Deep desulfurization of light oil. Part 2: hydrodesulfurization of dibenzothiophene, 4- methyldibenzothiophene and 4,6- dimethyldibenzothiophene," *Applied Catalysis A: General*, vol. 97, 1993.

[57] B. Gates and H. Topsøe, "Reactivities in deep catalytic hydrodesulfurization: challenges, opportunities, and the importance of 4-methyldibenzothiophene and 4,6-dimethyldibenzothiophene," *Polyhedron*, vol. 16, no. 18, pp. 3213–3217, 1997.

[58] C. Song, "An overview of new approaches to deep desulfurization for ultra-clean gasoline, diesel fuel and jet fuel," *Catalysis Today*, vol. 86, pp. 211–263, nov 2003.

[59] S. Grønborg, M. Šaric, P. Moses, J. Rossmeisl, and J. Lauritsen, "Atomic scale analysis of sterical effects in the adsorption of 4,6-dimethyldibenzothiophene on a CoMoS hydrotreating catalyst," *Journal of Catalysis*, vol. 344, pp. 121–128, 2016.

[60] C. Song and X. Ma, "New design approaches to ultra-clean diesel fuels by deep desulfurization and deep dearomatization," *Applied Catalysis B: Environmental*, vol. 41, pp. 207–238, mar 2003.

[61] J. Wilcoxon, T. Thurston, and J. Martin, "Applications of metal and semiconductor nanoclusters as thermal and photo-catalysts," *Nanostructured Materials*, vol. 12, pp. 993–997, 1999.

[62] T. F. Jaramillo, K. P. Jørgensen, J. Bonde, J. H. Nielsen, S. Horch, and I. Chorkendorff, "Identification of active edge sites for electrochemical H2 evolution from MoS2 nanocatalysts.," *Science (New York, N.Y.)*, vol. 317, pp. 100–102, jul 2007.

[63] M. A. Lukowski, A. S. Daniel, F. Meng, A. Forticaux, L. Li, and S. Jin, "Enhanced Hydrogen Evolution Catalysis from Chemically Exfoliated Metallic MoS 2 Nanosheets," *Journal of American Chemical Society*, vol. 135, pp. 10274–10277, 2013.

[64] J. Kibsgaard, T. Jaramillo, and F. Besenbacher, "Building an appropriate active-site motif into a hydrogen-evolution catalyst with thiomolybdate [Mo3S13]2- clusters.," *Nature chemistry*, vol. 6, pp. 248–253, mar 2014.

[65] M. Bollinger, K. Jacobsen, and J. Nørskov, "Atomic and electronic structure of MoS2 nanoparticles," *Physical Review B*, vol. 67, p. 85410, feb 2003.

[66] J. Lauritsen, S. Helveg, E. Lægsgaard, I. Stensgaard, B. Clausen, H. Topsøe, and F. Besenbacher, "Atomic-Scale Structure of Co-Mo-S Nanoclusters in Hydrotreating Catalysts." 2001.

[67] B. Hinnemann, P. Moses, and J. Nørskov, "Recent density functional studies of hydrodesulfurization catalysts: insight into structure and mechanism," *J. Phys.: Condens. Matter*, vol. 20, no. 20, 2008.

[68] N.-Y. Topsøe and H. Topsøe, "IR spectroscopic studies of the nature of surface sites in hydrotreating catalysts," *Journal of Electron Spectroscopy and Related Phenomena Elsevier Science Publishers B.V*, vol. 39, pp. 11–13, 1986.

[69] A. Walton, J. V. Lauritsen, H. Topsøe, F. Besenbacher, a.S. Walton, J. V. Lauritsen, H. Topsøe, and F. Besenbacher, "MoS2 nanoparticle morphologies in hydrodesulfurization catalysis studied by scanning tunneling microscopy," *Journal of Catalysis*, vol. 308, pp. 306–318, dec 2013.

[70] S. Helveg, J. Lauritsen, E. Lægsgaard, I. Stensgaard, J. Nørskov, B. Clausen, H. Topsøe, and F. Besenbacher, "Atomic-Scale Structure of Single-Layer MoS 2 Nanoclusters," *Physical Review Letters*, vol. 84, no. 5, pp. 951–954, 2000.

[71] L. van Haandel, G. M. Bremmer, E. J. M. Hensen, and T. Weber, "Influence of sulfiding agent and pressure on structure and performance of CoMo/Al2O3 hydrodesulfurization catalysts," *Journal of Catalysis*, vol. 342, pp. 27–39, 2016.

[72] M. Daage, R. Chianelli, and A. Ruppert, "Structure-function relations in layered transition metal sulfide catalysts," in *New Frontiers in Catalysis*, pp. 571–584, 1993.

[73] W. Hofer, A. Foster, and L. Shluger, "Theories of scanning probe microscopes at the atomic scale," *Reviews of Modern Physics*, vol. 75, pp. 1287–1331, 2003.

[74] A. Bruix, H. Füchtbauer, A. Tuxen, A. Walton, M. Andersen, S. Porsgaard, F. Besenbacher, B. Hammer, J. V. Lauritsen, H. G. Füchtbauer,

A. K. Tuxen, A. S. Walton, M. Andersen, and S. Porsgaard, "In Situ Detection of Active Edge Sites in Single-Layer MoS 2 Catalysts," no. 9, pp. 9322–9330, 2015.

[75] J. Kibsgaard, J. Lauritsen, E. Lægsgaard, B. Clausen, H. Topsøe, and F. Besenbacher, "Cluster-Support Interactions and Morphology of MoS 2 Nanoclusters in a Graphite-Supported Hydrotreating Model Catalyst," *Journal of the American Chemical Society*, vol. 128, pp. 13950–13958, 2006.

[76] H. Beuther, R. Flinn, and J. Mckinley, "For Better Hydrodesulfurization Activity of Promoted Molybdenum Oxide-Alumina Catalysts," *Industrial & Engineering Chemistry Research*, vol. 51, no. 11, pp. 1349–1350, 1959.

[77] H. Topsøe, B. S. Clausen, R. Candia, C. Wivel, and S. Mørup, "In situ Mössbauer emission spectroscopy studies of unsupported and supported sulfided Co-Mo hydrodesulfurization catalysts: Evidence for and nature of a Co-Mo-S phase," *Journal of Catalysis*, vol. 68, no. 2, pp. 433–452, 1981.

[78] L. S. Byskov, J. K. Nørskov, B. S. Clausen, and H. Topsøe, "DFT Calculations of Unpromoted and Promoted MoS 2 -Based Hydrodesulfurization Catalysts," *Journal of Catalysis*, vol. 187, pp. 109–122, 1999.

[79] H. Topsøe, "The role of Co-Mo-S type structures in hydrotreating catalysts," *Applied Catalysis A: General*, vol. 322, pp. 3–8, 2007.

[80] F. Besenbacher, M. Brorson, B. Clausen, S. Helveg, B. Hinnemann, J. Kibsgaard, J. Lauritsen, P. Moses, J. Nørskov, and H. Topsøe, "Recent STM, DFT and HAADF-STEM studies of sulfide-based hydrotreating catalysts: Insight into mechanistic, structural and particle size effects," *Catalysis Today*, vol. 130, pp. 86–96, 2008.

[81] J. Kibsgaard, A. Tuxen, K. Knudsen, M. Brorson, H. Topsøe, E. Laegsgaard, J. Lauritsen, and F. Besenbacher, "Comparative atomic-scale analysis of promotional effects by late 3d-transition metals in MoS 2 hydrotreating catalysts," *Journal of Catalysis*, vol. 272, pp. 195–203, 2010.

[82] Y. Zhu, Q. M. Ramasse, M. Brorson, P. G. Moses, L. P. Hansen, H. Topsøe, C. F. Kisielowski, and S. Helveg, "Location of Co and Ni promoter atoms in multi-layer MoS 2 nanocrystals for hydrotreating catalysis," *Catalysis Today*, vol. 261, pp. 75–81, 2016.

[83] P. Raybaud, J. Hafner, G. Kresse, S. Kasztelan, and H. Toulhoat, "Structure, Energetics, and Electronic Properties of the Surface of a Promoted MoS2 Catalyst: An ab Initio Local Density Functional Study," *Journal of Catalysis*, vol. 190, pp. 128–143, 2000.

[84] H. Schweiger, P. Raybaud, and H. Toulhoat, "Promoter Sensitive Shapes of Co(Ni)MoS Nanocatalysts in Sulfo-Reductive Conditions," *Journal of Catalysis*, vol. 212, pp. 33–38, 2002.

[85] J. Lauritsen, J. Kibsgaard, G. Olesen, P. Moses, B. Hinnemann, S. Helveg, J. Nørskov, B. Clausen, H. Topsøe, E. Lægsgaard, and F. Besenbacher, "Location and coordination of promoter atoms in Co- and Ni-promoted MoS2-based hydrotreating catalysts," *Journal of Catalysis*, vol. 249, pp. 220–233, jul 2007.

[86] M. Girgis and B. Gates, "Reactivities, reaction networks, and kinetics in high-pressure catalytic hydroprocessing," *Industrial & Engineering Chemistry Research*, vol. 30, pp. 2021–2058, sep 1991.

[87] F. van Looij, P. van der Laan, W. Stork, D. DiCamillo, and J. Swain, "Key parameters in deep hydrodesulfurization of diesel fuel," *Applied Catalysis A: General*, vol. 170, no. 1, pp. 1–12, 1998.

[88] P. Zeuthen, K. G. Knudsen, and D. Whitehurst, "Organic nitrogen compounds in gas oil blends, their hydrotreated products and the importance to hydrotreatment," *Catalysis Today*, vol. 65, no. 2, pp. 307–314, 2001.

[89] R. Bartsch and C. Tanielian, "Hydrodesulfurization I. Hydrogenolysis of Benzothiophene and Dibenzothiophene over CoO-MoO3-Al203 Catalyst," *Journal of Catalysis*, vol. 35, pp. 353–358, 1974.

[90] M. Houalla, N. Nag, A. Sapre, D. Broderick, and B. Gates, "Hydrodesulfurization of Dibenzothiophene Catalyzed by Sulfided CoO-MoO3 y-Al2O3: The Reaction Network," *ACS Division of Fuel Chemistry, Preprints*, vol. 24, pp. 1015–1021, 1978.

[91] G. H. Singhal, R. L. Espino, and J. E. Sobel, "Hydrodesulfurization of sulfur heterocyclic compounds: Reaction mechanisms," *Journal of Catalysis*, vol. 67, no. 2, pp. 446–456, 1981.

[92] X. Li, A. Wang, M. Egorova, and R. Prins, "Kinetics of the HDS of 4,6-dimethyldibenzothiophene and its hydrogenated intermediates over sulfided Mo and NiMo on γ -Al 2 O 3," *Journal of Catalysis*, vol. 250, pp. 283–293, 2007.

[93] N. Hermann, M. Brorson, and H. Topsøe, "Activities of unsupported second transition series metal sulfides for hydrodesulfurization of sterically hindered 4 , 6-dimethyldibenzothiophene and of unsubstituted dibenzothiophene," *Catalysis Letters*, vol. 65, pp. 169–174, 2000.

[94] A. Tuxen, H. Füchtbauer, B. Temel, B. Hinnemann, H. Topsøe, K. Knudsen, F. Besenbacher, and J. Lauritsen, "Atomic-scale insight into adsorption of sterically hindered dibenzothiophenes on MoS2 and Co-Mo-S hydrotreating catalysts," *Journal of Catalysis*, vol. 295, pp. 146–154, nov 2012.

[95] J. V. Lauritsen and F. Besenbacher, "Atom-resolved scanning tunneling microscopy investigations of molecular adsorption on MoS2 and CoMoS hydrodesulfurization catalysts," *Journal of Catalysis*, vol. 328, pp. 49–58, aug 2015.

[96] M. Šaric, J. Rossmeisl, and P. Moses, "Modeling the active sites of Co-promoted MoS 2 particles by DFT," *Phys. Chem. Chem. Phys. Phys. Chem. Chem. Phys*, vol. 19, no. 19, pp. 2017–2024, 2017.

[97] A. Tuxen, J. Kibsgaard, H. Gøbel, E. Laegsgaard, H. Topsøe, J. Lauritsen, and F. Besenbacher, "Size Threshold in the Dibenzothiophene Adsorption on MoS 2 Nanoclusters," *ACS Nano*, vol. 4, no. 8, pp. 4677–4682, 2010.

[98] H. Farag, D. D. Whitehurst, K. Sakanishi, and I. Mochida, "Improving kinetic analysis of sequential and parallel reactions of hydrodesulfurization of dibenzothiophenes by establishing reasonable boundaries for reaction rate constants," *Catalysis Today*, vol. 50, pp. 49–56, 1999.

[99] M. Macaud, "Hydrodesulfurization of Alkyldibenzothiophenes: Evidence of Highly Unreactive Aromatic Sulfur Compounds," *Journal of Catalysis*, vol. 193, pp. 255–263, jul 2000.

[100] M. Egorova and R. Prins, "The role of Ni and Co promoters in the simultaneous HDS of dibenzothiophene and HDN of amines over Mo/γ -Al 2 O 3 catalysts," *Journal of Catalysis*, vol. 241, pp. 162–172, 2006.

[101] D. Edwards and J. Prausnitz, "Vapor Pressures of Some Sulfur-Containing, Coal-Related Compounds," *Journal of Chemical and Engineering Data*, vol. 26, no. 2, pp. 121–124, 1981.

[102] Https://comptox.epa.gov/dashboard/, "Dibenzothiophene," 2017.

[103] Https://comptox.epa.gov/dashboard/, "4,6-Dimethyldibenzothiophene," 2017.

[104] Http://webbook.nist.gov/, "Dibenzothiophene," 2017.

[105] Y. Xu, H. Shang, R. Zhao, and C. Liu, "The Studies of Hydrodesulfurization of 4,6 Dimethyldibenzothiophene on Sulfided Mo/(gamma)-Al2O3: The Effects of Reactive Temperature and Pressure," *Preprints of Papers American Chemical Society, Division of Fuel*, vol. 49, no. 1, pp. 343–345, 2004.

[106] Http://webbook.nist.gov/, "4,6-Dimethyldibenzothiophene," 2017.

[107] K. F. Jensen, "Microreaction engineering - is small better?," *Chemical Engineering Science*, vol. 56, no. 2, pp. 293–303, 2001.

[108] T. Henriksen, J. Olsen, P. Vesborg, I. Chorkendorff, and O. Hansen, "Highly sensitive silicon microreactor for catalyst testing.," *The Review of scientific instruments*, vol. 80, p. 124101, dec 2009.

[109] T. Henriksen, *Silicon Microreactors for Measurements of Catalytic Activity*. PhD thesis, 2010.

[110] D. B. Trimarco, T. Pedersen, O. Hansen, I. Chorkendorff, and P. C. K. Vesborg, "Fast and sensitive method for detecting volatile species in liquids," *Review of Scientific Instruments*, vol. 86, p. 075006, jul 2015.

[111] T. Andersen, R. Jensen, M. Christensen, T. Pedersen, O. Hansen, and I. Chorkendorff, "High mass resolution time of flight mass spectrometer for measuring products in heterogeneous catalysis in highly sensitive microreactors," *Review of Scientific Instruments*, vol. 83, p. 075105, jul 2012.

[112] J. N. Riedel, M. D. Rötzer, M. Jørgensen, U. G. Vej-Hansen, T. Pedersen, B. Sebok, F. F. Schweinberger, P. C. K. Vesborg, O. Hansen, J. Schiøtz, U. Heiz, and I. Chorkendorff, "H2/D2 exchange reaction on mono-disperse Pt clusters: enhanced activity from minute O2 concentrations," *Catal. Sci. Technol.*, vol. 6, pp. 6893–6900, 2016.

[113] A. Roth, "Gas flow at low pressures," in *Vacuum Technology*, pp. 62–148, 1990.

[114] J. O'Hanlon, *A User's Guide to Vacuum Technology*. 2003.

[115] G. Wallis and D. I. Pomerantz, "Field assisted glass-metal sealing," *Journal of Applied Physics*, vol. 40, no. 10, pp. 3946–3949, 1969.

[116] A. Lapadatu and H. Jakobsen, *Anodic Bonding*. Elsevier Inc, 2010.

[117] T. R. Anthony, "Anodic bonding of imperfect surfaces," *Journal of Applied Physics*, vol. 54, no. 5, pp. 2419–2428, 1983.

[118] P. Vesborg, J. Olsen, T. Henriksen, I. Chorkendorff, and O. Hansen, "Note: Anodic bonding with cooling of heat-sensitive areas," *Review of Scientific Instruments*, vol. 81, no. 1, 2010.

[119] M. Guilhaus, "Principles and instrumentation in time-of-flight mass spectrometry: Physical and instrumental concepts," *Journal of Mass Spectrometry*, vol. 30, no. 11, pp. 1519–1532, 1995.

[120] R. Jensen, *Microreactors for Heterogeneous Catalysis*. PhD thesis, 2012.

[121] Pfeiffer Vacuum, "6.3 Quadrupole mass spectrometers (QMS)."

[122] I. Jordan TOF Products, *Instruction manual*. 2015.

[123] Https://github.com/CINF/PyExpLabSys, "Fix mass axis," 2017.

[124] Https://github.com/CINF/PyExpLabSys, "Spectrum plotter," 2017.

[125] A. Niquille-Röthlisberger and R. Prins, "Hydrodesulfurization of 4,6-dimethyldibenzothiophene and dibenzothiophene over alumina-supported Pt, Pd, and Pt-Pd catalysts," *Journal of Catalysis*, vol. 242, pp. 207–216, 2006.

[126] V. Baldovino-Medrano, P. Eloy, E. Gaigneaux, S. Giraldo, and A. Centeno, "Factors controlling the development of the HYD route of desulfurization of DBT over γ-alumina supported Pt and Pd catalysts," *Catalysis Today*, vol. 150, pp. 186–195, 2010.

[127] I. Lee and F. Zaera, "Nanoparticle Shape Selectivity in Catalysis: Butene Isomerization and Hydrogenation on Platinum," *Topics in Catalysis*, vol. 56, pp. 1284–1298, jul 2013.

[128] C. Castillo-Araiza, G. Chávez, A. Dutta, J. de los Reyes, S. Nuñez, and J. García-Martínez, "Role of Pt-Pd/γ-Al2O3 on the HDS of 4,6-DMBT: Kinetic modeling & contribution analysis," *Fuel Processing Technology*, vol. 132, pp. 164–172, 2015.

[129] S. Haji, Y. Zhang, and C. Erkey, "Atmospheric hydrodesulfurization of diesel fuel using Pt/Al2O3 catalysts prepared by supercritical deposition for fuel cell applications," *Applied Catalysis A: General*, vol. 374, pp. 1–10, feb 2010.

[130] V. Baldovino-Medrano, P. Eloy, E. Gaigneaux, S. Giraldo, and A. Centeno, "Development of the HYD route of hydrodesulfurization of dibenzothiophenes over Pd-Pt/γ-Al2O3 catalysts," *Journal of Catalysis*, vol. 267, pp. 129–139, 2009.

[131] S. Chen, J. Chen, R. Gieleciak, and C. Fairbridge, "Reactivity characteristics of Pt-encapsulated zeolite catalysts for hydrogenation and hydrodesulfurization," *Applied Catalysis A: General*, vol. 415-416, pp. 70–79, 2011.

[132] S. Haji, Y. Zhang, D. Kang, M. Aindow, and C. Erkey, "Hydrodesulfurization of model diesel using Pt/Al2O3 catalysts prepared by supercritical deposition," *Catalysis Today*, vol. 99, no. 3, pp. 365–373, 2005.

[133] G. W. Thomson, "The Antoine equation for vapor-pressure data," *Chem. Rev*, vol. 38, no. 1, pp. 1–39, 1946.

[134] G. C. Sinke, "A method for measurement of vapor pressures of organic compounds below 0.1 Torr Naphthalene as a reference substance," *Journal of Chemical Thermodynamics*, vol. 6, pp. 311–316, 1974.

[135] A. De Jong, V. De Beer, J. Rob Van Veen, and H. Niemantsverdriet, "Surface Science Model of a Working Cobalt-Promoted Molybdenum Sulfide Hydrodesulfurization Catalyst: Characterization and Reactivity," *Journal of Physical Chemistry*, vol. 100, pp. 17722–17724, 1996.

[136] G. M. Bremmer, L. Van Haandel, E. J. M. Hensen, J. W. M. Frenken, and P. J. Kooyman, "Instability of NiMoS 2 and CoMoS 2 Hydrodesulfurization Catalysts at Ambient Conditions: A Quasi in Situ High-Resolution Transmission Electron Microscopy and X-ray Photoelectron Spectroscopy Study," *The Journal of Physical Chemistry C*, vol. 120, pp. 19204–19211, 2016.

[137] R. Dickinson and L. Pauling, "The crystal structure of molybdenite," *Journal of American Chemical Society*, vol. 45, no. 6, pp. 1466–1471, 1923.

Appendix A

TOF spectra

HDS of DBT

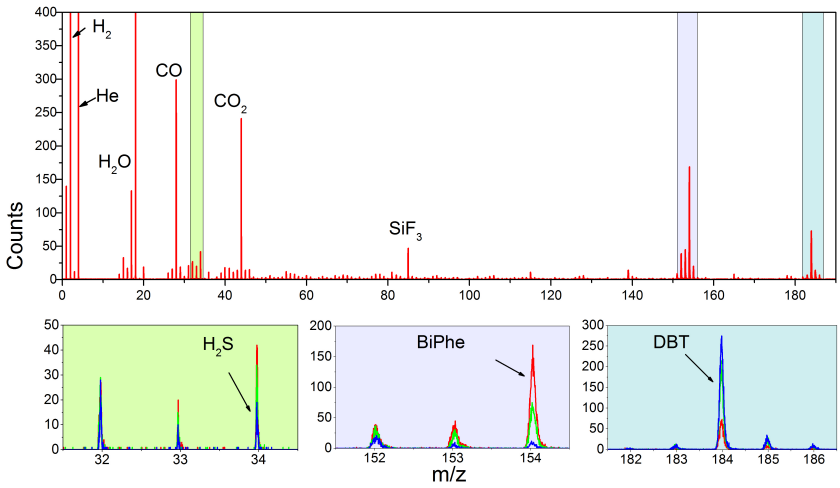

Figure A.1: *TOF mass spectrum of the HDS of DBT on a 185 kamu (∼3 nm) Pt sample (MR-04). The red and uppermost spectrum was obtained at 350° C and shows masses* m/z = *0-190. The insets below illustrate close-ups of three regions. In all insets the colors indicate: red spectrum: 350° C; green spectrum: 275° C; and blue spectrum: 200° C.*

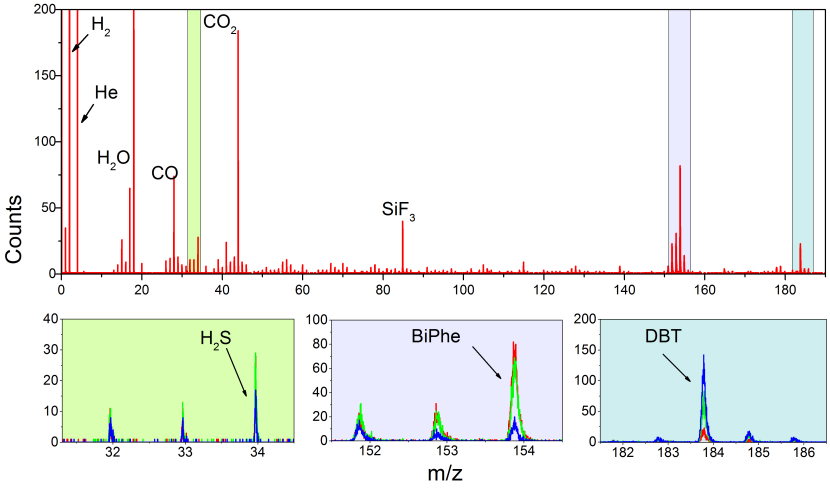

Figure A.2: *TOF mass spectrum of the HDS of DBT on a 185 kamu (∼3 nm) Pt sample (MR-06). The red and uppermost spectrum was obtained at 350° C and shows masses* m/z = *0-190. The insets below illustrate close-ups of three regions. In all insets the colors indicate: red spectrum: 350° C; green spectrum: 275° C; and blue spectrum: 200° C.*

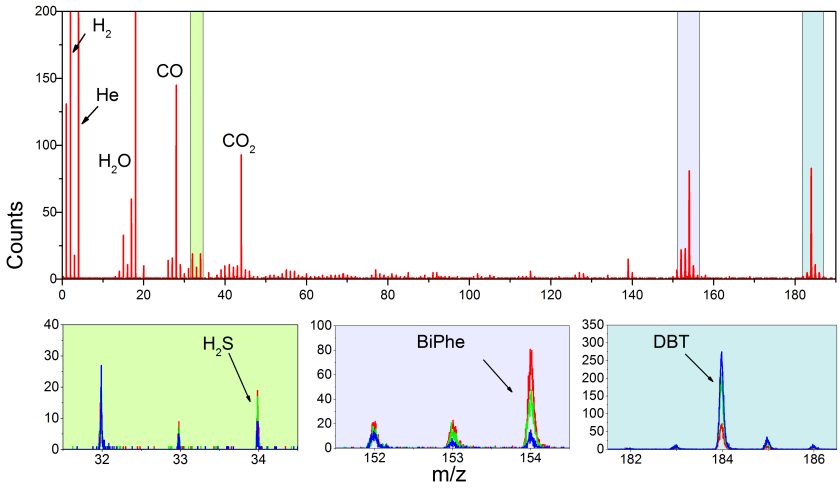

Figure A.3: *HDS of DBT on a 1500 kamu (∼6 nm) Pt sample (MR-01). The red and uppermost spectrum was obtained at 350° C and shows masses* m/z = *0-190. The insets below illustrate close-ups of three regions. In all insets the colors indicate: red spectrum: 350° C; green spectrum: 275° C; and blue spectrum: 200° C.*

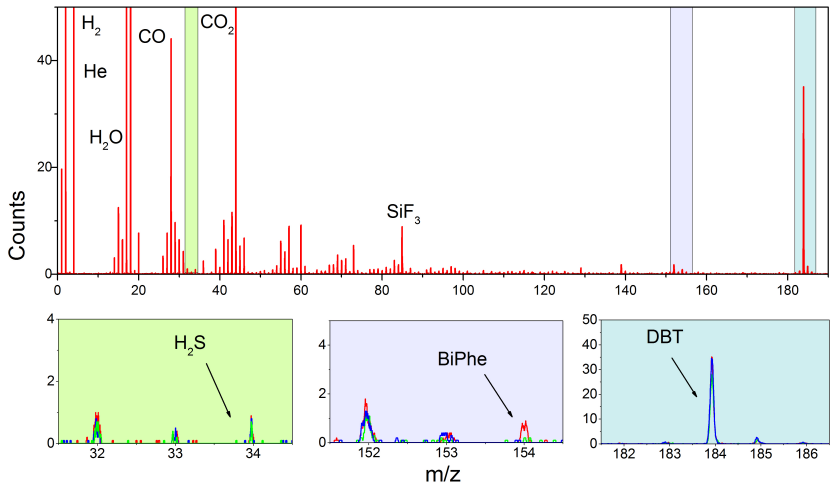

Figure A.4: *TOF spectra of HDS of DBT on a 195 amu Pt single atom sample (AnluMR-12). The red and uppermost spectrum was obtained at 350° C and shows masses* m/z = *0-190. The insets below illustrate close-ups of three regions. In all insets the colors indicate: red spectrum: 350° C; green spectrum: 275° C; and blue spectrum: 200° C.*

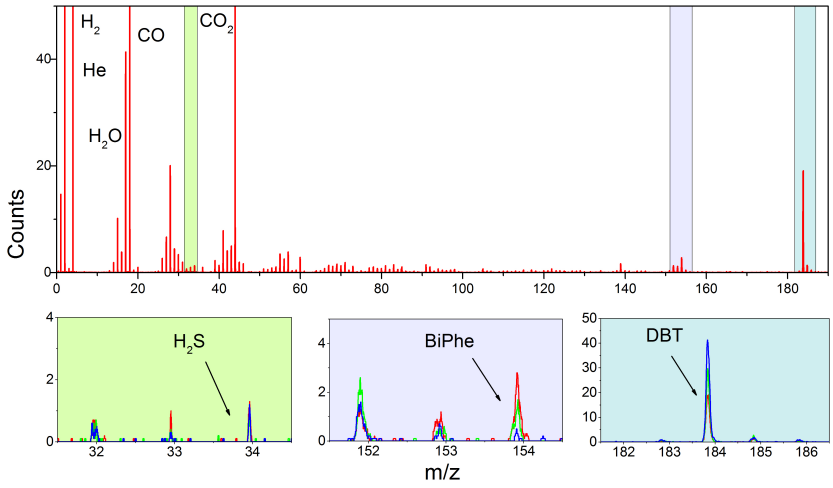

Figure A.5: *TOF spectra of HDS of DBT on a 195 amu Pt single atom sample (AnluMR-13). The red and uppermost spectrum was obtained at 350° C and shows masses* m/z = *0-190. The insets below illustrate close-ups of three regions. In all insets the colors indicate: red spectrum: 350° C; green spectrum: 275° C; and blue spectrum: 200° C.*

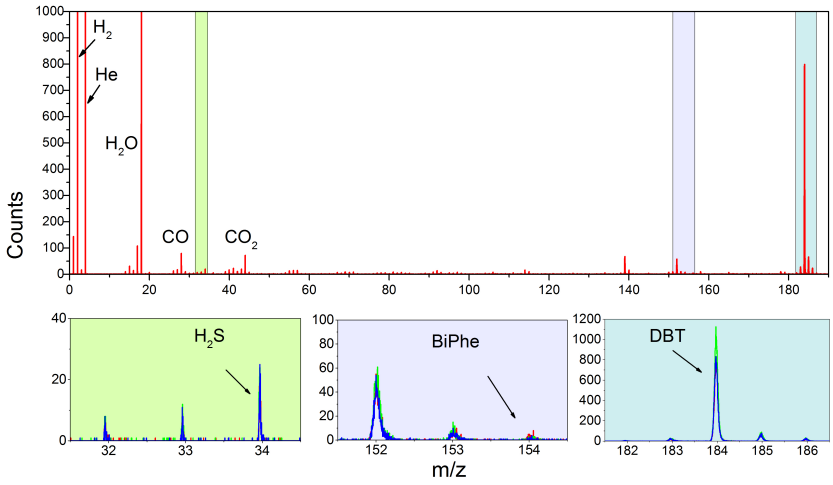

Figure A.6: *TOF spectra of the HDS of DBT on a 200 kamu as-prepared in-flight sulfided $NiMoS_x$ sample (MR-05). The red and uppermost spectrum was obtained at 350° C and shows masses* m/z = *0-190. The insets below illustrate close-ups of three regions. In all insets the colors indicate: red spectrum: 350° C; green spectrum: 275° C; and blue spectrum: 200° C.*

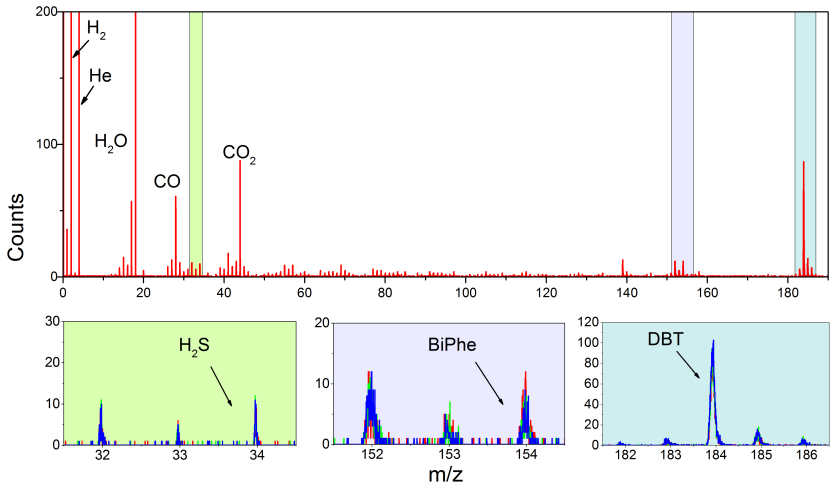

Figure A.7: *TOF spectra of the HDS of DBT on a 134 kamu as-prepared NiMo sample (MR-10). The red and uppermost spectrum was obtained at 350° C and shows masses* m/z = *0-190. The insets below illustrate close-ups of three regions. In all insets the colors indicate: red spectrum: 350° C; green spectrum: 275° C; and blue spectrum: 200° C.*

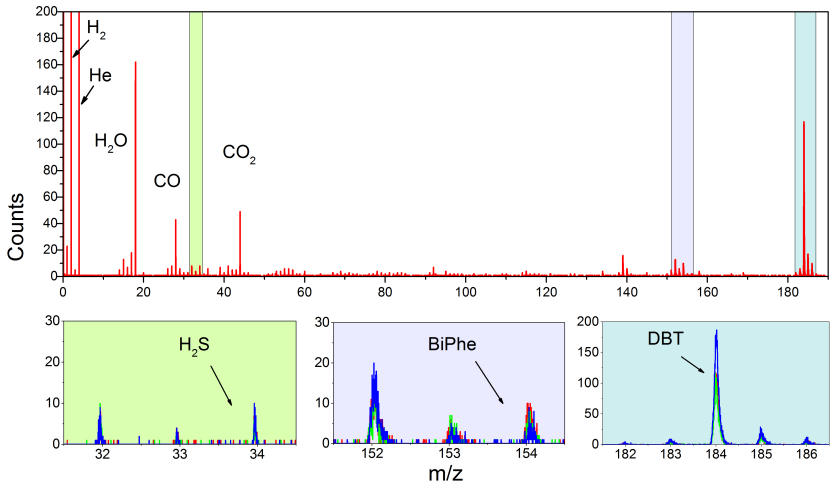

Figure A.8: *TOF spectra of the HDS of DBT on a 134 kamu NiMo sample (MR-10) sulfided in the μ-reactor at 1 bar 10,% H_2S in H_2 at 350° C for an hour. The red and uppermost spectrum was obtained at 350° C and shows masses* m/z = *0-190. The insets below illustrate close-ups of three regions. In all insets the colors indicate: red spectrum: 350° C; green spectrum: 275° C; and blue spectrum: 200° C.*

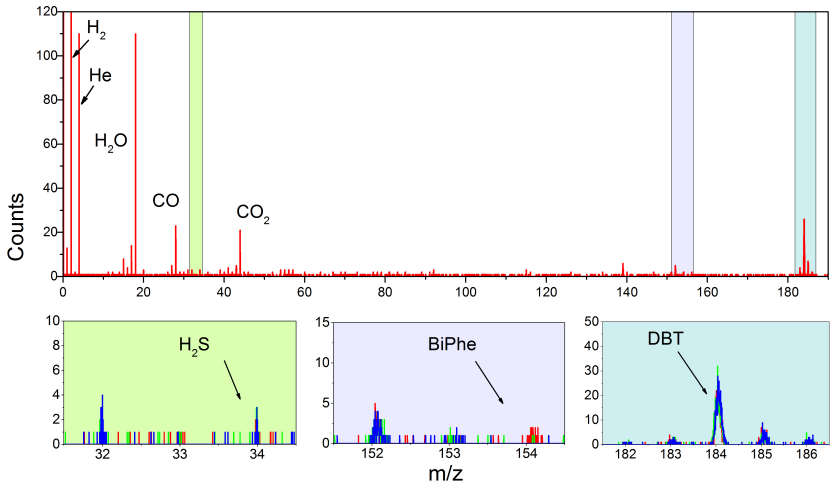

Figure A.9: *TOF spectra of the HDS of DBT on a 134 kamu as-prepared NiMo sample (MR-11). The red and uppermost spectrum was obtained at 350° C and shows masses* m/z = *0-190. The insets below illustrate close-ups of three regions. In all insets the colors indicate: red spectrum: 350° C; green spectrum: 275° C; and blue spectrum: 200° C.*

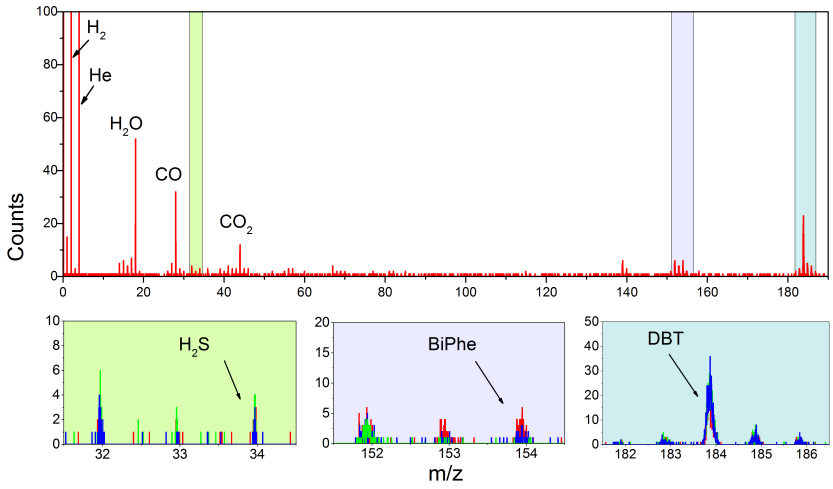

Figure A.10: *TOF spectra of the HDS of DBT on a 134 kamu NiMo sample (MR-11) sulfided in the μ-reactor at 1 bar 10,% H_2S in H_2 at 350° C for an hour. The red and uppermost spectrum was obtained at 350° C and shows masses* m/z = *0-190. The insets below illustrate close-ups of three regions. In all insets the colors indicate: red spectrum: 350° C; green spectrum: 275° C; and blue spectrum: 200° C.*

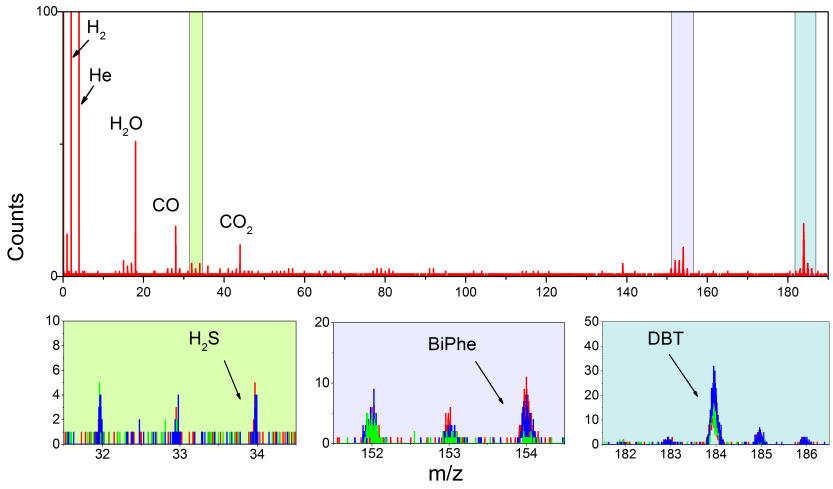

Figure A.11: *TOF spectra of the HDS of DBT on a 440 kamu in-flight sulfided $NiMoS_x$ sample (MR-12) re-sulfided in the μ-reactor at 1 bar 10 % H_2S in H_2 at 350° C for an hour. The red and uppermost spectrum was obtained at 300° C and shows masses from m/z = 0 to m/z = 190. The insets below illustrate close-ups of three regions. Red spectrum: 300° C; green spectrum: 250° C; and blue spectrum: 200° C.*

HDS of 4,6-DMDBT

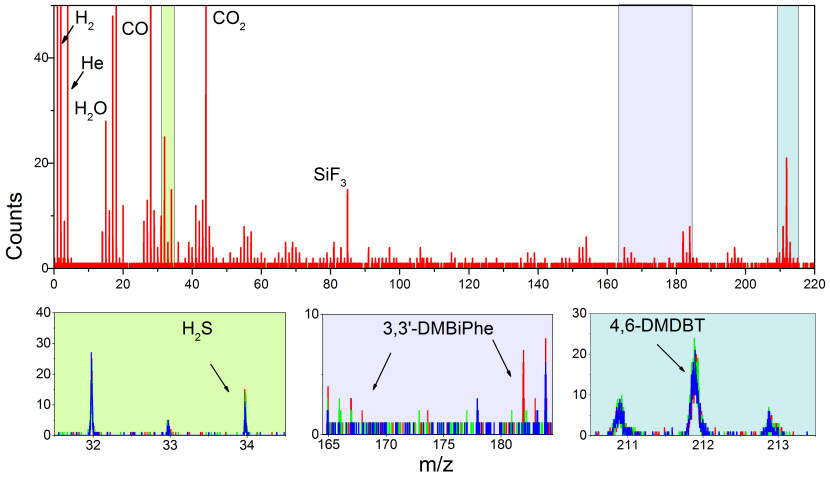

Figure A.12: *TOF spectra of the HDS of 4,6-DMDBT on a 185 kamu (∼3 nm) Pt sample (MR-04). The red and uppermost spectrum was obtained at 350° C and shows masses m/z = 0-220. The insets below illustrate close-ups of three regions. Red spectrum: 300° C; green spectrum: 250° C; and blue spectrum: 200° C.*

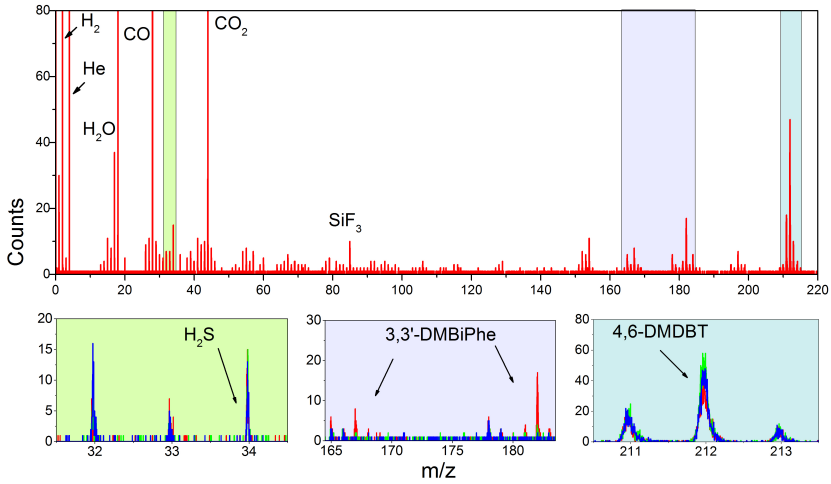

Figure A.13: *TOF spectra of the HDS of 4,6-DMDBT on a 185 kamu (∼3 nm) Pt sample (MR-06). The red and uppermost spectrum was obtained at 350° C and shows masses m/z = 0-220. The insets below illustrate close-ups of three regions. Red spectrum: 300° C; green spectrum: 250° C; and blue spectrum: 200° C.*

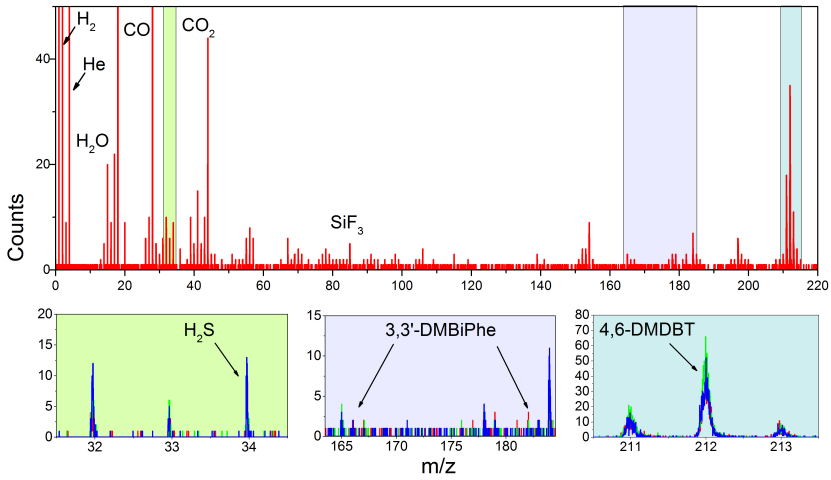

Figure A.14: *TOF spectra of the HDS of 4,6-DMDBT on a 1500 kamu (∼6 nm) Pt sample (MR-01). The red and uppermost spectrum was obtained at 350° C and shows masses m/z = 0-220. The insets below illustrate close-ups of three regions. Red spectrum: 300° C; green spectrum: 250° C; and blue spectrum: 200° C.*

Appendix B

Activity plots

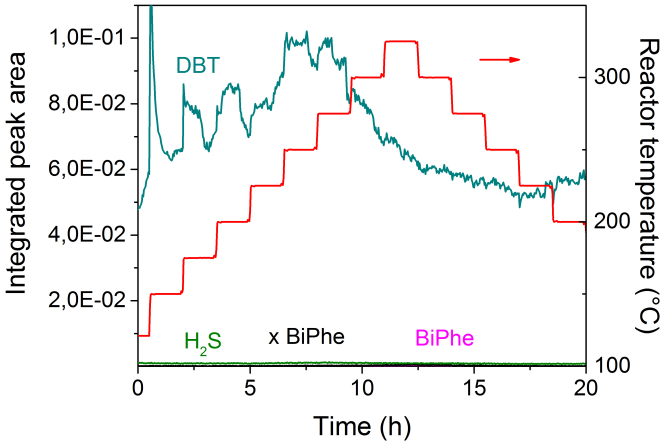

Figure B.1: *HDS of DBT on as-prepared 200 kamu in-flight sulfided $NiMoS_x$ (MR-05).*

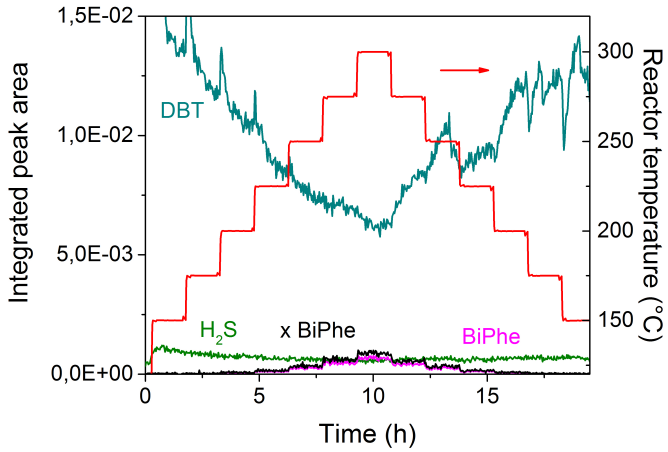

Figure B.2: *HDS of DBT on 200 kamu in-flight sulfided $NiMoS_x$ (MR-05) after a one hour oxidation in air at 400 mbar and 200 °C.*

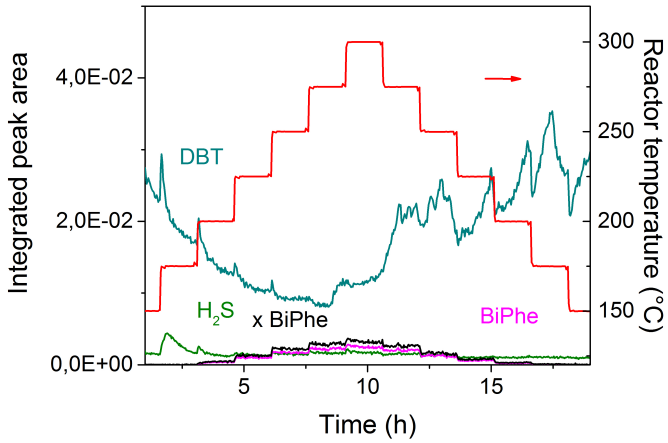

Figure B.3: *HDS of DBT on 200 kamu in-flight sulfided $NiMoS_x$ (MR-05) after the second one hour re-sulfidation in 1 bar of 10 % H_2S in H_2 at 350 °C.*

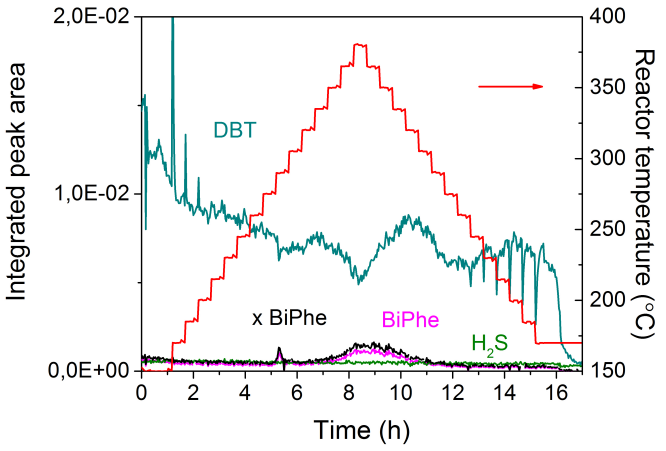

Figure B.4: *HDS of DBT on metallic 134 kamu NiMo nanoparticles (MR-10).*

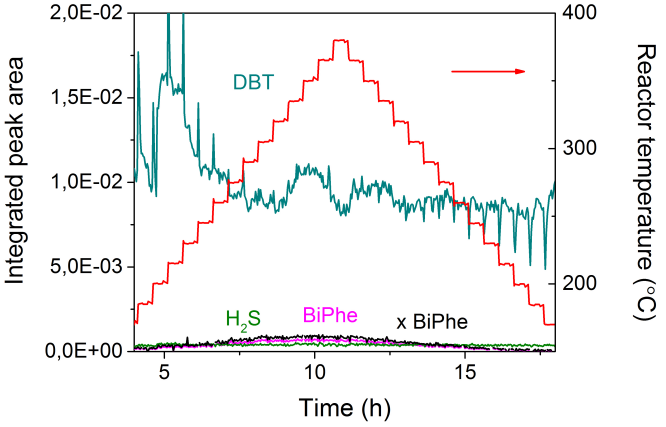

Figure B.5: *HDS of DBT on metallic 134 kamu NiMo (MR-10) after a one hour sulfidation in 1 bar of 10% H_2S in H_2 at 350 °in the μ-reactor.*

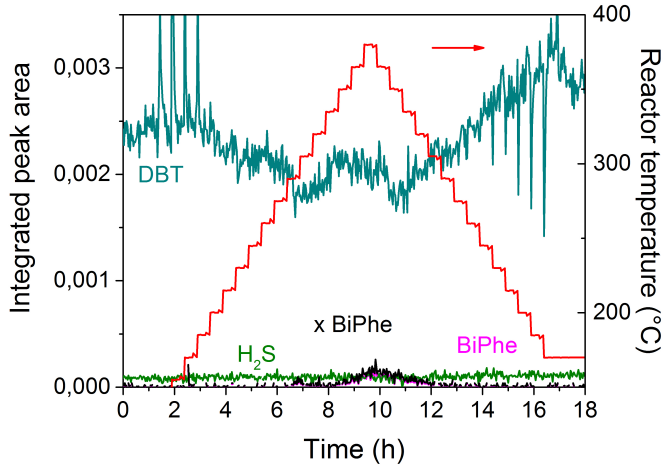

Figure B.6: *HDS of DBT on metallic 134 kamu NiMo nanoparticles (MR-11).*

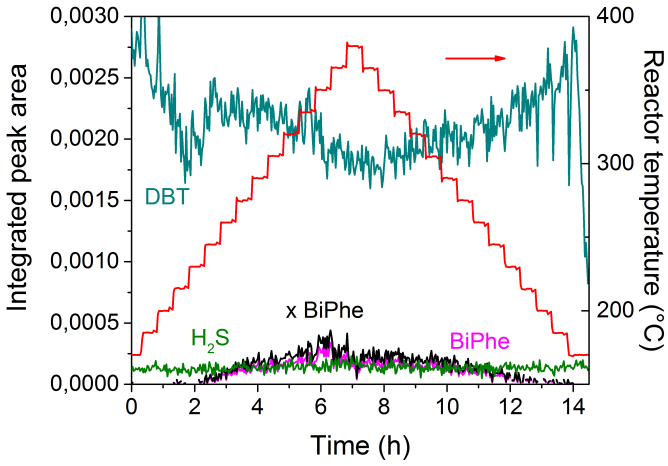

Figure B.7: *HDS of DBT on metallic 134 kamu NiMo (MR-11) after a one hour sulfidation in 1 bar of 10% H_2S in H_2 at 350 °in the μ-reactor.*

Paper 1

Ambient Pressure HDS of Refractory Sulfur Compounds in Highly Sensitive μ-reactor Platform Coupled to a Time-of-Flight Mass Spectrometer

In preparation. To be submitted to the Journal of Physical Chemistry C.

Ambient Pressure HDS of Refractory Sulfur Compounds in Highly Sensitive μ-reactor Platform Coupled to a Time-of-Flight Mass Spectrometer

Ann-Louise Nygård Christoffersen[1], Anders Bodin[1], Christian F. Elkjær[2], Jakob Ejler Sørensen[1], Jakob Kibsgaard[1], Ib Chorkendorff[1]

[1]*Department of Physics, Technical University of Denmark, Fysikvej, Building 312 DK-2800 Kgs. Lyngby, Denmark*

[2]*Haldor Topsøe A/S, Nymøllevej 55, DK-2800 Kgs. Lyngby, Denmark*

ABSTRACT

Tightened restrictions call for cleaner transportation fuels to minimize environmental and societal problems caused by the presence of sulfur in transportation fuels. This emphasizes the need for new and better catalysts in the field of hydrodesulfurization (HDS), which aims at removing the refractory sulfur from different petroleum streams mostly found in the form of the alkyl-substituted dibenzothiophenes (β -DBTs). In this work we demonstrate how a setup dedicated to testing minute amounts of well-defined catalytic systems in μ-reactors can be used in the gas phase HDS of the model compounds DBT and 4,6-dimethyldibenzothiophene (4,6-DMDBT) and the reaction pathways revealed by time-of-flight mass spectrometry. Specifically we investigate HDS of DBT and 4,6-DMDBT on mass-selected Pt nanoparticles, and show that only the direct desulfurization (DDS) products are formed. The setup is a means to bridge the gap between structural characterization of HDS catalysts and their related activity.

1. INTRODUCTION

Environmental concern combined with the unfortunate health related effects caused by the presence of sulfur compounds in transportation fuels have led to tightened legislation, demanding more efficient hydrodesulfurization (HDS) catalysts[1,2]. Industrial HDS is a high pressure catalytic process conducted at elevated temperatures in excess of molecular hydrogen to form H_2S and hydrocarbons[3–6]. The difficulties in producing ultra-low sulfur diesel (ULSD) increase with the need for processing increasingly heavier feed stocks with high amounts of alkyl-substituted dibenzothiophenes (β-DBTs), which are known to be the

most refractory sulfur-containing compounds found in crude oil[7–9].

Especially when the alkyl groups are located in the 4th and 6th position, the sulfur atom is sterically hindered[10–12], and reducing the total sulfur content to the sub ppm level remains a challenge. Designing catalysts that are able to spatially access the sulfur atom is therefore key to find better and more efficient catalysts for producing essentially "sulfur-free" diesel fuel[13,14], and DBT and 4,6-dimethyldibenzothiophene (4,6-DMDBT) are therefore often used as model molecules in HDS studies[15,16].

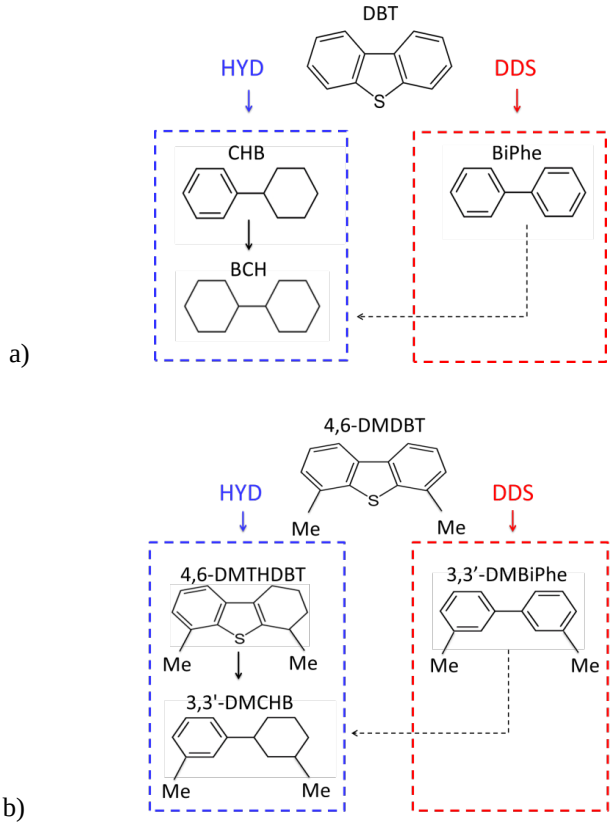

Figure 1 Reaction pathways of DBT (a) and 4,6-DMDBT (b). The direct desulfurization (DDS) pathway produces biphenyl (BiPhe) and 3,3'-dimethylbiphenyl (3,3'-DMBiPhe) respectively. The hydrogenation (HYD) pathway produces cyclohexylbenzene (CHB) and 3,3'-dimethylcyclohexylbenzene (3,3'-DMCHB) respectively.

Under the industrial HDS of DBT and 4,6-DMDBT, it is well-accepted that two different reaction pathways exist[17–20], which can be seen in Figure 1.

The hydrogenation (HYD) pathway of DBT and 4,6-DMDBT produces cyclohexylbenzene (CHB) and 3,3'-dimethylcyclohexylbenzene (3,3'-DMCHB), respectively, whereas the direct

desulfurization (DDS) occurs by hydrogenolysis of the C-S bonds followed by sulfur extrusion to form biphenyl (BiPhe) and 3,3-dimethylbiphenyl (3,3'-DMBiPhe), respectively[13,21,22]. It is well-accepted that DBT mainly reacts through the DDS pathway, whereas the sterically hindered 4,6-DMDBT mainly reacts through the HYD pathway[8,13,18].

Mass-selected nanoclusters and nanoparticles deposited onto well-defined substrates have gained increasing popularity as model catalysts[23–26]. Such models tested under controlled conditions represent a simplification of the complex nature of an industrial catalytic process, but may provide useful and crucial insight into the elementary steps of a catalytic reaction, especially when combined with surface sensitive characterization techniques[27,28]. Extensive density functional theory (DFT) and scanning tunneling microscopy (STM) studies on such clusters have revealed the adsorption mechanism of DBT and 4,6-DMDBT on well-defined MoS_2 based model systems[29,30] as well as the structure and promoter effects of Co and Ni[14,31,32]. These have been found to mostly decorate the edges of the MoS_2 basal planes, resulting in hexagonally truncated particle shapes, where especially the brim structure is of catalytic interest[33–36]. The detailed structural insight provided by this type of studies has hitherto not been directly linked to the catalytic activity of the model catalysts. Supported catalysts, on the other hand, provide a good basis for activity measurements, but these are however very heterogeneous with MoS_2 crystals of different shape and size[37] which hamper the ability to link activity to a specific structure.

With the work presented here, we attempt to bridge the gap between ambient pressure measurements and surface sensitive techniques by controlled catalytic measurements of small amounts of very homogeneous catalyst. To achieve this goal we have developed a setup dedicated to testing minute amounts of catalyst in the gas phase HDS of DBT and 4,6-DMDBT at ambient pressure. A specially designed µ-reactor platform coupled to a time-of-flight mass spectrometer (TOF-MS) enables high sensitivity and data acquisition with high temporal resolution of 200 ps and a mass resolution of $m/\Delta m = 2500$. In order to focus on the technical aspects of this setup, we present measurements on Pt, which is an active hydrogenation catalyst and at the same time represent a simpler case than the more complex MoS_2-based catalysts[19,38]. Monitoring the entire range of products enables us to link specific structures to specific products, hence elucidate the prevailing reaction pathway.

2. THE MODEL SYSTEM

The experimental setup consists of four main parts – see Figure 2. 1) The reactant dosing zone features two compound sources containing DBT and 4,6-DMDBT, respectively, enabling back-to-back activity measurements of both molecules. This allows for a detailed comparison between the relative reaction rates of the HDS of DBT and 4,6-DMDBT and can be a helpful means to gain insight into the similarities and differences in products and formation and reaction pathways on a given catalyst. 2) Catalytic conversion takes place in the µ-reactor platform and the outlet gas is directed through a narrow capillary into 3) a specially designed heat traced ionization zone which enables the use of 4) the TOF-MS, which is used for gas detection and analysis.

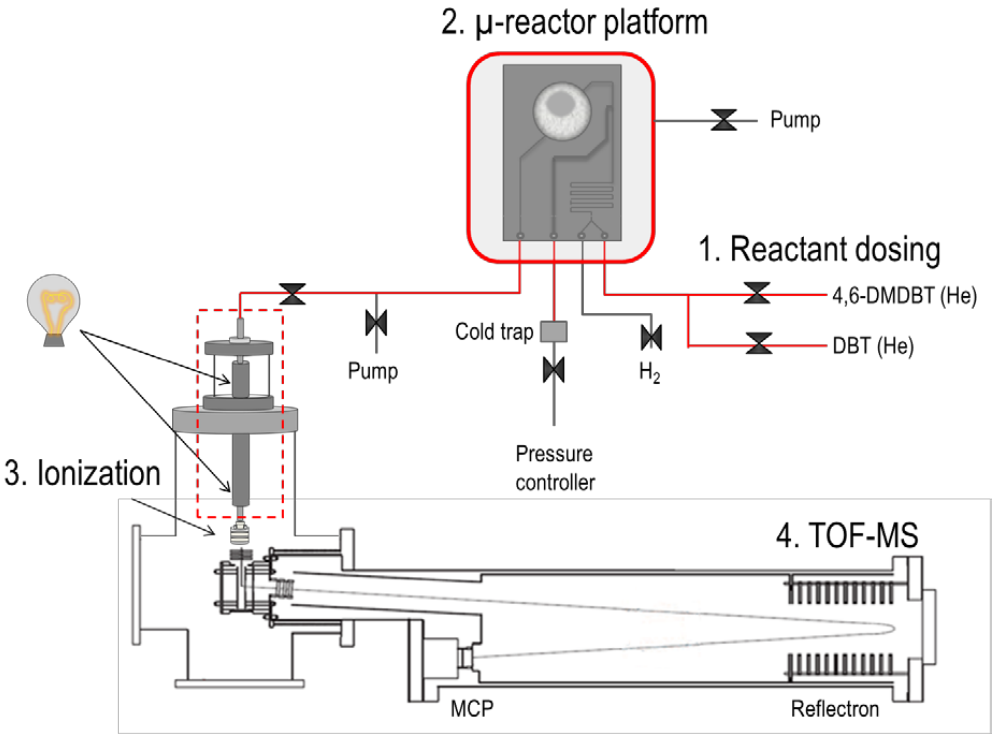

Figure 2 The experimental setup consists of four main parts. 1) The reactant dosing zone, 2) the µ-reactor platform, 3) an ionization area and 4) the time-of-flight mass spectrometer (TOF-MS). The red lines represents heat tracing.

2.1. Reactant dosing. The setup is designed so that HDS of DBT and 4,6-DMDBT can be performed back to back. Both compounds are put in homemade compound sources made from CF fittings. At room temperature the model compounds are solid crystals with vapor pressures well below 5×10^{-4} mbar[39,40] so heating is required in order to release a sufficient

amount at ambient pressure. The compound sources and valves are therefore equipped with heating tapes and thermocouples. Helium (He) is used as a carrier gas, hence avoiding solvent effects. A constant flow is directed through the compound source and it is assumed that the He gas is saturated by DBT or 4,6-DMDBT, respectively, up to the vapor pressure at the given source temperature[39]. The entire system is heat traced and held at a constant temperature of 130 °C (150°C in the case of 4,6-DMDBT), and importantly, the temperature of the reactant dosing zone is kept well below this at 110 °C (140 °C in the case of 4,6-DMDBT), in order to avoid condensation and clogging of DBT/4,6-DMDBT in pipes and valves.

2.2. The µ-reactor platform. Catalytic measurements are performed in a specially designed silicon based µ-reactor sealed with a Pyrex lid by anodic bonding[41]. It features a reaction chamber volume of approximately 240 nl, which allows minute amounts (ng) of catalysts to be tested, typically in the form of a thin film of a single layer of particles deposited directly on the bottom of the reaction chamber. In other words, the system offers an ideal platform for testing model catalysts. Two inlets are combined and gas is mixed by diffusion in a meander structure. An integrated capillary outlet on the exit side of the reaction chamber ensures probing of $\sim 5 \times 10^{14}$ molecules s^{-1} at 1 bar. Surplus of gas from the two inlets is directed through an outlet to a turbo pump, and never enters the reaction area. This makes it possible to direct the entire reaction zone volume into a mass spectrometer thereby offering a high sensitivity [41–43]. An integrated Pt thin film on the backside of the silicon chip enables ohmic heating and the temperature is monitored by thermocouples mounted directly on top of the reactor. The reactor is mounted on a stainless steel manifold and sealed by Kalrez O-rings. However, to completely avoid contamination by ambient gasses, the µ-reactor is placed inside a containment volume, which is pumped by a roughing pump to obtain vacuum. The containment volume is heated along with the rest of the system to 130 °C.

2.3. Ionization. The capillary outlet is connected to a stainless steel tube which is separated from the ionization zone by a valve. This part is constantly heated, even when not running experiments. The backside of the valve facing the ionization zone has been modified so that an aluminum tube continues into the ionization zone. The aluminum tube is extended by an additional Al block with the same inner diameter as the tube. The block features two 150 W light bulbs and a thermocouple which enable heat tracing from the valve to the ionization source, purchased from Pfeiffer. The gas enters axially through a spring mounted ceramic fitting in a gas-tight design originally intended for a QMS and is especially well-suited for

small volumes of sample gas. To optimize the MS signal, the ion source is placed as close as possible to a series of entry Einzel lenses inside the TOF-MS, in order to maximize sensitivity.

2.4 TOF-MS. The time-of-flight is designed as an orthogonal mass spectrometer which has been assembled from modules purchased from Jordan TOF Products, Inc[43]. The ionized gas molecules are pushed from the ionization zone into the flight tube by a repelling voltage of + 800V at a frequency of 4000 s^{-1}. A liner voltage of ~ -2500 V accelerates the ions further before they are deflected 7 ° and focused. The reflectron mode increases the effective flight length of the ions thus also the resolution. Finally, the ions are directed towards the micro channel plate (MCP) detector. Whenever a pulse of +800 V is initiated, a multiple-event digitizer (MCS6A) is notified and starts counting the number of ions that has reached the MCP (signal intensity) within a predefined scan length (the x-axis), only limited by the pulse frequency of 250 µs (4000 s^{-1}). Complete mass spectra can therefore be produced every 250 µs but since the number of counts is proportional to the time frame in which they have been iterated, 60 seconds are preset in this work, corresponding to 2.4×10^5 iterations. The peak intensities are proportional to the concentration, and heavy data sets are therefore presented as integrated peak areas of the base peak of the compounds in question normalized to counts.

3. EXPERIMENTAL SECTION

3.1 Sample preparation. The sample was prepared in the MULTIPROBE XP ultra-high vacuum system from Omicron Nanotechnology (now Scienta Omicron) with a typical chamber pressure of 1×10^{-11} mbar. In this system, the reaction chamber of the µ-reactor was cleaned prior to deposition by sputtering with 1 keV Ar^+ for 45 minutes with a sample current of 0.8 – 1.3 µA using an Omicron ISE 10 sputter ion source. The sample current is as measured at a bias of +48 V and not corrected for secondary emissions. Before and after deposition of nanoparticles, the cleanliness and elemental composition of the sample was verified using a combination of low-energy ion scattering spectroscopy (ISS) and X-ray photoelectron spectroscopy (XPS) coupled to an Omicron NanoSAM 7 channel energy analyzer. Minute contaminations of Sn on the verge of the detection limit of XPS were identified with ISS due to its high surface sensitivity. For ISS, 1 keV He^+ ions were rastered in a 1×1 mm² area using an Omicron ISE 100 fine focus ion gun. XPS was done using a SPECS XR 50 X-ray gun using a Mg Kα source with 240 W power.

The nanoparticles were synthesized by an ultra-high vacuum (UHV) nanoparticle source with a typical base pressure of 1×10^{-10} mbar (Nanobeam 2011 from Birmingham Instruments Inc.) coupled to the MULTIPROBE XP. As sketched in Figure 3, particles are formed by magnetron sputtering of a platinum target (99.99% purity, Kurt J. Lesker Company) followed by gas-phase aggregation. The formed particles exit through a small aperture into a differentially pumped UHV region halting further aggregation and interaction by undergoing a super-sonic expansion. The beam of charged particles is then filtered by mass in a lateral time-of-flight mass filter with mass resolution $m/\Delta m$ = 20 ref.[44], before being deposited on a sample in the adjacent MULTIPROBE XP chamber. Samples with a diameter of 6 nm were prepared using around 0.08 mbar pressure in the aggregation zone with an Ar/He ratio of 8:1 by filtering for particles of mass 1,500,000 amu. The conversion between particle size and particle mass was made assuming spherical particles. 555 ng Pt was deposited into the µ-reactor corresponding to a loading of 700 ng/cm^2.

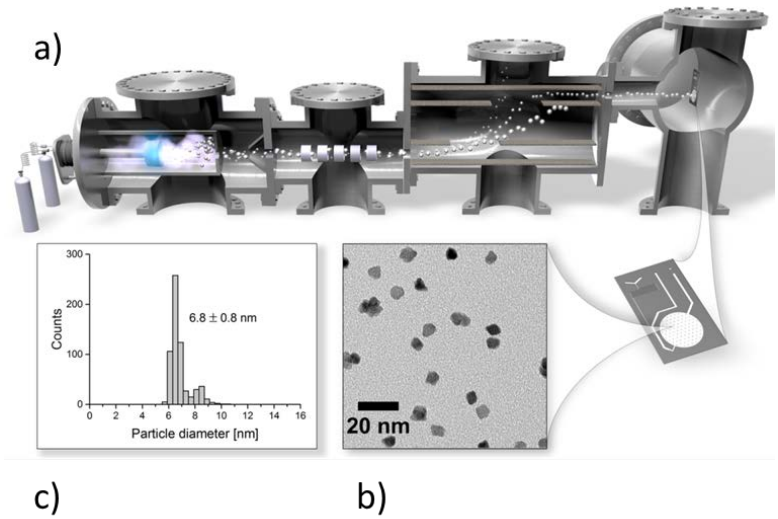

Figure 3 The nanoparticle source (Nanobeam 2011) where the Pt nanoparticles have been synthesized. The nanoparticles are deposited directly into the µ-reactor in the adjacent chamber (MULTIPROBE XP). b) TEM image of deposited 6 nm diameter Pt particles. c) Actual 6 nm particle size distribution from TEM images.

Transmission electron microscopy was used to obtain an actual size distribution of the sample size by using the same deposition conditions as for the µ-reactor on a copper grid covered with lacey carbon. TEM images were acquired in a FEI Tecnai T20 G2 transmission electron microscope and analyzed using ImageJ software. The size distribution found this way is assumed to be representative of the µ-reactor sample disregarding the difference between

substrates. The size distribution in Figure 3c exhibits a second small peak around 8.5 nm. These are due to a fraction of particles carrying two elemental charges instead of a single charge. For the mass filter, particles of double mass and two charges will thus be indistinguishable from the desired particles. The distribution is skewed further by particles landing on top of each other as well as having non-spherical shapes. After deposition, the reactor was sealed by anodic cold bonding to prevent the particles from sintering[41,45].

3.2. Catalyst activity test. The reactor was mounted and pumped down through the main outlet (pressure controller) and capillary outlet. Mass scans were initiated and recorded every second minute and the TOF valve was opened. A He (DBT/4,6-DMDBT) flow of 2 ml/min and 800 mbar was initiated and heating of the containment volume followed. Once the inside of the containment volume reached a temperature of approximately 130 °C (150°C in the case of 4,6-DMDBT), the compound source valves were heated as well. The DBT (or 4,6-DMDBT) source was heated subsequently and once the temperature was stable around 110 °C (140 °C for 4,6-DMDBT) and the TOF signal stopped increasing, a H_2 flow of 1 ml/min was initiated (see supplementary information for TOF overview scan before addition of H_2).

Activity measurements were conducted at 800 mbar over a temperature range from 140-380 °C. Each temperature step of 15 °C was kept for 30 minutes.

4. RESULTS AND DISCUSSION

Figure 4 and Figure 5 show the results of the HDS of DBT and 4,6-DMDBT, respectively. Representative sections of the full mass scans are shown in Figure 4 and for both DBT and 4,6-DMDBT the only products observed were the desulfurized BiPhe and 3,3'-DMBiPhe, respectively. This indicates that the DDS reaction pathway prevails in both cases.

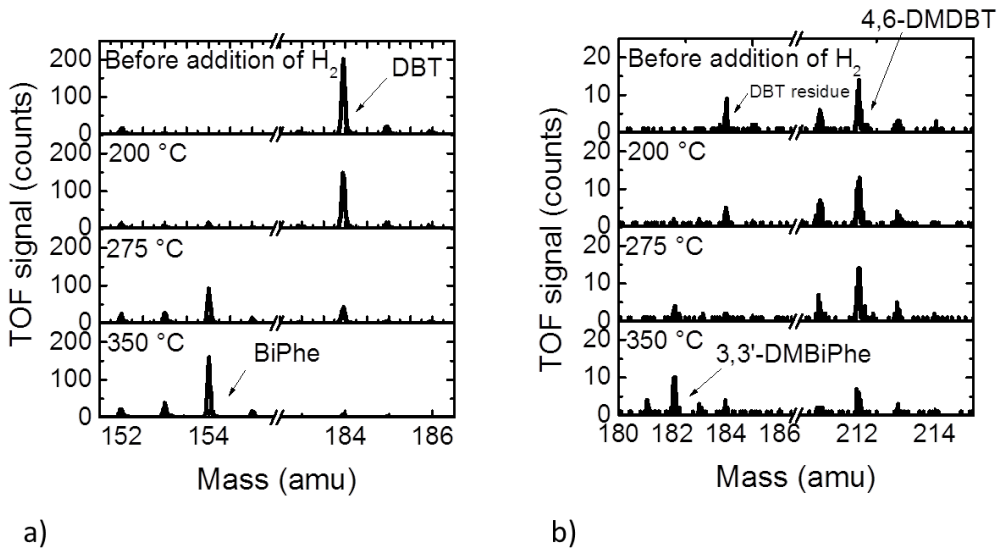

Figure 4 Evolution of relevant peaks of a) DBT and BiPhe and b) 4,6-DMDBT and 3,3'-DMBiPhe before addition of H_2, at 200 °C, 275 °C and 350 °C.

As can be seen in Figure 4, there are no indications of BiPhe nor 3,3'-DMBiPhe before introducing H_2 into the system. In Figure 4a it is clearly seen how DBT is converted into BiPhe as H_2 is added and temperature increased. Furthermore, at 350°C full conversion is approached and almost no DBT is left.

In the uppermost spectrum of 4,6-DMDBT (Figure 4b) small residues of DBT are also present. This is caused by DBT deposits inside the tubing, which are released with the increase in temperature when switching from DBT to 4,6-DMDBT. Hence, is difficult to avoid with the current setup construction enabling back-to-back measurements of DBT and 4,6-DMDBT.

What can also easily be seen from the spectra in Figure 4b is the low peak intensities which are significantly lower than the ones observed in Figure 4a. This can be explained by the low partial pressure of 4,6-DMDBT inside the µ-reactor, which was limited by the heat resistance of the components inside the containment volume. However, it is still evident that 4,6-DMDBT is successfully converted into 3,3-DMBiPhe.

In order to follow the evolution of the relevant peaks as a function of time and reaction temperature, data is presented as the integrated peak area of specified base peaks in each scan

recorded at every temperature step: DBT (*m/z* = 184) and BiPhe (*m/z* = 154) (Figure 5a) and for 4,6-DMDBT (*m/z* = 212) and 3,3'-DMBiPhe (*m/z* = 182) (Figure 5b), respectively.

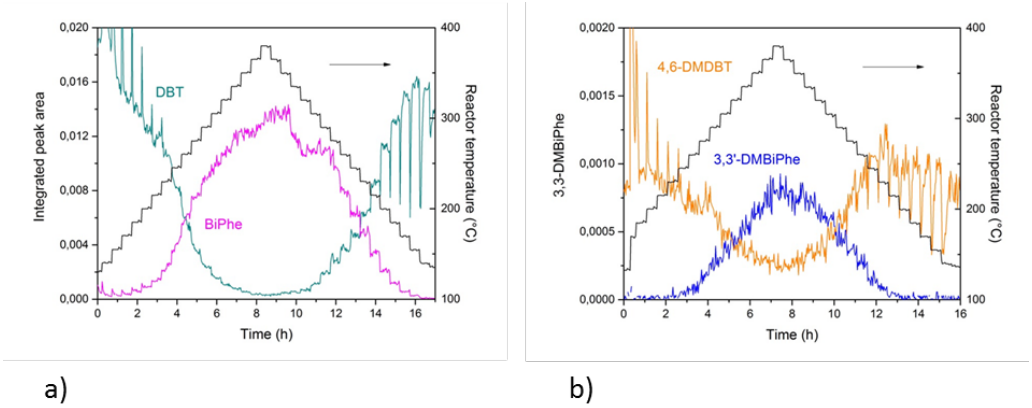

Figure 5 a) Integrated peak areas of DBT and BiPhe as a function of time and temperature. b) Integrated peak areas of 4,6-DMDBT and 3,3'-DMBiPhe as a function of time and temperature.

The left y-axes show the integrated peak areas, whereas the right y-axes show the reaction temperature. As is obvious from both plots in Figure 5, significant spikes are present in the reactant signals at all temperature steps below 250 °C. This is attributed to degassing of adsorbed species from the catalyst itself and means that the partial pressures of the reactants are transiently higher than what can be estimated from the compound source temperatures.

For the conversion of DBT (Figure 5a) it results in temporary increases in the BiPhe signal even at low temperatures. Another artefact is the shoulder observed in the BiPhe signal after approximately ten hours of measurements at a temperature of 335 °C, indicating that a sudden deactivation of the catalyst should have occurred. However, an unintended decrease in the DBT source temperature was observed simultaneously, explaining this behavior.

For the plot in Figure 5b the increase in 3,3'-DMBiPhe follows the decrease in 4,6-DMDBT from temperatures above 250 °C.

Since defining the initial DBT/4,6-DMDBT level is difficult due to the obvious degassing at temperatures below 250 °C, conversion, X, was estimated as the ratio between the product and the sum of reactant and product. Furthermore, an apparatus specific sensitivity factor was applied, resulting in equation

$$X = \frac{xA_{BiPhe/3,3\prime-DMBiPhe}}{xA_{BiPhe/3,3\prime-DMBiPhe} + A_{DBT/4,6-DMDBT}} \qquad (1)$$

Where x is the sensitivity factor and A is the integrated peak area of the specified base peaks.

Figure 6 shows the conversion of both DBT and 4,6-DMDBT. Each data point represents the average conversion and the standard deviation calculated for all TOF scans recorded at every temperature step.

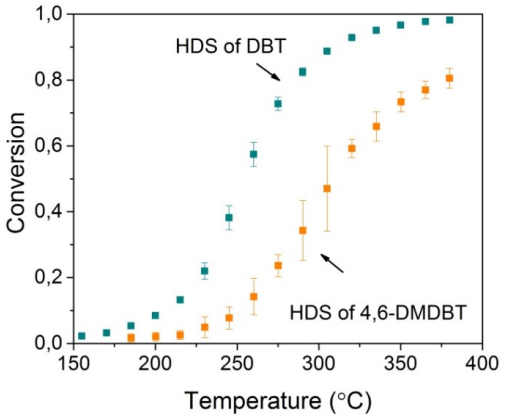

Figure 6 Conversion of DBT and 4,6-DMDBT, respectively.

From Figure 6 it is evident that the HDS of DBT reaches full conversion, whereas the HDS of 4,6-DMDBT has a lower conversion and larger standard deviations.

From Figure 1 it is obvious that the HDS through the HYD pathway requires more than twice as much H_2 than HDS through the DDS pathway. Under industrially relevant conditions the minimum H_2 pressure employed is 20 bar[4], and the effect of the pressure is presumably much more pronounced at the low pressure applied in this study. The Since only DDS products are observed the relation between the HDS of DBT and 4,6-DMDBT observed from Figure 6 is in good agreement with what has previously been reported in literature[46].

5. CONCLUSION

In this work we have shown how the refractory sulfur containing model compounds DBT and 4,6-DMDBT can be successfully desulfurized through gas phase HDS in a silicon-based µ-reactor at 800 mbar. The entire reaction gas volume was analyzed in a TOF-MS, enabling high sensitivity and high mass resolution. We have demonstrated that the configuration of our dedicated setup allows for back-to-back measurements between the two model compounds, and immediately establish the most prevailing reaction pathway (HYD or DDS). We have

shown that even minute amounts of Pt nanoparticles show high activity in both the HDS of DBT and 4,6-DMDBT. Only the DDS products were observed, which is not surprising. Under industrially relevant conditions, it is observed that DBT favors the DDS pathway, whereas 4,6-DMDBT favors the HYD pathway. Since the HYD pathway is highly dependent on the H_2 pressure even at industrially relevant pressures, the effect must be even more pronounced at low pressures, which can be assumed to be the reason why no HYD products are formed. Our setup bridges the gap between structural characterization of relevant catalytic model systems and their activity.

References

1. Song C. An overview of new approaches to deep desulfurization for ultra-clean gasoline, diesel fuel and jet fuel. *Catal. Today* 2003;86(1-4):211-263. doi:10.1016/S0920-5861(03)00412-7.

2. Stanislaus A, Marafi A, Rana MS. Recent advances in the science and technology of ultra low sulfur diesel (ULSD) production. *Catal. Today* 2010;153(1-2):1-68. doi:10.1016/j.cattod.2010.05.011.

3. Qusro Q, Massoth FE. *Comparison of High and Low Pressure HDS Activities for Mo/Al2O3 Catalysts*.; 1987. doi:10.1016/S0166-9834(00)82906-1.

4. Topsøe H, Clausen BS, Massoth FE. *Hydrotreating Catalysis Science and Technology*. (Anderson JR, Boudart M, eds.). Springer Verlag; 1996.

5. Bensch W. *Comprehensive Inorganic Chemistry II*. Elsevier; 2013. doi:10.1016/B978-0-08-097774-4.00723-3.

6. Topsøe HH, Knudsen KG, Byskov LS, Nørskov JK, Clausen BS. Advances in Deep Desulfurization. In: *Science and Technology in Catalysis*.; 1998:13-22.

7. Srivastava VC. An evaluation of desulfurization technologies for sulfur removal from liquid fuels. *RSC Adv.* 2012;2(3):759. doi:10.1039/c1ra00309g.

8. Shafi R, Hutchings GJ. Hydrodesulfurization of hindered dibenzothiophenes: an overview. *Catal. Today* 2000;59(3-4):423-442.

9. Kibsgaard J, Tuxen A, Knudsen K., et al. Comparative atomic-scale analysis of promotional effects by late 3d-transition metals in MoS 2 hydrotreating catalysts. *J. Catal.* 2010;272:195-203. doi:10.1016/j.jcat.2010.03.018.

10. Kilanowski DR, Teeuwen H, de Beer VHJ, Gates BC, Schuit GCA, Kwart H. Hydrodesulfurization of thiophene, benzothiophene, dibenzothiophene, and related compounds catalyzed by sulfided CoO-MoO3/y-Al2O3: Low-pressure reactivity studies. *J. Catal.* 1978;55(2):129-137. doi:10.1016/0021-9517(78)90199-9.

11. Kabe T, Ishihara A, Zhang Q. Deep desulfurization of light oil. Part 2: hydrodesulfurization of dibenzothiophene, 4- methyldibenzothiophene and 4,6-dimethyldibenzothiophene. *Appl. Catal. A Gen.* 1993;97.

12. Kabe T, Ishihara A, Tajima H. Hydrodesulfurization of Sulfur-Containing Polyaromatic Compounds in Light Oil. *Ind. Eng. Chem. Res.* 1992;31:1577-1580.

13. Egorova M, Prins R. Hydrodesulfurization of dibenzothiophene and 4,6-dimethyldibenzothiophene over sulfided NiMo/γ -Al2O3, CoMo/γ-Al2O3, and Mo/γ-Al2O3 catalysts. *J. Catal.* 2004;225:417-427. doi:10.1016/j.jcat.2004.05.002.

14. Grønborg SS, Šaric M, Moses PG, Rossmeisl J, Lauritsen JV. Atomic scale analysis of sterical effects in the adsorption of 4,6-dimethyldibenzothiophene on a CoMoS hydrotreating catalyst. *J. Catal.* 2016;344:121-128. doi:10.1016/j.jcat.2016.09.004.

15. Egorova M, Prins R. The role of Ni and Co promoters in the simultaneous HDS of dibenzothiophene and HDN of amines over Mo/γ -Al 2 O 3 catalysts. *J. Catal.* 2006;241:162-172. doi:10.1016/j.jcat.2006.04.011.

16. Knudsen KG, Cooper BH, Topsøe H. Catalyst and process technologies for ultra low sulfur diesel. *Appl. Catal. A Gen.* 1999;189:205-215.

17. Bartsch R, Tanielian C. Hydrodesulfurization I. Hydrogenolysis of Benzothiophene and Dibenzothiophene over CoO-MoO3-Al203 Catalyst. *J. Catal.* 1974;35:353-358.

18. Houalla M, Nag NK, Sapre AV, Broderick DH, Gates BC. Hydrodesulfurization of Dibenzothiophene Catalyzed by Sulfided CoO-MoO3 y-Al2O3: The Reaction Network. *ACS Div. Fuel Chem. Prepr.* 1978;24:1015-1021.

19. Whitehurst DD, Isoda T, Mochida I. Present State of the Art and Future Challenges in the Hydrodesulfurization of Polyaromatic Sulfur Compounds. *Adv. Catal.* 1998;42:345-471. doi:10.1016/S0360-0564(08)60631-8.

20. Singhal GH, Espino RL, Sobel JE, Huff GA. Hydrodesulfurization of sulfur heterocyclic compounds: Kinetics of dibenzothiophene. *J. Catal.* 1981;67(2):457-468. doi:10.1016/0021-9517(81)90305-5.

21. Li X, Wang A, Egorova M, Prins R. Kinetics of the HDS of 4,6-dimethyldibenzothiophene and its hydrogenated intermediates over sulfided Mo and NiMo on γ -Al 2 O 3. *J. Catal.* 2007;250:283-293. doi:10.1016/j.jcat.2007.06.005.

22. Prins R, Egorova M, Röthlisberger A, Zhao Y, Sivasankar N, Kukula P. Mechanisms of hydrodesulfurization and hydrodenitrogenation. *Catal. Today* 2006;111(1-2):84-93.

doi:10.1016/j.cattod.2005.10.008.

23. Ertl G, Freund H-J. Catalysis and Surface Science. *Phys. Today* 1999;52(1):32-38. doi:10.1063/1.882569.

24. Palmer RE, Pratontep S, Boyen H-G. Nanostructured surfaces from size-selected clusters. *Nat. Mater.* 2003;2:443-448.

25. Sattler K, Muhlbach J, Recknagel E. Generation of Metal Clusters Containing from 2 to 500 Atoms. *Phys. Rev. Lett.* 1980;45(10):821-824.

26. Dietz TG, Duncan MA, Powers DE, Smalley RE. Laser production of supersonic metal cluster beams Laser production of supersonic metal cluster beams a). *J. Chem. Phys.* 1981;74:6511-41101. doi:10.1063/1.3697599.

27. Böhme DK, Schwarz H. Gas-phase catalysis by atomic and cluster metal ions: The ultimate single-site catalysts. *Angew. Chemie - Int. Ed.* 2005;44(16):2336-2354. doi:10.1002/anie.200461698.

28. Jacobs PW, Somorjai GA. Conversion of heterogeneous catalysis from art to science: the surface science of heterogeneous catalysis. *J. Mol. Catal. A Chem.* 1998;131:5-18.

29. Tuxen AK, Füchtbauer HG, Temel B, et al. Atomic-scale insight into adsorption of sterically hindered dibenzothiophenes on MoS2 and Co-Mo-S hydrotreating catalysts. *J. Catal.* 2012;295:146-154. doi:10.1016/j.jcat.2012.08.004.

30. Tuxen AK, Kibsgaard J, Gøbel H, et al. Size Threshold in the Dibenzothiophene Adsorption on MoS 2 Nanoclusters. *ACS Nano* 2010;4(8):4677-4682. doi:10.1021/nn1011013.

31. Lauritsen JV, Helveg S, Lægsgaard E, et al. *Atomic-Scale Structure of Co-Mo-S Nanoclusters in Hydrotreating Catalysts*. Academic Press; 2001. doi:10.1006/jcat.2000.3088.

32. Lauritsen JV, Kibsgaard J, Olesen GH, et al. Location and coordination of promoter atoms in Co- and Ni-promoted MoS2-based hydrotreating catalysts. *J. Catal.* 2007;249(2):220-233. doi:10.1016/j.jcat.2007.04.013.

33. Daage M, Chianelli RR, Ruppert AF. Structure-function relations in layered transition

metal sulfide catalysts. In: *New Frontiers in Catalysis*.; 1993:571-584.

34. Helveg S, Lauritsen JV, Lægsgaard E, et al. Atomic-Scale Structure of Single-Layer MoS 2 Nanoclusters. *Phys. Rev. Lett.* 2000;84(5):951-954.

35. Bollinger M, Jacobsen K, Nørskov J. Atomic and electronic structure of MoS2 nanoparticles. *Phys. Rev. B* 2003;67(8):85410. doi:10.1103/PhysRevB.67.085410.

36. Bruix A, Füchtbauer HG, Tuxen AK, et al. In Situ Detection of Active Edge Sites in Single-Layer MoS 2 Catalysts. 2015;(9):9322-9330.

37. Baubet B, Girleanu M, Gay AS, et al. Quantitative Two-Dimensional (2D) Morphology-Selectivity Relationship of CoMoS Nanolayers: A Combined High-Resolution High-Angle Annular Dark Field Scanning Transmission Electron Microscopy (HR HAADF-STEM) and Density Functional Theory (DFT) Study. *ACS Catal.* 2016;6(2). doi:10.1021/acscatal.5b02628.

38. Girgis MJ, Gates BC. Reactivities, reaction networks, and kinetics in high-pressure catalytic hydroprocessing. *Ind. Eng. Chem. Res.* 1991;30(9):2021-2058. doi:10.1021/ie00057a001.

39. Edwards DR, Prausnitz JM. Vapor Pressures of Some Sulfur-Containing, Coal-Related Compounds. *J. Chem. Eng. Data* 1981;26(2):121-124.

40. US Environmental Protection Agency. 4,6-Dimethyldibenzothiophene. 2017.

41. Henriksen TR, Olsen JL, Vesborg P, Chorkendorff I, Hansen O. Highly sensitive silicon microreactor for catalyst testing. *Rev. Sci. Instrum.* 2009;80(12):124101. doi:10.1063/1.3270191.

42. Henriksen TR. Silicon Microreactors for Measurements of Catalytic Activity. 2010;(April).

43. Andersen T, Jensen R, Christensen MK, Pedersen T, Hansen O, Chorkendorff I. High mass resolution time of flight mass spectrometer for measuring products in heterogeneous catalysis in highly sensitive microreactors. *Rev. Sci. Instrum.* 2012;83(7):75105. doi:10.1063/1.4732815.

44. Issendorff B Von, Palmer RE. A new high transmission infinite range mass selector for

cluster and nanoparticle beams. 1999;70(12):4497-4501.

45. Vesborg PCK, Olsen JL, Henriksen TR, Chorkendorff I, Hansen O. Note: Anodic bonding with cooling of heat-sensitive areas. *Rev. Sci. Instrum.* 2010;81(1). doi:10.1063/1.3277117.

46. Gates BC, Topsøe H. Reactivities in deep catalytic hydrodesulfurization: challenges, opportunities, and the importance of 4-methyldibenzothiophene and 4,6-dimethyldibenzothiophene. *Polyhedron* 1997;16(18):3213-3217.

Paper 2

Engineering Ni-Mo-S Nanoparticles for Ultra-Deep Hydrodesulfurization: Reactive Gas Aggregation Synthesis, Characterization and Catalytic Testing

In preparation.

Engineering Ni-Mo-S Nanoparticles for Ultra-Deep Hydrodesulfurization: Reactive Gas Aggregation Synthesis, Characterization and Catalytic Testing

Anders Bodin[1], Ann-Louise N. Christoffersen[1], Christian F. Elkjær[2], Jakob Kibsgaard[1], Stig Helveg[2], and Ib Chorkendorff [*1]

[1]Department of Physics, Technical University of Denmark, Fysikvej, Building 312, DK-2800 Kgs. Lyngby, Denmark
[2]Haldor Topsøe A/S, Nymøllevej 55, DK-2800 Kgs. Lyngby, Denmark

July 23, 2017

Abstract

With the aim of engineering highly active nanoparticle catalysts for ultra-deep hydrodesulfurization (HDS), we present the synthesis of well-defined model systems of mass-selected Ni-Mo-S nanoparticles by aggregation of sputtered metal from a $Mo_{75}Ni_{25}$ target in a reactive atmosphere of Ar and H_2S. The nanoparticles are undersulfided with a stoichiometry of $Mo_{0.8}Ni_{0.2}S_{1.1}$, and exhibit high-surface area morphologies with many under-coordinated sites, which is desired for desulfurization of molecules where the location of the sulfur atoms makes the HDS sterically hindered. Before deposition on a substrate, the nanoparticles are filtered by mass in a quadrupole mass filter, and it is shown that varying the deposition mass can significantly alter the nanoparticle structures. Using a micro-reactor system, we assess the catalytic activity of the Ni-Mo-S nanoparticles for HDS of dibenzothiophene and show that nanoparticles produced by reactive gas-phase aggregation are more than twice as active as nanoparticles produced by post-sulfiding metallic Ni-Mo nanoparticles.

[*]Corresponding author. Email: ibchork@fysik.dtu.dk.